Modeling, Estimation and Benchmarking of Lithium Ion Electric Bicycle Battery

MODELING, ESTIMATION AND BENCHMARKING OF LITHIUM ION ELECTRIC BICYCLE BATTERY

By

Weizhong Wang, B.Sc

A Thesis
Submitted to the School of Graduate Studies
in Partial Fulfillment of the Requirements
for the Degree
Master of Applied Science

McMaster University

MASTER OF APPLIED SCIENCE (2016) Electrical Engineering
McMASTER UNIVERSITY Hamilton, Ontario

TITLE: **Modeling, Estimation and Benchmarking of Lithium Ion Electric Bicycle Battery**

AUTHOR: Weizhong Wang
B. Sc.
School of Information and Electrical Engineering
(Harbin Institute of Technology, China)

SUPERVISOR: Ali Emadi, Professor
Ph. D. (Texas A&M University)
IEEE Fellow
Canada Excellence Research Chair in Hybrid Powertrain

CO-SUPERVISOR: Pawel Malysz, Adjunct Assistant Professor
Ph.D (McMaster University)
FCA Fiat Chrysler Automobiles

NUMBER OF PAGES: XX, 157

谨以此献给我的母亲父亲

To My Parents

Abstract

As a conventional transportation modality, bicycles have been gradually electrified to meet the desire for convenient and green commuting patterns, especially in developed urban areas. The electric bicycle battery pack and its management system are core elements that determine key performance metrics such as electric range and output power. With respect to electric bicycle applications, focused research on the battery, its management system, and performance has received less attention compared to other energy storage applications.

In this thesis, a well-developed conversion kit produced by BionX is studied. A data collecting system is first installed to record both mechanical and electrical data, such as speed, power and voltage; this enables defining two standard riding cycles at different riding conditions. Two benchmarking tests are performed to investigate the battery life in pure electric mode and at different threshold levels of optimal assistance.

A novel quadratic programming based fitting algorithm is derived and applied in both time and frequency domain parameter identification tests. The proposed algorithm is able to fit single/multiple pulses by applying a masking vector. Sensitivity study and experimental results show the high robustness and fast computation time of the approach compared to existing and commonly used methods, such as fmincon. The comparison between hybrid power pulse

characterization (HPPC) and electrochemical impedance spectrum (EIS) tests are performed in terms of extracted internal resistance.

A second-order RC battery model is developed using parameters extracted from HPPC tests. The model is validated by experimental riding cycles and used to generate the reference SOC profiles that are employed in a SOC estimation study. Four estimation strategies, including extended Kalman Filter (EKF), Sigma point Kalman Filter (SPKF), Cubature Kalman Filter (CKF), and joint extended Kalman Filter (JEKF), are compared systematically in terms of accuracy, robustness and computation complexity.

Acknowledgements

I would first like to thank my thesis supervisor Prof. Ali Emadi of the ECE department at McMaster University. He consistently steered me in the right the direction whenever he thought I needed it. I have been given all kinds of guidance in study or daily life. The door to Prof. Emadi's office was always open whenever I ran into a trouble spot or had a question about my research.

I would like to express my very great appreciation to Dr. Malysz, my research co-supervisor, for his valuable and constructive suggestions during the planning and development of this research work. His willingness to give his time so generously has been very much appreciated. Whenever I need help from him, he is and will be always on the other side of teleconference no matter how busy he is.

I would also like to thank Prof. Gauchia and her students Khalin Khan and Medri Jafari for performing battery characterization testing at Michigan Technological University. Without their passionate participation and input, this research could not have been successfully conducted.

I am grateful to my colleagues in the Canada Excellence Research Chair in Hybrid Power Program. I will never forget the great times that we have shared together.

This research was undertaken, in part, thanks to funding from the Canada Excellence Research Chairs Program.

CONTENTS

LIST OF FIGURES

LIST OF TABLES

LIST OF ABBREVIATIONS

AC	alternate current
BMS	battery manage system
CPE	constant phase element
CV	constant voltage
CKF	Cubature Kalman filter
CA	Cycle Analyst
DC	direct current
EIS	electrochemical impedance spectrum
ECM	equivalent circuit model
EKF	extended Kalman filter
FRA	frequency response analyzer
FRF	full range fitting
GA	genetic algorithm
GUI	graphic user interface
HPPC	hybrid power pulse characterization
JEKF	joint extended Kalman filter
KF	Kalman filter
MEP	maximum energy pulse
OLS	ordinary least squares
QP	quadratic programming
RLS	recursive least square
RMSE	root mean square error
SPF	single pulse fitting
SPKF	sigma point Kalman filter
SEI	solid electrolyte interface
SOH	State of Health
ZOH	zero-order holder

Chapter 1

INTRODUCTION

1.1 Motivation

Fossil fuels are not a sustainable energy source; however, human activities have been more energy-consuming. This trend, to some extent, drives science and technology to develop in a 'greener' way. As a result an increasing number of transportation manufacturers are exploring the field of transportation electrification. Even though improving fuel efficiency by electrifying automobiles [1]–[5] , such as Toyota Prius and Tesla Model S, is a promising way to reduce air pollution and the dependence on fossil fuel, it is still unrealistic to drive in cities with high population density, e.g. New York City. Public transportation and bicycles are therefore better options to commute in urban areas.

Similarly with electrified vehicles, electrified bicycles start to step into people's daily life to offer a healthier way to commute and are a cleaner alternative to motorcycles. Many manufactures have Electric Bicycles on sale and specific electric bike kits are developed for converting traditional bikes to Electric Bicycles, as shown in Figure 1.1. The Electric Bicycle market is expected to double from 2013 to 2020, as shown in Figure 1.2. It proves that the Electric Bicycles have drawn increasing attention and will be broadly adopted by most consumers who are looking for an alternative way of commuting. Electric Bicycles provide a balance between exercise and convenience. They assist riders to climb inclines and overcome wind resistance, which are more difficult by conventional bicycles.

The battery pack as the core element of any electrified transportation system determines the battery life and restricts the maximum power output to the motor. Few researchers have investigated the battery manage system (BMS) in Electric Bicycle application. However, it is necessary to have a better understanding of the BMS in this application, because increasing higher volume battery pack will be used to fulfill longer range demand. Higher volume means more cells in series/parallel, which leads to higher possibility of unbalanced cells and difficulty to precisely manage the battery pack.

(a) (b)

(c) (d)

Figure 1.1 Some examples of commercial E-bicycles: (a) Stealth Electric Bikes B-52, with maximum 5.2 kW motor output, up to 80 km/h and 80 km range, (b) Smart Electric Bicycle powered by BionX motor, battery and control unit, (c) BionX conversion kit (48 V, 8.8 Ah battery pack and 350 W motor), and (d) Electrified bike by BionX conversion kit

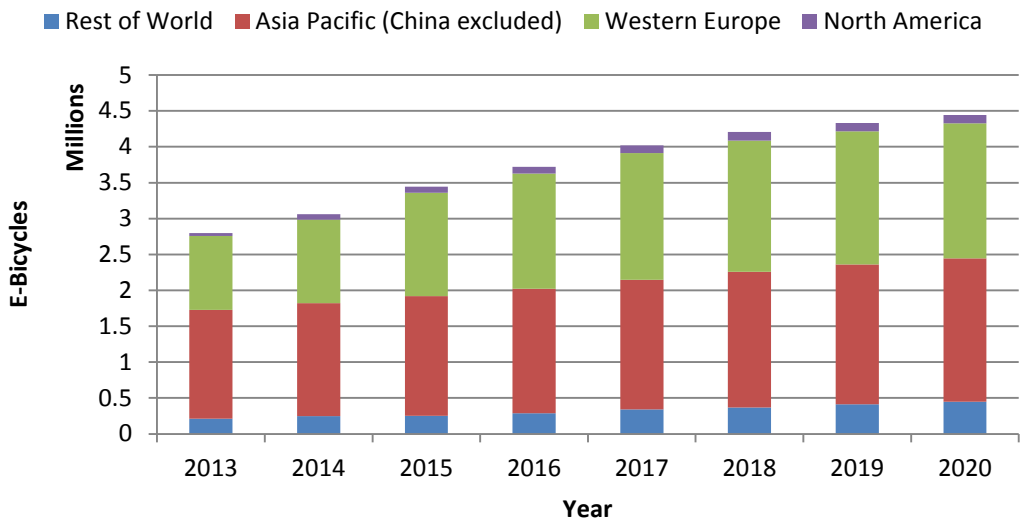

Figure 1.2 The annual Electric Bicycle sales by region and forecast scenario (adopted from [6])

1.2 Outline

This thesis will include the benchmarking, parameterization in both time domain and frequency domain, and modeling of an Electric Bicycle lithium-ion battery pack. The details are organized as follows.

Chapter 2 focuses on literature review. The previous work from other researchers is summarized. It is divided into three categories: battery modeling, SOx estimation and fundamentals about electrochemical impedance spectra (EIS). This chapter will briefly state the basic knowledge and drawbacks of existing techniques.

The Electric Bicycle system is described in Chapter 3. The conversion kit and data acquisition systems are introduced. By using the data acquisition system, electrical and mechanical information are used to define so-called riding cycles. The riding cycles will be used to validate the proposed battery model in Chapter 6. Two benchmarking tests are performed: 1) range test,

the maximum distance under pure electric mode, 2) user experience test, correlation between assistance power and a new defined metric referred to as 'tiredness'.

Time domain experiments and characterizations will be explained in Chapter 4. The capacity test and hybrid power pulse characterization (HPPC) are briefly introduced and the results will be discussed. A novel quadratic programming (QP) based optimizer is designed and employed to fit the results from HPPC tests. HPPC and maximum energy pulse (MEP) signal simulators are developed and applied to a sensitivity study on the proposed fitting algorithm.

EIS based frequency domain parameterization tests were performed and explained in Chapter 5. A corresponding QP based fitting algorithm is formulated and a sensitivity study is performed to investigate its robustness. The results from EIS tests are parameterized by the fitting algorithm and the parameters are compared with the ones from HPPC tests.

In Chapter 6, a comprehensive comparison for SOC estimation among extended Kalman Filter, Sigma point Kalman Filter, Cubature Kalman Filter, and joint extended Kalman Filter are performed. The work that has been done in Chapter 3 and 4 is used in this chapter. The parameters extracted from HPPC tests is input to a second-order RC equivalent circuit model (ECM) to mimic the battery's dynamic behavior. The ECM is validated by comparing to voltage response from riding cycles in Chapter 3 with the same current input.

The overview of this thesis is summarized in Figure 1.3.

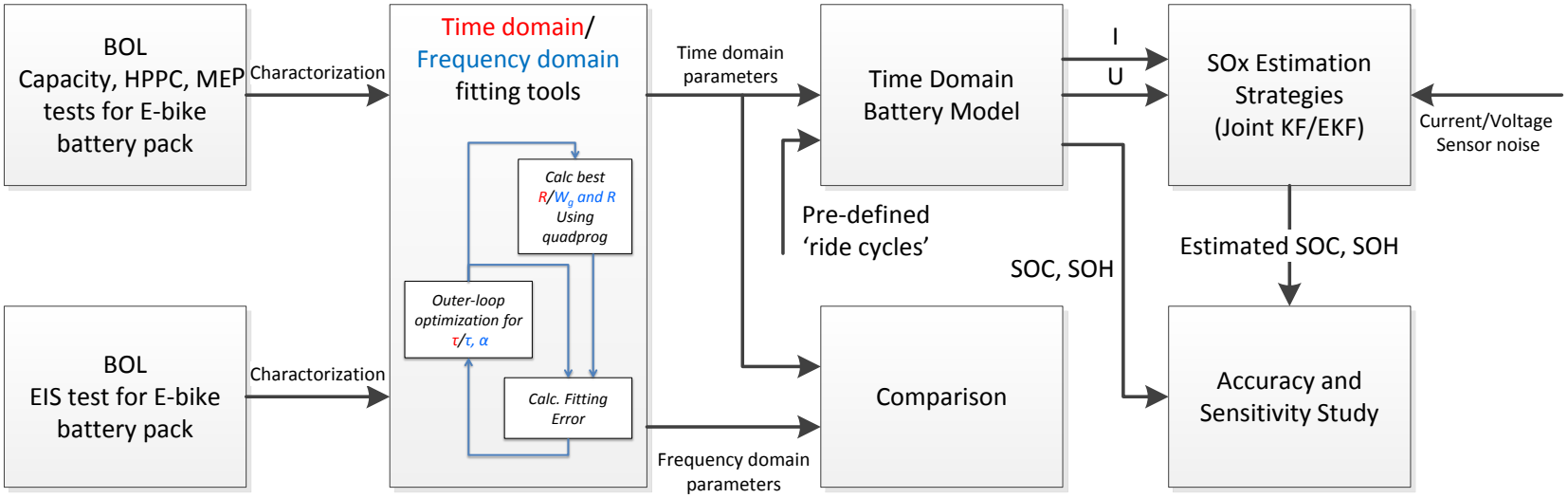

Figure 1.3 Thesis overview

1.3 Publications

[1] W. Wang, J. Ye, P. Malysz, H. Yang and A. Emadi, "Sensitivity analysis of Kalman Filter based capacity estimation for electric vehicles," *IEEE Transportation Electrification Conference and Expo (ITEC), 2015 IEEE*, Dearborn, MI, June 2015, pp. 1-7.

[2] W. Wang, P. Malysz, D. Wang, R. Gu, H. Yang, and A. Emadi, "Efficient Multi-cell SOC Estimation for Electrified Vehicle Battery Packs," *2016 IEEE Transportation Electrification Conference and Expo (ITEC), Dearborn, MI, USA, 2016, pp. 1-5.*

[3] W. Wang, D. Wang, T. Li, X. Wang, R. Ahmed, A. Emadi, "Comparison of Kalman Filter-Based State-of-Charge Estimation Strategies Based On Equivalent Circuit Battery Models," *2016 IEEE Transportation Electrification Conference and Expo (ITEC), Dearborn, MI, USA, 2016, pp. 1-6.*

[4] W. Wang, P. Malysz, K. Khan, L. Gauchia and A. Emadi, "Modeling, Parameterization, and Benchmarking of a Lithium Ion Electric Bicycle Battery," *to be presented at IEEE Energy Conversion Congress & Exposition (ECCE), September 2016.*

[5] R. Gu, P. Malysz, D. Wang, W. Wang, H. Yang and A. Emadi, "On the Design of a Direct Cell Coupled Hybrid Energy Storage System for Plug-in Hybrid Electric Vehicles," *2016 IEEE Transportation Electrification Conference and Expo (ITEC), Dearborn, MI, USA, 2016, pp. 1-7.*

Chapter 2

LITERATURE REVIEW

The literature review will be mainly focusing on the battery modeling, SOC estimation, and fitting algorithm in order to investigate the advantages and disadvantages of existing techniques.

2.1 Battery Modeling

Several battery models have been presented in the literature, such as equivalent circuit models and electrochemical models [7]–[9]. Equivalent circuit-based models utilize simple electric circuit components such as resistors and capacitors to model the relationship between the input current and the output terminal voltage. Equivalent circuit-based models, such as the first order OCV-RRC model is relatively accurate and simple to be implemented onboard of a battery management system. Electrochemical based models try to formulate the internal chemical reactions, such as diffusion of lithium. The electrochemical models therefore have better correlation to physical/chemical phenomena [10].

2.1.1 Electrochemical Modeling

Derivation of a full-order electrochemical based battery model involves hundreds of states, compared to equivalent circuit-based models with only 2-5 states [9]. It makes online estimation based on full-order electrochemical based battery models highly intractable. The reduced order models, thus, are introduced.

There are two ways to reduce the order [11]: 1) Electrode Averaged Model (EAM), which can be achieved by ignoring the solid concentration distribution along with the electrode, and taking the

material diffusion into account. 2) State Values Model (SVM). It changes the governing equations to derive analytical transfer functions.

C. Speltino, D. Di Domenico, G. Fiengo and A. Stefanopoulou [12] conducted a comparison between two kinds of reduced order Lithium-Ion battery models chemically. By analyzing these two methods to reduce order, it is found that both of them can give good voltage estimations. But they have their own advantages and disadvantages. For example, the EAM can estimate SOC and voltage precisely thanks to considering discontinuities of rapid electrode bulk concentration. However, on-line parameters estimation cannot be implemented easily because of the strong non-linearity. On the contrary, the SVM model shows poor SOC estimation and difficulty to set up. But the less complex linear structure is suitable for on-line adaptive control and voltage estimation.

2.1.2 Electrical Modeling

Due to high complexity of building the electrochemical model even for reduced-order ones which normally have more than 20 parameters [13], electrical circuit modeling is a more reasonable alternative to have similar accuracy compared with electrochemical modeling. Alternatively, the mathematical models driven by empirical functions, e.g. OCV is an n_{th} polynomial function of SOC, are used to describe the battery behavior. It is proved that mathematical models are relatively inaccurate, 5 – 20% error [14]. Therefore, electrical modeling is widely adopted.

The relationship between the input and output of the battery can be characterized by using an equivalent circuit model (ECM) that consists of resistors, capacitors and voltage source [15] [16]. ECM is the most commonly used model in practice. A second-order RC model is shown in

Figure 2.1, where V_o, R_a, C_a, R_b and C_b are functions of SOC and temperature. Higher ordered RC models (more RC pairs) are able to more accurately represent kinetic aspects of internal impedance behavior [17] and [8]. The output equations based on various model orders are summarized in Table 2.1. In order to improve the accuracy of ECM, many researchers proposed so-called enhanced ECM considering temperature effect [18], surface SOC based on electrochemical analysis [19], and charge redistribution effect [20].

A hysteresis effect on OCV-SOC relation was observed in many battery chemistries, such as Nickel-metal hydride batteries and Lithium-ion batteries. The hysteresis effect exhibits different OCV when batteries are in steady state based on current rate, current direction and cycling histories [21]. In other word, it is a character that charging OCV is higher than discharging OCV at the same SOC level. It has been observed that the effect is significant for Nickel-metal hydride batteries [21]. On the other hand, for Li-Ion batteries the effect is relatively small to consider [22].

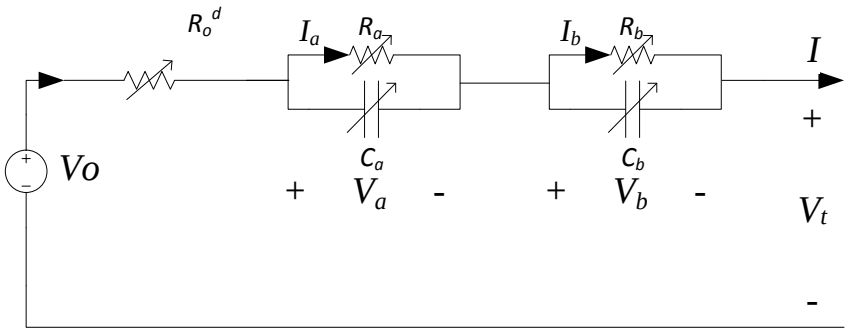

Figure 2.1 Second-order RC equivalent circuit model

Xiaosong Hu and Shengbo Li [8] compared twelve battery models by validating two types of batteries (LiNMC cell and $LiFePO_4$ cell) under different cell datasets. The twelve battery models refer to combined model, enhanced self-correcting model and different ordered RC models. The conclusion is that first-order RC model is preferred in terms of accuracy and complexity. The

trade-off of the number of cells has to be made to balance the performance and computational complexity of the ECMs.

Table 2.1: Summary of RC models

Model	Output equations
The first-order RC model	$V_{a,k+1} = e^{(-\Delta t/R_a C_a)} V_{a,k} + R_a (1 - e^{(-\Delta t/R_a C_a)}) I_k$ $V_t = OCV(SOC) - R_o I_k - V_{a,k}$
The first-order RC model with hysteresis state	$V_t = OCV(SOC) - R_o I_k - V_{a,k} + V_h$
The second-order RC model	$V_t = OCV(SOC) - R_o I_k - V_{a,k} - V_{b,k}$
The second-order RC model with hysteresis state	$V_t = OCV(SOC) - R_o I_k - V_{a,k} - V_{b,k} + V_h$
The third-order RC model	$V_t = OCV(SOC) - R_o I_k - V_{a,k} - V_{b,k} - V_{c,k}$
The third-order RC model with hysteresis state	$V_t = OCV(SOC) - R_o I_k - V_{a,k} - V_{b,k} - V_{c,k} + V_h$

2.2 State of Charge

The battery SOC is defined as the remaining battery capacity in comparison to the battery nominal capacity [23]. Unlike internal combustion engines, where fuel tank level can be directly monitored by a sensor, battery SOC is not directly measurable [24]; therefore various techniques for SOC estimation have been presented in the literature. One of the simplest techniques to calculate the SOC is known as Coulomb Counting, in which current is integrated to calculate the total input and output charge. However, since coulomb counting involves integration, error is accumulated from current sensors and other uncertain disturbances such as the initial SOC error [25]. Several improvements to Coulomb Counting technique has been presented in the literature, such as periodically correcting the initial SOC based on the OCV as shown in [26].

2.2.1 Definition of SOC

A few definitions are noted first as follows:

C-rate is a standard term that describes the charging or discharging current based on the capacity. For example, 1C is equal to 40A if the capacity is 40Ah. In other words, it will take 1 hour to fully discharge or charge the battery.

Total capacity is the maximum ampere-hours that battery can output at ambient temperature and at a small current amplitude, e.g. C/30 rate, to discharge from 100% SOC.

Available capacity is the maximum remaining ampere-hours that battery can be discharged at ambient temperature and real-life demands.

SOC is similar to a fuel tank gage which could be treated as an indicator of how much available capacity is left. It can be expressed as

$$SOC = CAP_{available} / CAP_{total} \times 100\% \tag{2.1}$$

However, SOC cannot be directly calculated by (2.1) because the available capacity is not directly measurable. Furthermore, to determine SOC accurately is a critical task for the BMS. Estimating SOC is challenging due to the nonlinearity of internal battery reactions [27]. This nonlinear characteristic can be caused by either internal condition, such as the capacity fading and the resistance increasing, or external condition including temperature and current load. Although accurate SOC is necessary for protecting the battery, SOC cannot be measured directly from the battery. Since there are typically two measurements in the battery, terminal voltage and current load, the battery can be thought of as a 'black box'. SOC can be simply estimated by online algorithms.

2.2.2 SOC Estimation

Coulomb Counting

SOC can be calculated by the integral of current during a specific period time, i.e.

$$SOC = \int \eta i dt \Big/ Cap_{total} \times 100\% \tag{2.2}$$

where, η is the efficiency of charging/discharging. It is the most commonly used method to approximately calculate the SOC, so called Coulomb Counting. And Coulomb Counting is normally used as the reference SOC to be compared with other SOC estimation strategies in simulation, provided capacity is known and an accurate current sensor is used.

In practice, the counting technique is barely used to estimate SOC, since the current sensor noise will have significant influence on the accuracy, this is because

1) There is an integral operation in (2.2) which will accumulate the censor bias/error.
2) The charging and discharging efficiency can change.
3) The total capacity will degrade as the battery ages instead of being a constant.

As a result, the factors above could dramatically affect the accuracy of SOC estimation.

OCV-SOC Mapping

A unique relationship between OCV and SOC has been experimentally observed [28]. That is OCV is a nonlinear monotonic function of SOC. Therefore, SOC can be estimated by mapping OCV through the OCV-SOC relationship. For example, in Figure 2.2 SOC is 60% when OCV is shown in a black dashed line. So it can be found that OCV-SOC mapping is a relatively accurate method to obtain SOC by using precise OCV. However, open circuit voltage is defined as the

voltage without current load and when the system is in equilibrium state. The OCV can be obtained after a period of so called relaxation time at each SOC and temperature. Within this time interval, the diffusion process inside the battery is gradually completed until a stable equilibrium state [29]. Consequently, this mapping method is not commonly used because of the fact that the process to get the OCV vs. SOC curve is time-consuming. In addition, the curve will lose fidelity since open circuit voltage can change as the battery ages.

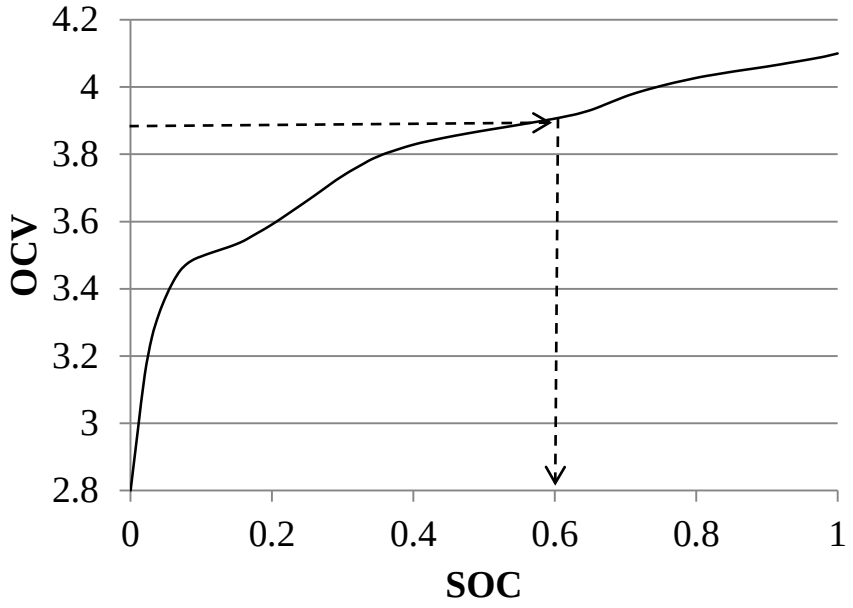

Figure 2.2 An example of mapping OCV to SOC

Observer based Techniques

By using the input/output measurements, a state observer is able to estimate the internal states. The observer design is based on state-space matrices that describe the real system. A feedback gain is used to drive the observer to converge toward a real system state. This procedure is done by multiplying the error between the real output and estimated output. A typical system block diagram is illustrated in Figure 2.3. As shown in Figure 2.3, both of the real system and the

observer have the same state-space matrices in (2.3). In order to eliminate the modeling uncertainty, a sliding mode observer is developed in [30]. Adaptive algorithms are implemented to SOC estimation. By decreasing or eliminating the error between the actual output and estimated output, the uncertainty of the battery model and the measurement noise can be reduced [30].

$$\begin{cases} x_k = A_{k-1}x_{k-1} + B_{k-1}u_{k-1} + w_{k-1} \\ y_k = C_k x_k + D_k u_k + v_k \end{cases} \tag{2.3}$$

where, w_k and v_k are process noise and measurement noise, respectively. Both of them are white (zero mean) Gaussian noises.

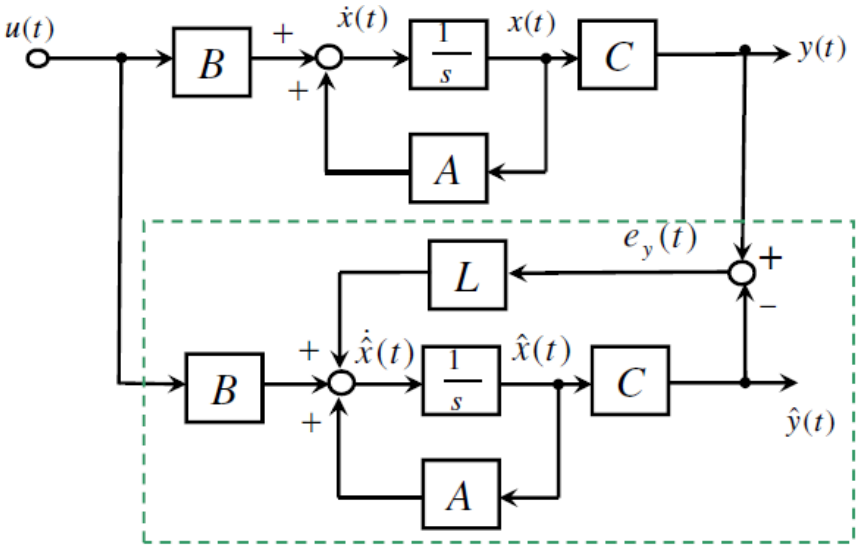

Figure 2.3 The system block diagram for general observers

Similar to observer algorithms, Kalman Filter (KF) is one of the most widely adopted strategies for state and parameter estimation since they could provide an optimal estimate for linear systems with white Gaussian noise. If the system is nonlinear or if the noise is non-Gaussian, KFs are not optimal and might suffer from divergence problems [31].

Battery modeling has non-linearity in many forms, such as the relationship between temperature, open circuit voltage and SOC. When it comes to SOC estimation, the non-linearity is mainly embodied in the OCV-SOC curve, illustrated in Figure 2.2. As a result, KF cannot be applied directly. Therefore, in the literature, various forms of KFs have been proposed such as the EKF, SPKF, [31] and CKF, [32]. The battery SOC estimation performance of EKF and CKF has been compared in [33]. The CKF outperformed EKF in terms of its estimation accuracy; however, the EKF has demonstrated better performance than CKF in terms of its computational time and complexity. An estimation strategy known as the Smooth Variable Structure Filter [34] has been applied for battery SOC estimation based on equivalent circuit models. The strategy has demonstrated fast convergence and robustness to modeling uncertainties [34]. KFs have been successfully applied to equivalent circuit-based models as well as electrochemical models. Electrochemical models are physics-based models that describe lithium diffusion inside the anode and cathode electrodes. Domenico Di Domenico in [35] applied the EKF to estimate the battery state of charge along with the lithium critical surface concentration. The details about EKF, SPKF and CKF will be explained in Chapter 6.

Electrochemical Impedance Spectrum (EIS) based Technique

A relationship between the SOC and the special value in EIS has been found in [36]. The author tried different special values in EIS, such as the intersection between EIS curve and the real axis (internal resistance R). It might not be useful due to minor variations over the 20–100% SOC interval. However, the series resonance frequency represents significant dependence on SOC. In other words, SOC could be estimated by this correlation. But, this relationship was just verified for Ni-MH and Ni-Cd batteries. A wide range of batteries need to be tested for justifying this thought.

Not only the series resonance frequency can be used to estimate SOC, but also other parts of EIS curve could be developed as an available reference to estimate SOC. The traditional way to obtain SOC using EIS is to analyze the relationship between SOC and the parameters in EIS [37] and [38]. However, it is quite time-consuming due to frequency of signal injection from 0.1mHz to 1kHz.

An alternative was proposed in [39]. Jong-Hak Lee used the correlation between the charge-transfer time constant and the SOC to figure out how much the residual SOC is. But only two specific frequencies during the process of charge transferring has been input to the batteries rather than sweeping from 0.1mHz to 1kHz. It overcomes the time issue that the traditional EIS methods were encountering.

2.3 State of Health

2.3.1 Background

State of Health (SOH) is becoming increasingly important recently, because the battery will age or degrade over time. The main consequences of aging are the drop of capacity and growth of internal resistance. The only difference between the method to estimate SOC and SOH is that SOC estimation needs rapid response, but battery's fading is a slow process. Similar algorithms to estimate SOC can be utilized, such as KF/EKF/SPKF.

2.3.2 SOH Estimation

Capacity Estimation

How to estimate or calculate the capacity and the resistances can be divided into two parts: time domain and frequency domain. For time-domain estimation, KF and EKF are popular for

estimating capacity [40]. Plett (2006) used EKF technique as a non-linear estimator. As described in SOC estimation section, its basic theory is to linearize the system by a first-order Taylor-series expansion. Actually, the EKF has the similar algorithm with the KF: substituting the linearized matrix to the KF algorithm. It is noted that the EKF is no longer the optimal solution to non-linear system, but it works well for SOH and SOC estimation.

Since SOC and SOH are normally detected simultaneously, dual EKF has been developed [41]. Two separate filters are used to estimate SOC and SOH, but they need to exchange information to make the estimation more accurate. The block diagram is shown in Figure 2.4. However, there is a problem. Battery ages at a very slow speed, for example, after hundreds of cycles the capacity maybe just decrease by a few percent. As a result, if we use same time scale to calculate the two parameters it would be overly computationally expensive. In paper [42], a special EKF called multi-scale EKF was introduced. It can be realized that the slowly time-varying parameters are adapting on macro time-scale while fast time-varying parameters are estimated based on micro time-scale, as shown in Figure 2.5.

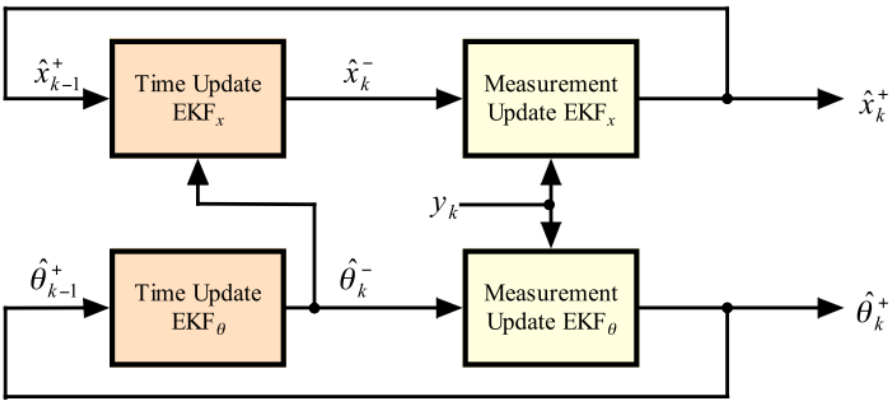

Figure 2.4 Dual extended Kalman fiter (adopted from [41])

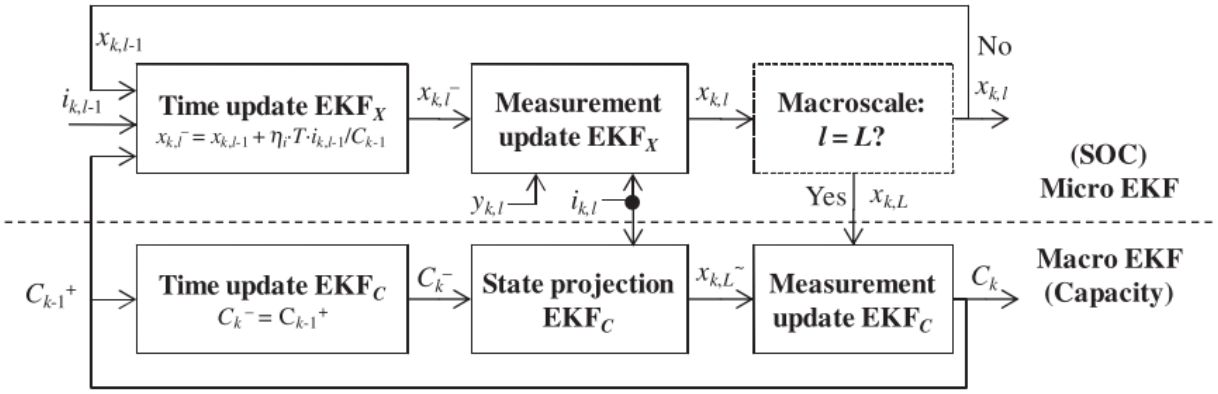

Figure 2.5 Multi-scale EKF (adopted from [42])

Resistance Estimation

Regarding resistance estimation, the KF can also be used in a joint estimation strategy [43]. A recursive least square (RLS) can be employed using a linear parameter regression equation solely for the purpose of Ohmic resistance estimation [27].

Genetic algorithm (GA) is an alternative to estimate the resistances, including resistors and capacitors. The GA relies on the computer to 'guess' the parameters within some ranges around the initialized values. According to how many initialized 'populations' and 'generations', the accuracy is different. If populations and generations are larger, the results will be more precise but it results in longer computation time. Although its accuracy is relatively higher than other techniques of estimating the resistances, GA has many disadvantages: 1) offline algorithm, a large amount of data is needed to try to reach the optimal solution, 2) high dependence on the initialization, if the initialized values are biased from the true value, it is possible that the results diverge or converge at a so called 'local minimum point' instead of 'global minimum point', 3) computationally expensive. These three main drawbacks indicate this offline technique could not be realized online.

EIS can be used off-line to estimate SOC and SOH. It has been proved as a non-destructive and reliable technique. The EIS tests are able to identify the actual origin of cell degradation processes and bring some aging effects insight, which are difficult to realize by traditional test methods [44].

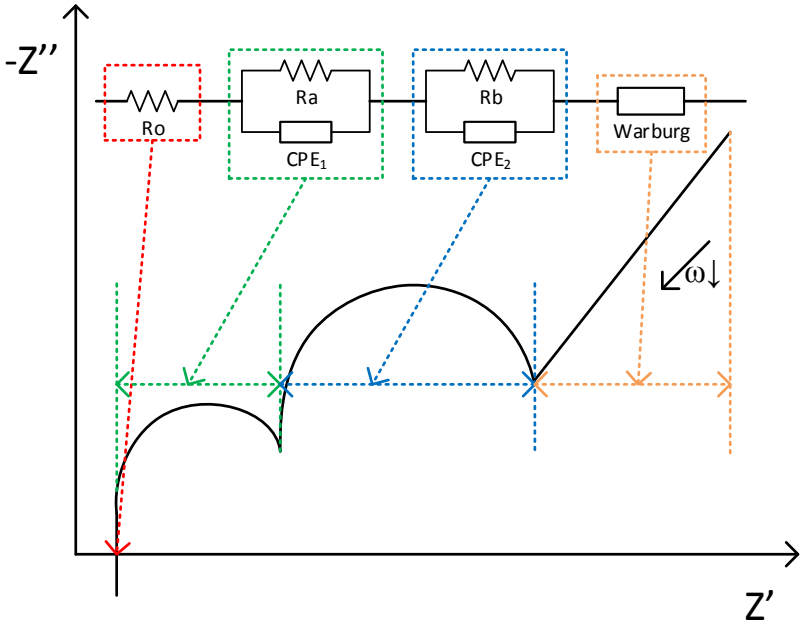

Figure 2.6 Electrical circuit presentation of EIS

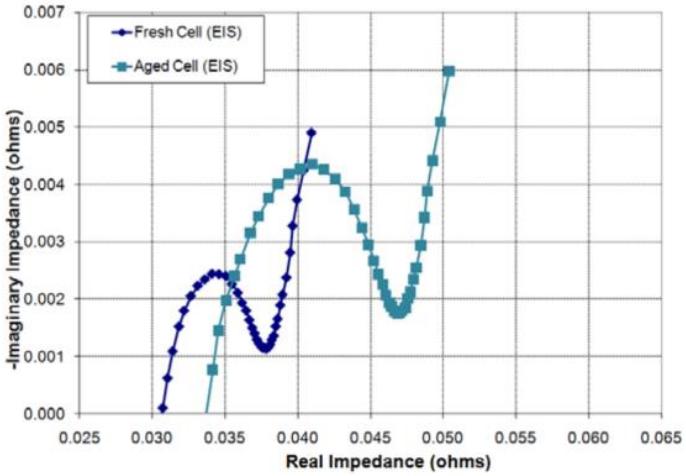

Figure 2.7 Example of fresh cell and aged cell (adopted from [45])

Figure 2.6 shows the different parts of EIS curve representing the elements corresponding to an equivalent circuit model. In paper [46], it demonstrates that the EIS curves are different when the cell is fresh or aged, as shown in Figure 2.7.

If the relationship between the levels of degradations and EIS can be found, it is easy to define when the battery should be replaced. In [45] the deterioration has a clear relationship with the parameters in the battery, such as R_1 and C_2.

The EIS tests were implemented on aging tests. Almost every critical parameter is covered in [47]. The variations of parameters that could be caused by aging include

1) Pure ohmic resistance

The results show the pure ohmic resistance varies not due to SOC changing but temperature changing.

2) Resistance on the RC pair

It has little dependency on temperature due to aging. On contrast, SOC has more influence on the resistance changing.

3) Capacitor on RC pair

Double layer capacitor is not sensitive to varying temperature; instead, it will increase with battery aging.

4) Previous history

Previous history is defined in this paper as how long after the last full charge. The study shows it has around 5% deviation between fresh cell and aged cell at resistance r_d.

The parameter effects are summarized in Table 2.2.

Importantly, the methodologies mentioned above are all off-line methods. Although off-line techniques can bring accurate results, these techniques are replaced by on-line strategies, such as Kalman filter and RLS.

Table 2.2: The summary of the dependency on SOC and temperature

<table>
<tr><th></th><th>Pure Ohmic resistance</th><th>Resistance on RC pair</th><th>Capacitor on RC pair</th></tr>
<tr><td rowspan="2">SOC increases</td><td rowspan="2">Stay constant →</td><td rowspan="2">Little decrease ↘</td><td>Stay constant for fresh cell →</td></tr>
<tr><td>Slightly changes for aged cell</td></tr>
<tr><td rowspan="2">Temperature increases</td><td>Deduce slightly for fresh cell ↘</td><td rowspan="2">Slump dramatically ↡</td><td rowspan="2">Stay constant →</td></tr>
<tr><td>Drop significantly for aged cell ↡</td></tr>
</table>

2.4 Electrochemical Impedance Spectroscopy

2.4.1 Basic Principle of EIS

The electrochemical impedance reflects dynamic characteristics. In other word, it is the response after a small signal injection of voltage or current. Therefore, there are two modes: 1) Galvanostatic mode, the direct current (DC) charging or discharging current plus an alternate current (AC) sine current

$$\Delta I = I_{\max} \sin(2\pi ft) \tag{2.4}$$

Response from voltage:

$$\Delta V = V_{\max} \sin(2\pi ft + \phi) \tag{2.5}$$

2) Potentiostatic mode, input is a DC voltage between terminals plus AC voltage:

$$\Delta V = V_{\max} \sin(2\pi ft) \tag{2.6}$$

Response from current:

$$\Delta I = I_{\max} \sin(2\pi ft - \phi) \tag{2.7}$$

For both cases, the impedance is defined as:

$$Z = \frac{\Delta V}{\Delta I} = \frac{V_{\max}}{I_{\max}} e^{j\phi} \tag{2.8}$$

In Figure 2.6, it illustrates the real and negative imaginary parts at specified frequencies, mostly from 1mHz to 1 kHz. From this figure, it can be divided into four sections: 1) the intersection of real and imaginary axis, which indicates the resistance without phase difference, 2) the inductance is the value at high frequency, 3) the semi-circle represents the R-Capacitor/R-Constant Phase Element (CPE) pair which starts at 0 imaginary axis to local minimum at around 1Hz. 4) Low frequency response. The 45° slope can be modeled as so called Warburg Impedance. These four terms indicate the electrolyte and connection resistance, high frequency phenomena, charge transfer phenomena and diffusion phenomena, respectively [48]. The detailed explanations will be covered in Chapter 5.

2.4.2 Perturbation Signals

Popkirov and Schindler [49] compared many types of excitation signals (white noise, rectangular pulses, voltage steps, combinations of overlapped sinusoid) for EIS in time domain. It is noted that the amplitude of excitation signals is limited. The reason is demonstrated as follows. If the

amplitude of stimulus is high, the cell is operating within nonlinear region. Severe problems could be caused, e.g. loss of accuracy and loss of consistency. In order to avoid the nonlinearity in current-voltage curve, the amplitude of voltage excitation signal or voltage response should be limited, normally to 10 mV.

Aperiodic Signals

Aperiodic signals, such as random signals, will cause a problem so called 'leakage' [50]. The leakage is specific term for the Fast Fourier transform based analyzers. In practice, the extent of leakage can be reduced by selection of spectral window or data processing, such as averaging the results. However, it is also a result of increased measurement time and systematical error. As a result, the aperiodic signals are not commonly used in practice.

Periodic Signals

The basic method is to apply sine wave as an excitation (current /voltage). The response at one specific frequency can be measured as a sine wave with phase difference [51] . The impedance at this frequency is calculated by voltage and current. Repeatedly, the procedure can be operated at many frequencies until the completed spectrum is obtained. The most common choices of the excitation signals are summarized in Table 2.3. According to [50], the deterministic signals (swept sine, multi sine) show the most accurate results while the noise has flat power spectrum. Even though the noise is not so, multi sine can still generate the most precise results. Besides test about the accuracy of measurement, another test considering nonlinear distortions on results has been carried out. It shows the multi sine is the best one as well. This is why most manufacturers of EIS are using multi sine as their injection signals.

Table 2.3: Summary of periodic signals

Signals	Expressions
Pure sine	$x(t) = A\sin(2\pi ft)$
Swept sine	$x(t) = \sin[(at+b)t], 0 \le t \le T$ T: measurement period $a = \pi(f_2 - f_1)/T, b = 2\pi f_1$ f_1 : *lower frequency*, f_2 : *higher frequency*

2.4.3 Fitting Techniques

There are few papers fully concentrated on the fitting algorithms for battery parameters identification. Normally least square methods and genetic algorithm are selected [52] [53]. A so-called complex non-linear least square algorithm was utilized in [54]. The details about the fitting results were not included. However, the least square algorithms may suffer from diverging or converging to a local minimum when the initialization is not effective. GA is used to evaluate the initial parameters and assist other algorithms [55]. Even though GA can accurately fit the EIS curve, the high computation complexity is not inevitable.

An ordinary least squares (OLS) has been used in [56]. The merit of OLS is that the parameters can even be estimated by analyzing a portion of the data during a period. Compared to traditional OLS, the novel OLS can be used not only under static single-frequency sinusoids, but also under a large amplitude frequency-continuous short-time excitation signal that lasts more than 4 decades. This is realized by applying a logarithmically sweeping sine-wave current. More detailed information needs to be added. Through experimental validations, the measurement time can be reduced by estimation from a part of EIS data during one period interval. In addition, high accuracy of fitting results can also be achieved.

So called multi-points impedance spectrum has been applied in [57]. Five-point impedance spectrum fitting and ten-point impedance spectrums fitting by least square have been tried in

simulation. It turns out that five-point version is accurate enough to obtain the EIS curves and the parameters for the battery. It is noted that test points should not be less than 5, which might result in the failure to fit the EIS curve. Compared to traditional methods to parameterize the battery, such as HPPC test, multi-point spectrum method is not only accurate but also non-destructive to the battery. However, how to select the interested frequencies for different types of batteries is another challenge.

There is novelty on fitting valve-regulated lead-acid battery in [58]. According to different states that batteries have, corresponding equivalent circuit models have been applied to fit the EIS curve. For example, there is battery with static state, like fully charged battery, and battery with dynamic state. The only difference between them is the Warburg impedance which is either zero or Warburg Short Terminus. Warburg Short Terminus is closer to realistic physical phenomenon than Warburg impedance [58]. But the fitting algorithm is not mentioned and the errors between measured ones and fitting ones are relatively huge, some of the parameters are fitted with 10% errors.

Chapter 3

ELECTRIC BICYCLE SYSTEM

3.1 Introduction

The popularity of the Electric Bicycles is gradually increasing. However, in Electric Bicycle application, the lack of comprehensive study on the battery and standard testing procedures/riding cycles blocks companies from optimizing Electric Bicycles battery design. In this chapter, the Electric Bicycle conversion kit is briefly discussed in Section 3.2. The details about the recorder for Electric Bicycle parameters are introduced in Section 3.3. Two standard riding cycles are defined and battery life is benchmarked in Section 3.4.

The contributions of this chapter can be summarized as follows: 1) an integrated parameter collector measurement system for both mechanical and electrical information is found and installed. For example, velocity , battery output current and power can be recorded in real time and during real road conditions, 2) two standard riding cycles are saved from the parameter collector in pure electric mode. The riding cycles are presented in both velocity and current demand formats, which can be used for modeling and designing the battery pack of the Electric Bicycle, 3) the battery life of the BionX Electric Bicycle in pure electric mode is investigated, 4) correlation between tiredness and assistance power is discussed.

3.2 Conversion Kit

The award-winning electrified kit from BionX is selected for its competitive technical specifications. The Electric Bicycle conversion kit consists of a rear wheel 350 W high torque electric motor and a 48 V 8.8 Ah battery with BMS. The electrified bike is shown in Figure 3.1. Unlike many other conversion kits, the one employed has regenerative braking for energy recapture.

Figure 3.1 Electrified bike using BionX conversion kit

3.3 Recorder of Electric Bicycle Parameters

The speed and cadence sensor is purchased from Wahoo Fitness (represented in Figure 3.2) and installed on the rear wheel to collect accurate real-life speed and cadence, a rate at which a cyclist is pedaling the pedals. It features wireless connection which enables data exporting and location capturing. The speed profile can be recorded for defined 'riding cycles' along with current and voltage from the battery pack. In addition, the grade experience by the rider can also be monitored and restored wirelessly.

Figure 3.2 The Wahoo speed and cadence sensor with magnetic piece

Figure 3.3 Data collecting system from Grin Technology

Not only mechanical data needs to be recorded but electrical information is also important to define riding cycles. As a result, additional custom voltage, current, and temperature sensing hardware and cycle analyst electronics from Grin Technology are used for the purpose of collecting real-world data and benchmarking the electric bicycle.

The data collector is shown in Figure 3.3. There are many signals that can be traced using this Cycle Analyst (CA), such as torque and temperature. They are not currently connected due to the limitation of this study. However, this tool can be extended as reference of many other studies including motor design and control. Data exportation was realized by connecting to an external SD card.

3.4 Riding Cycle Definitions

For automotive applications, driving cycles are defined by United States Code of Federal Regulations. In BMS design process, it is common to use the driving cycles to validate the proposed battery model or test proposed SOx estimators [14], [47] and [58].

The Electric Bicycle market is drawing much more attention from people. Therefore, riding cycles for helping study Electric Bicycle system and design of its battery pack should be defined as well. In this section, two standard riding cycles are defined for further study. Note that all the data was collected in pure electric mode, i.e. no human force is delivered to the bicycle.

3.4.1 Long-range Riding Cycle

First, similar with highway driving cycle which involves less dynamic behavior but more sustaining driving condition, a long-range riding cycle is defined. This type of riding cycle is suitable for constantly riding with low traffic at high speed and also applicable for riding on dedicated cycling trails that have minimal stops and traffic. In this test, the tester weighs 95 kgs

with a bottle of water. The speed profile and grade profile are shown as Figure 3.4. It lasts 35m 53s. The total distance is 12.67 kms. These data can be used to model the mechanical power if one is interested. They can be input to an Electric Bicycle powertrain model to obtain the current demand based on the specific model. As a result, it benefits designing the battery pack to satisfy the power requirement.

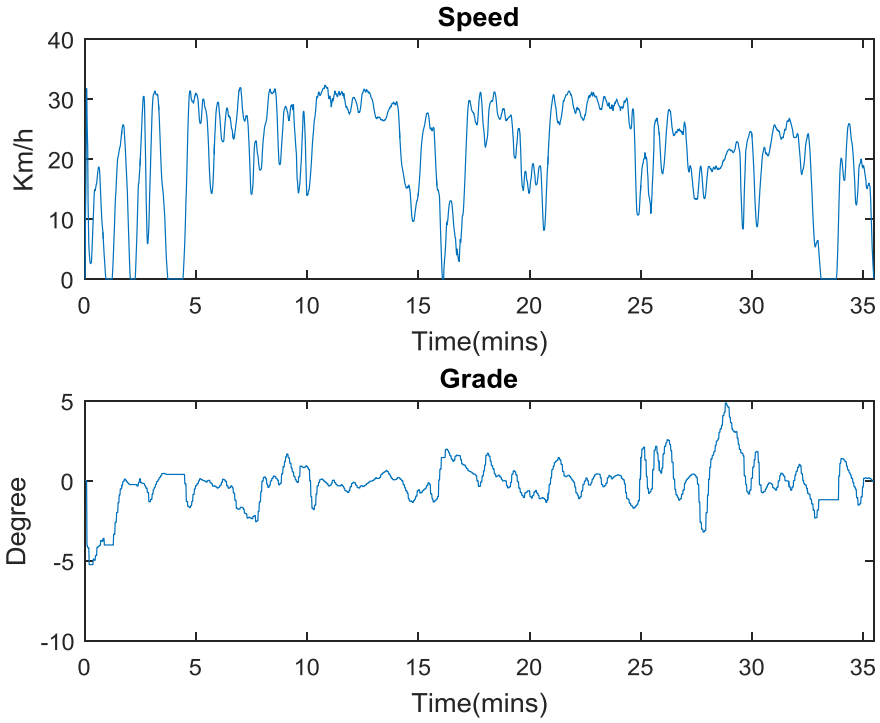

Figure 3.4 Mechanical information for the long-range riding cycle

Figure 3.4 shows the speed maintains at around 30 km/h, which is the restriction of the local law. The dynamic behavior is not significant due to low traffic. The average speed is 21.6 km/h. The electrical data including current and voltage were recorded by Cycle Analyst. The Ah consumption and pack power are shown in Figure 3.5. It is noted that this trip consumes around 4 Ah energy which is almost half of the total capacity, and 151.5 Wh. The pack voltage drops as energy is consumed. The maximum power extracted from the battery pack is 1 kW for a very

short of term, less than 3s. The constant power output is around 200 watts. The voltage response and current load in Figure 3.5 will be used for validation of the proposed battery model.

A GPS integrated in CA has captured the location information of this trip to give the readers a sense of the riding cycle, as shown in Figure 3.6. Red and green arrows represent the start point and end point of this trip, respectively.

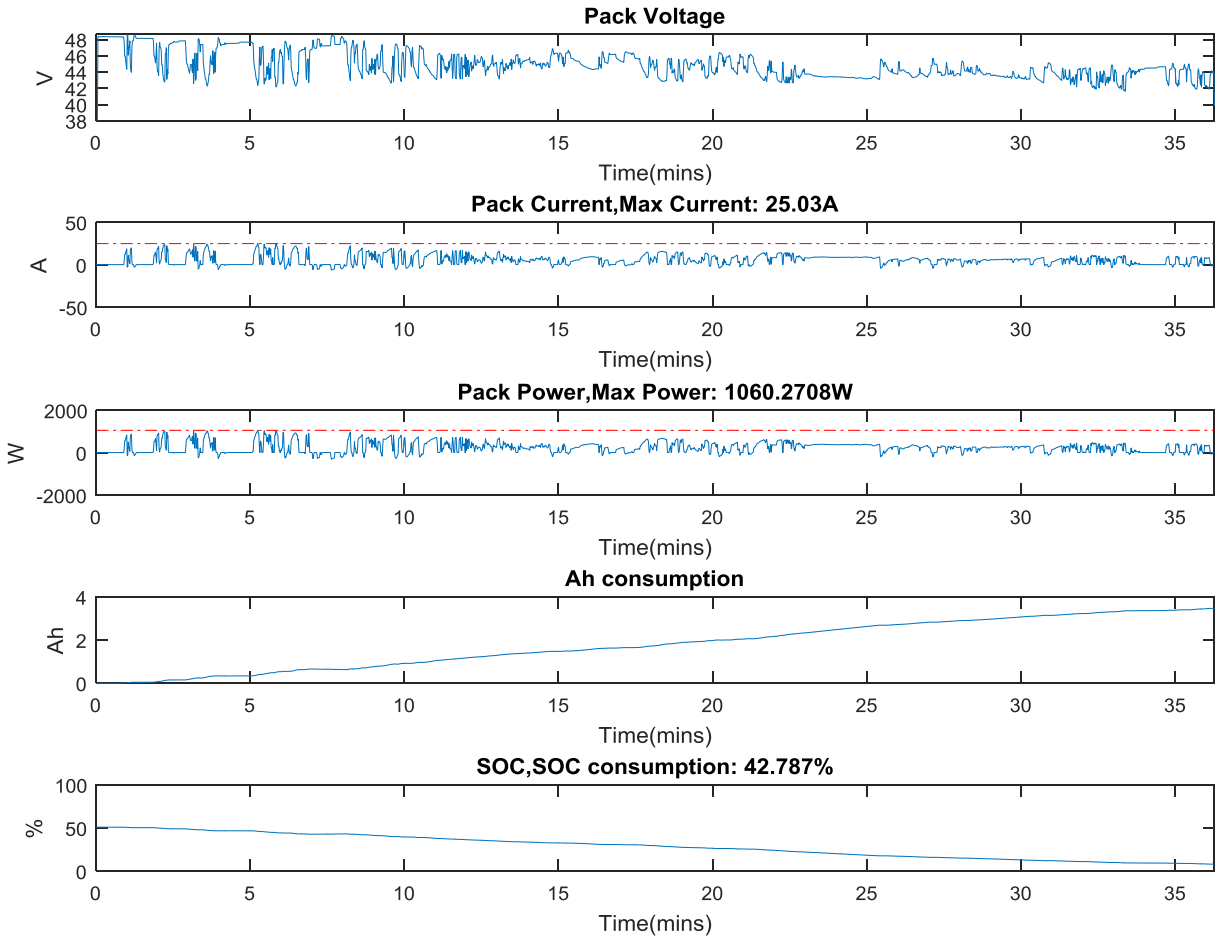

Figure 3.5 Electrical information for the long-range riding cycle

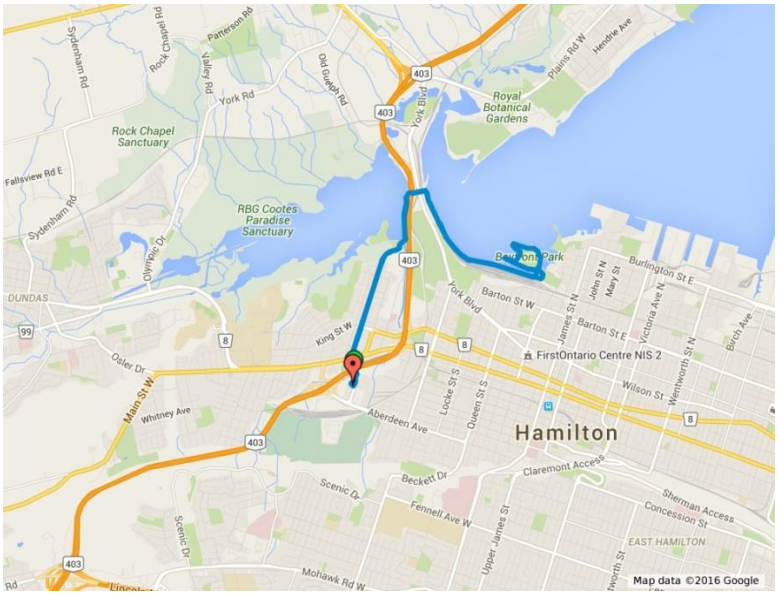

Figure 3.6 The location information of the long-range riding cycle

3.4.2 Commute Riding Cycle

The second riding cycle is defined for short range and heavy traffic. It approximates the daily commuting between work/school and home. A backpack with laptop and food inside was taken with the tester to simulate a practical heavier loading situation. The backpack weighs approximately 5 kg in addition to a 95 kg tester.

The trip is 21m 20s long and the total distance is 5.87 km. Compared to long-range riding cycle, the dynamics of the speed is more prevalent. The speed alternates between 4 km/h and 30 km/h frequently, this reflects the urban traffic conditions. As a result, the regenerative pulses and power will be sent back to the battery pack more frequently. The average speed is 16.8 km/h. It is slower than long-range riding cycle.

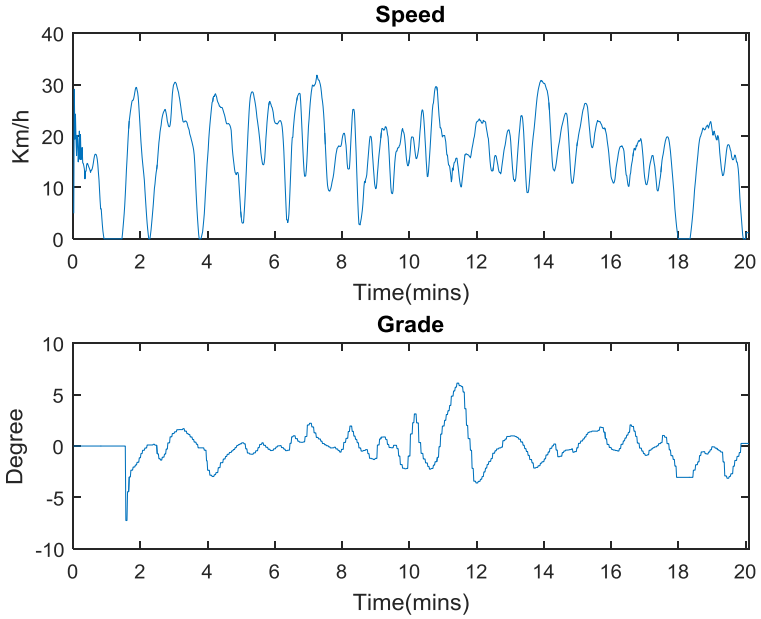

Figure 3.7 Mechanical information for commuting riding cycle

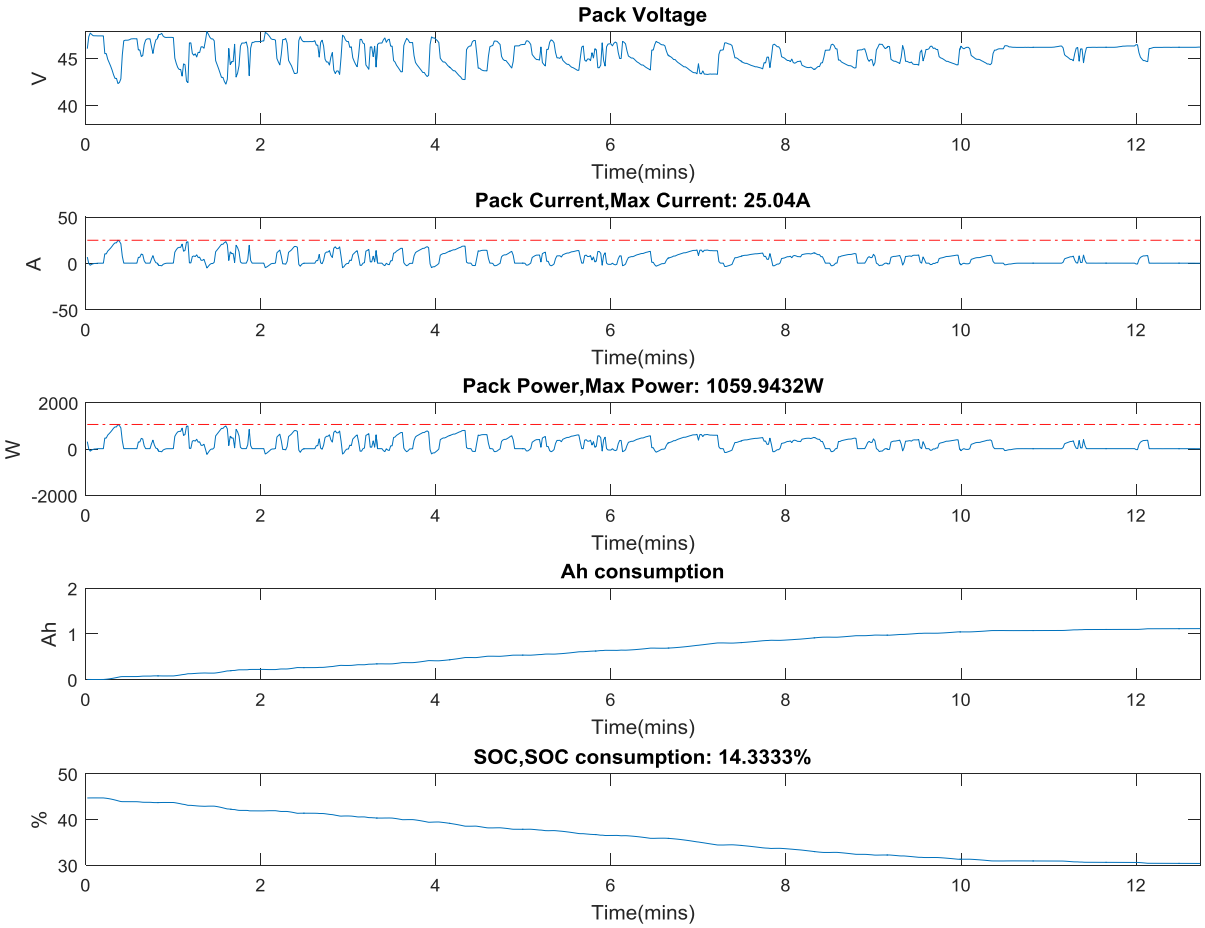

Figure 3.8 Electrical information for the commuting riding cycle

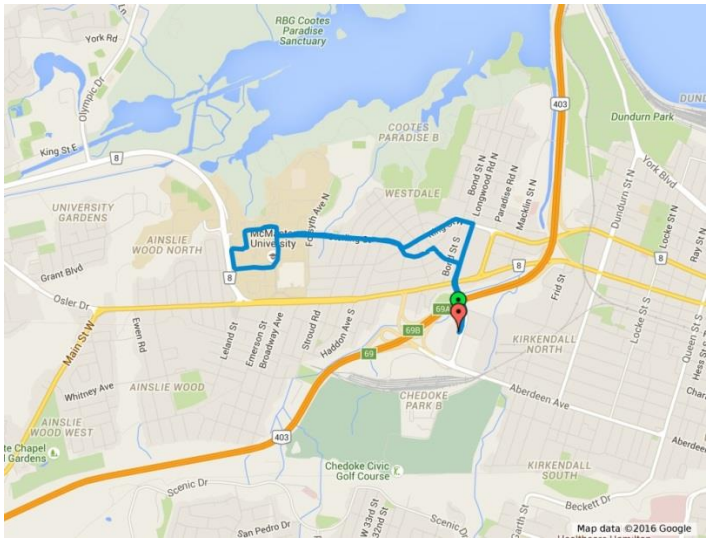

Figure 3.9 The location information of the commuting riding cycle

The phenomena of regenerative pulses can be observed from negative current and power more often, as shown in Figure 3.8. Due to the high dynamic of driving force, the pack voltage varies more dramatically. The transient high power is around 1 kW, which is as high as the one in long-range riding cycle. The high power normally occurs when the acceleration is high. However, the consumed energy is low because of shorter time and cruise range. The location records are shown in Figure 3.9.

3.4.3 Range Benchmarking

Since electric bicycles are supposed to assist people commuting and exploring, how long the battery life is and how much the energy saved from riding the Electric Bicycle are two important criteria for riders. The electric bicycle features regenerative braking and different levels of assistance from the motor. The ability of regenerating power as well as assistance levels benefits prolonging the battery life. The assistance level ranges from 35% - 300%, which refers to the different amounts of power driving from the motor. 300% level matches the peak power 1060 W captured in long-range riding cycle, since the motor is 350 W. Due to high uncertainties of

various riding styles, the battery life will be highly dependent on riding conditions. As a result, the range tests are only performed on pure electric riding. Range increases with any rider assistance/pedaling; this can be referred to as hybrid mode riding.

The test was repeated for three times to get the average range. The distance until the battery automatically shut off was recorded. The three tests are summarized in Table 3.1.

TABLE 3.1: Riding range test

Test #1	Test #2	Test #3	Avg.
29.2 km	31.3 km	30.5 km	30.34 km

It can be concluded from the table that the average battery life is 30.34 km in pure electric mode. The slight bias is caused by variance of riding behavior. It is also observed that the output power from battery remains around 200 W when the external human support is involved. However, as concluded from previous section, the transient power reaches 1 kW and will maintain around 500 W to keep driving the bike. This can explain why the bike can run longer in hybrid mode than in pure electric mode.

3.4.4 Correlation between Manpower and Tiredness

In order to quantify the saved energy and rider's tiredness from riding based on different assistance levels, the same trip is repeated five times at five assistance levels. As a reference, the energy in pure electric mode is approximated the same with the energy pedalling only consumes. This assumption will be valid when the proportion of manpower is needed, as shown in (3.1), since the efficiency on motor and transmission is counterbalanced.

$$\begin{aligned} E_{t,human} &= E_{t,battery}\eta \\ E_{i,battery}\eta + E_{i,human} &= E_{t,human} \\ Percentage &= \frac{E_{i,human}}{E_{t,human}} \\ &= \frac{E_{t,battery}\eta - E_{i,battery}\eta}{E_{t,battery}\eta} \\ &= \frac{E_{t,battery} - E_{i,battery}}{E_{t,battery}} \end{aligned} \tag{3.1}$$

where, E_t and $E_{i,battery}$ refer to total consumed energy and consumed energy from battery at i_{th} assistance level, respectively. η is the efficiency of the motor and transmission.

This benchmarking test is to investigate a) the relationship between riding effort and tiredness, b) the consumed energy at each assistance level. The test is performed in the same route, i.e. the distance and road condition were approximately identical. Trip information at assistance level 4, including mechanical and electrical data, is recorded by sensors, as shown in Figure 3.10. The grade is an important factor for other research areas, e.g. systematically modeling the Electric Bicycle and friction. The energy and SOC consumptions and proportion of manpower at each assistance level can be extracted from Figure 3.10 - Figure 3.15. They are summarized and compared in Table 3.2. The 'Pure Assist' column is assumed as pure manpower to be compared with, explained in (3.1). Additionally, tiredness is assessed from the feeling of testers.

The percentage of tiredness shows the tiredness equivalent to x% of pedaling only riding. For example, 40% means that the feeling of the rider is similar with the feeling of pedaling only for 40% total distance. The higher percentage refers to approaching nonassistant bikes which consume manpower.

It can be observed from Table 3.2 that higher assistance levels offer more energy from battery/motor. The lower manpower engaged decrease the tiredness. 'Pure Assist' and Level 4 can significantly decrease the proportion of manpower, leading to less tiredness.

TABLE 3.2: Important indicators at each assistance level

Assistance level	**Level 1**	**Level 2**	**Level 3**	**Level 4**	**Pure Assist**
Energy from battery (Wh)	7.50	10.87	15.89	26.55	33.94
Manpower (%)	77.9	67.97	53.18	21.77	0
SOC consumption (%)	1.89	2.81	4	6.8	9.09
Tiredness (%)	80	60	40	20	0

However, energy-wise speaking, these two consumed approximately 1/10th total energy of the battery. To search for a balance between consumption and comfortability, Level 3 with around 50% manpower is optimal in terms of energy and tiredness from users' point of views. It is conjectured, there exists an optimal combination of assistance level and rider effort for each rider. Such investigation is beyond the scope of the current thesis and can be explored in future.

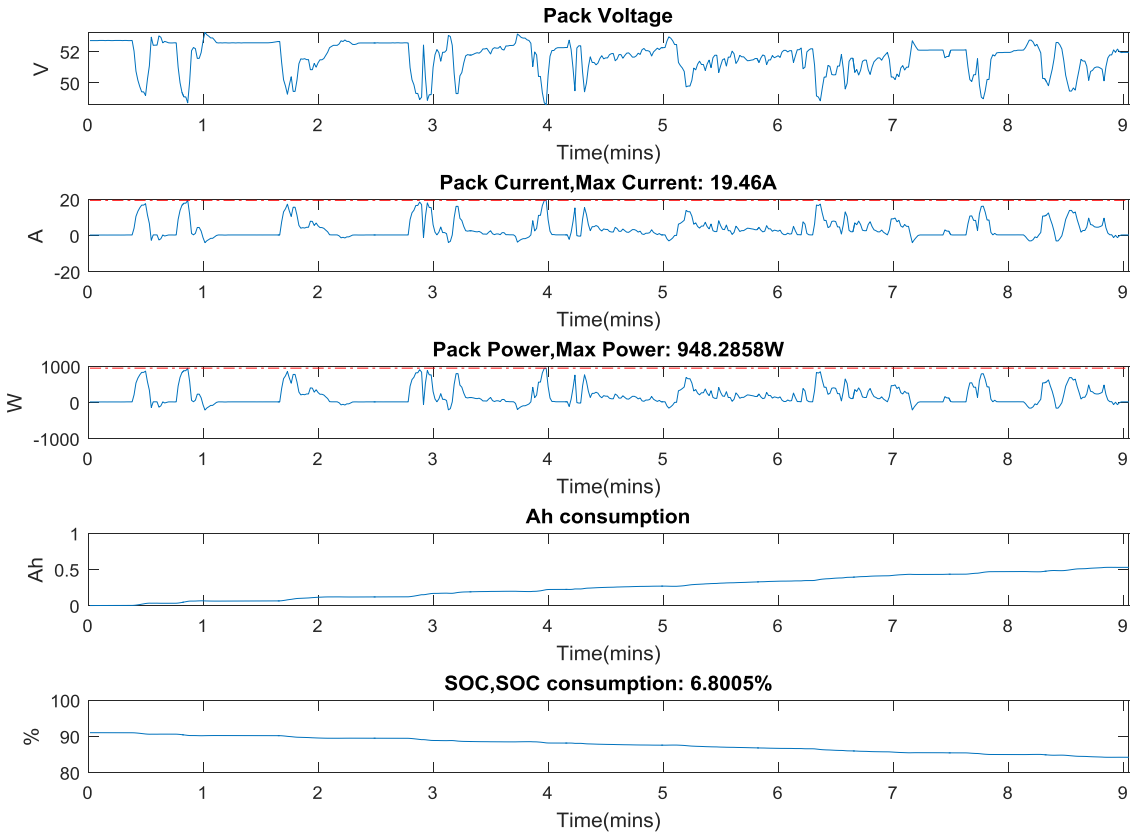

Figure 3.10 Electrical information at Level 4

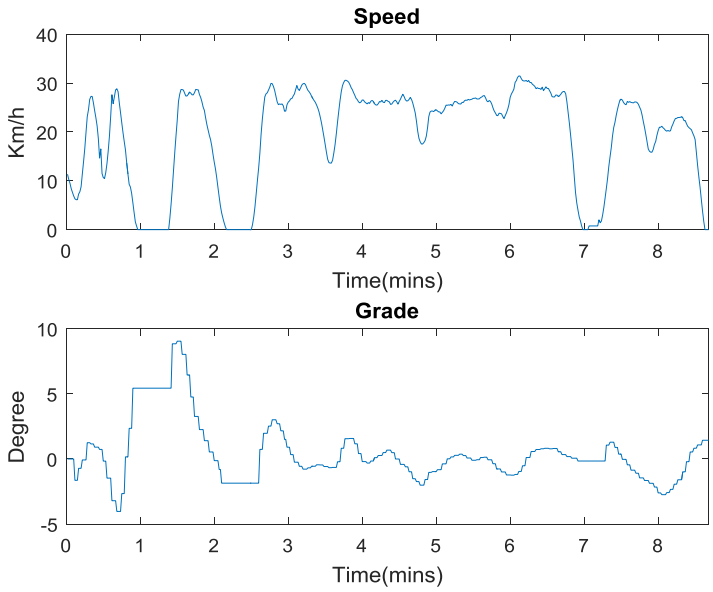

Figure 3.11 Mechanical information at Level 4

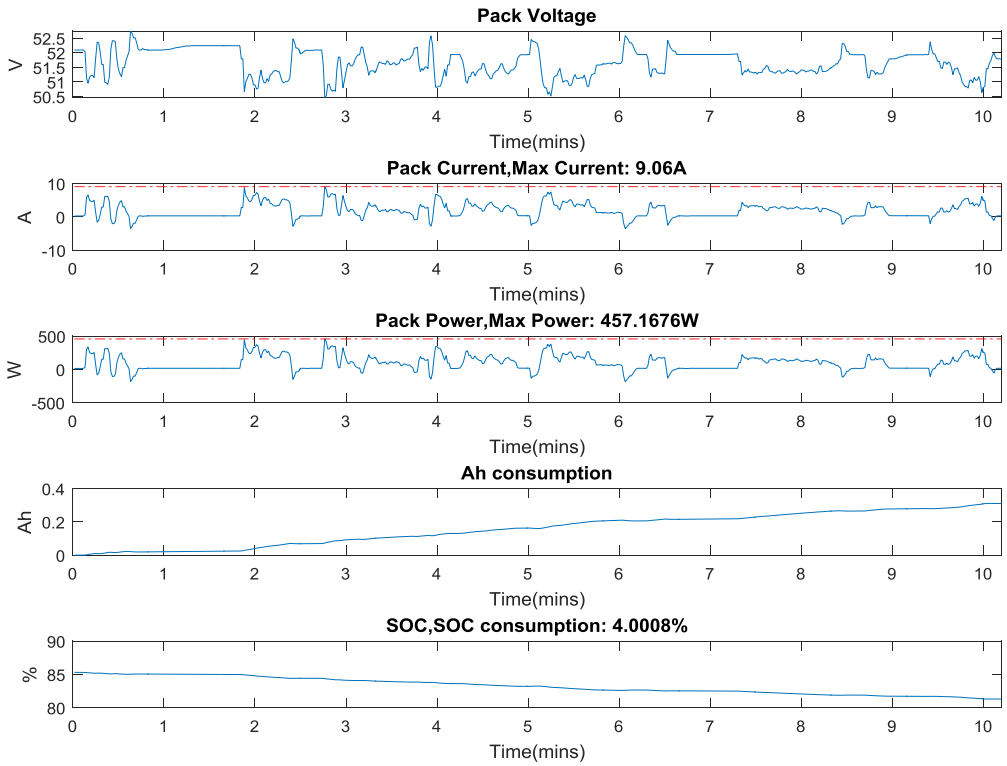

Figure 3.12 Electrical information at Level 3

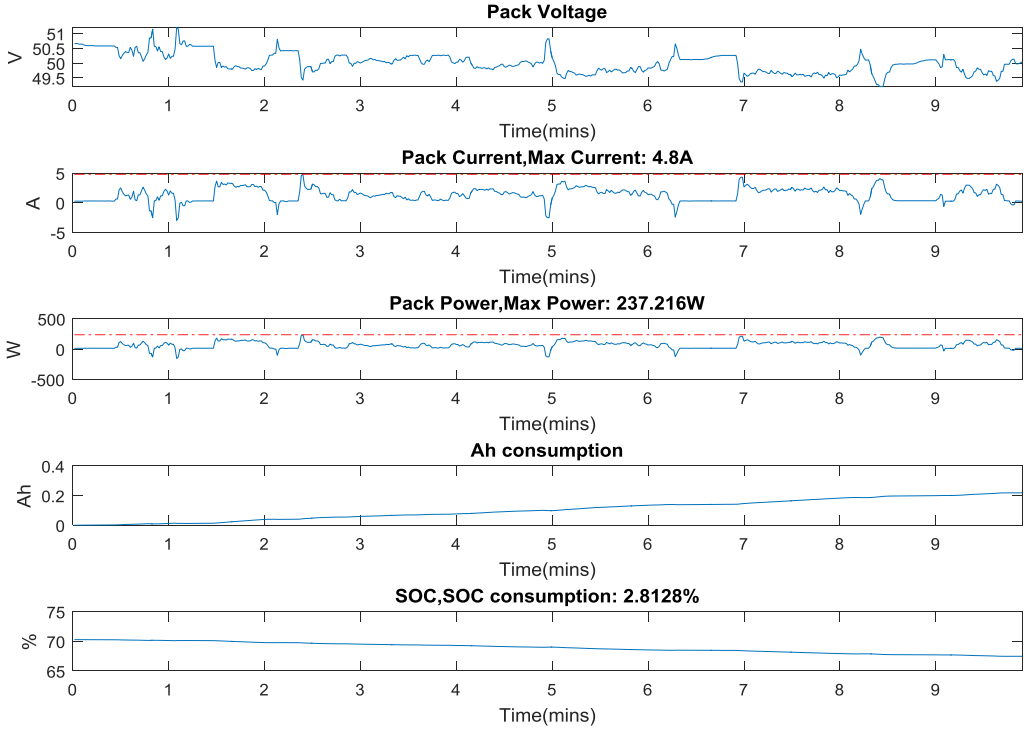

Figure 3.13 Electrical information at Level 2

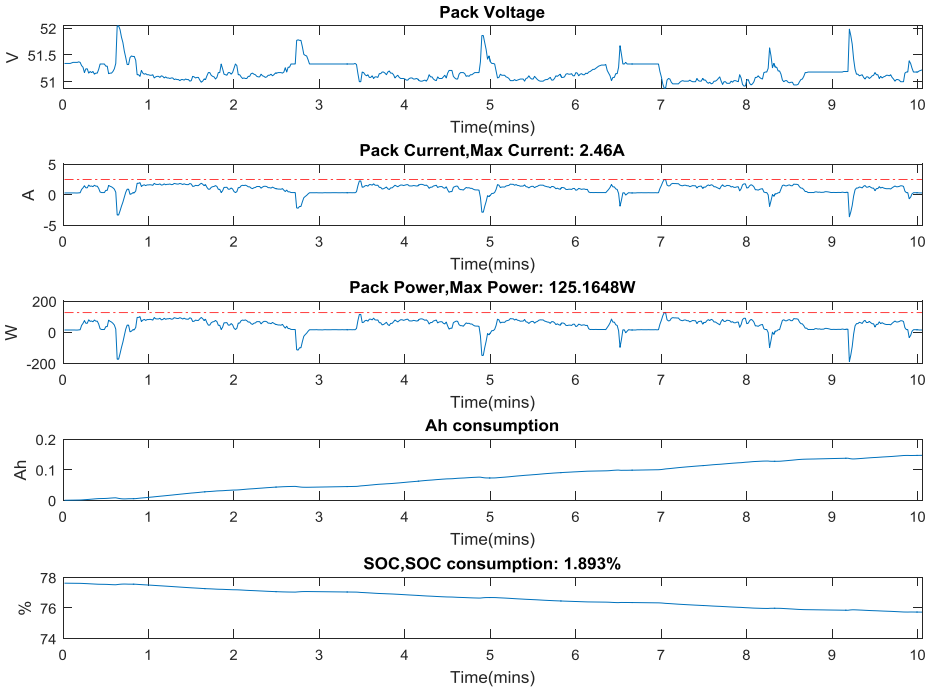

Figure 3.14 Electrical information at Level 1

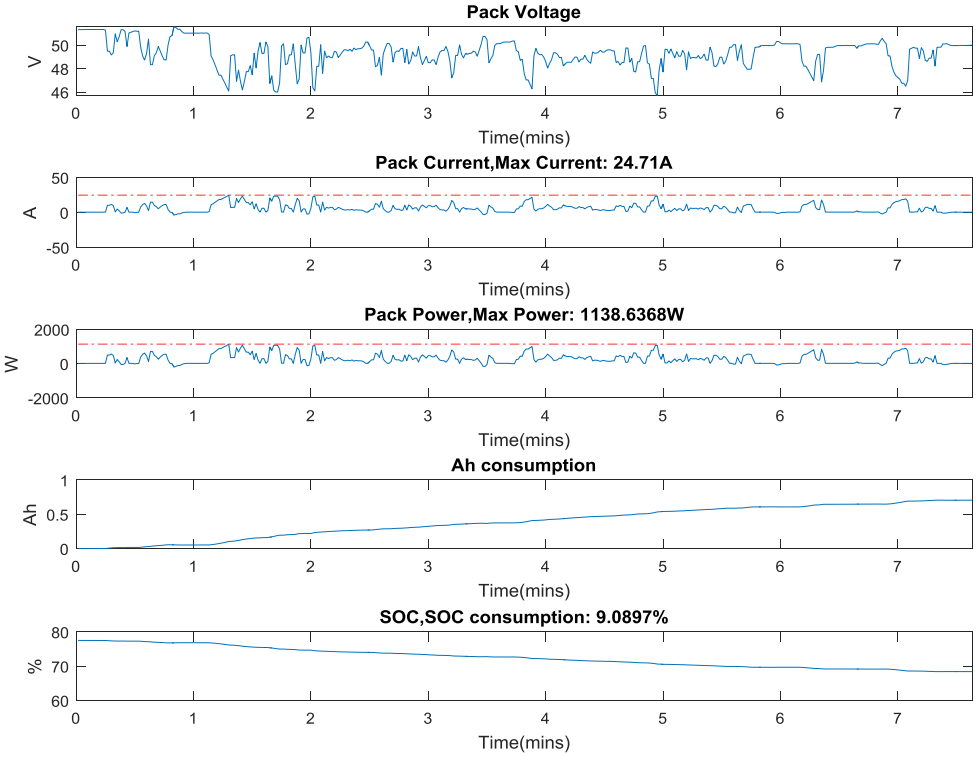

Figure 3.15 Electrical information in pure electric mode

3.5 Conclusion

A complete data acquisition system for the Electric Bicycle was installed. The system is able to record nearly all the basic parameters included in this Electric Bicycle, e.g. speed, cadence, battery current, battery voltage, etc. It enabled and achieved the collection of battery-side information for the purposes of battery model validation and e-bicycle benchmarking.. More wiring is needed for temperature, throttle or motor power measurements. This system will benefit other researchers who are interested in Electric Bicycle application.

Two standard riding cycles were defined based on the recorded data from the data acquisition system. Both mechanical and electrical riding cycles were represented. The mechanical riding cycles consisted of velocity and grade profiles. The electrical riding cycles composed of current and voltage profile give guidance of designing or testing Electric Bicycles battery pack. In this thesis, the extracted current and voltage profiles were used to validate a fitted battery model; this will be explained in the Chapter 4.

Two benchmarking tests are performed on the electric bicycle system: a) the range every fully charge is determined in pure electric mode. The average range is acquired as 30.34 km per ful charge, b) the relationship between the manpower and tiredness has been approximately quantified.

Chapter 4

TIME DOMAIN EXPERIMENTS AND CHARACTERIZATION

4.1 Introduction

A variety of researchers present and apply their fitting results of battery modeling using time-domain and/or frequency domain experiments; usually exclusively either in time-domain or frequency-domain. However, the commonly used optimization algorithms are highly dependent on initialization, such as fmincon, which leads to impossibility of full SOC range fitting. Instead, the fitting tools have to process the experimental data pulse by pulse. It is either time-consuming or inaccurate when the initialization is unreasonable. As a result, it is necessary to develop an alternative algorithm to improve this phenomenon.

This chapter is organized as follows. Capacity test and its results at ambient temperatures ranging from -10 – 20 ºC are described in Section 2. In Section 3, time domain experiments and its simulated tests are explained. The detailed fitting algorithm is presented in Section 4. A sensitivity study and experimental fitting results are shown in Section 5. In Section 6, this chapter is concluded.

The main contributions in this chapter are described as follows: a) a novel quadratic programming based optimization algorithm is proposed and developed at both single and multiple SOC points without initialization. b) Other features, such as current-dependent nonlinear resistance and asymmetric charging and discharging impedance, are included in time

domain parameter fitting to improve the fidelity of the fitting algorithm. c) The effect of measurement noises on HPPC data was investigated. d) User-friendly interface is developed to integrate proposed functionalities for time domain fitting algorithm. A subset of the work in this chapter is part of publication [60].

4.2 Capacity Test

It should be noted that the capacity test, HPPC test, and EIS test are performed in Dr. Gauchia's research group, Michigan Technological University, Houghton, Michigan, United States. The detailed experimental procedures please refer to Appendix.

4.2.1 Theory

Although the BOL rated capacity is normally shown in battery's datasheets, the difference between measured and rated capacity is still observed. The capacity is very sensitive to SOC and temperature, the actual capacity from this test is used in HPPC and EIS at corresponding temperatures and SOC levels.

Table 4.1: Comparison between rated capacity and measured capacity

	Capacity @ 20 ºC	**Capacity @ 0 ºC**
Rated	8.8 Ah	80%×8.8Ah = 7.04 Ah
Measured	8.187 Ah	7.95 Ah

The whole process starts with at least 1 hour resting from fully-charged state to upper-limit voltage. Once the lower-limit voltage specified by manufacturers is reached, followed by a default rest at open circuit voltage, a cycle of capacity test is finalized. The cycle is required to repeat up to 10 cycles until three consecutive discharging capacities are converged within +/- 2% [61]. The capacity is calculated by (4.1) [62].

$$C = \int_{t_1}^{t_2} \frac{idt}{3600 / (SOC(t_2) - SOC(t_1))} \tag{4.1}$$

Where, 3600 stands for converting Ah to As, t_2 and t_1 represent the end and beginning of the test. Typically, $(SOC(t_2) - SOC(t_1))$ is equal to 1 since the battery is from fully charge to fully discharge.

4.2.2 Experimental Setups

The test is based on the battery pack from the Electric Bicycle. It consists of 13S14P Samsung ICR19650-22P-2200mAh cells. 13S4P construction indicates 4 cells in parallel and 13 modules in series, as shown in Figure 4.1. This battery pack should have a nominal capacity of 8.8 Amp-Hour (2.2 Ah per cell). Capacity tests were performed for both charging and discharging at different temperatures. Besides the pack voltage, continuous current, temperature from different locations in the pack and time were recorded. There were two sets of measurements recorded for each testing, 1) the battery tester recorded data (time, current, pack voltage and power), 2) the dedicated NI DAQ device, which measured and recorded module voltages for three modules, five temperature sensors and pack current from a hall effect sensor.

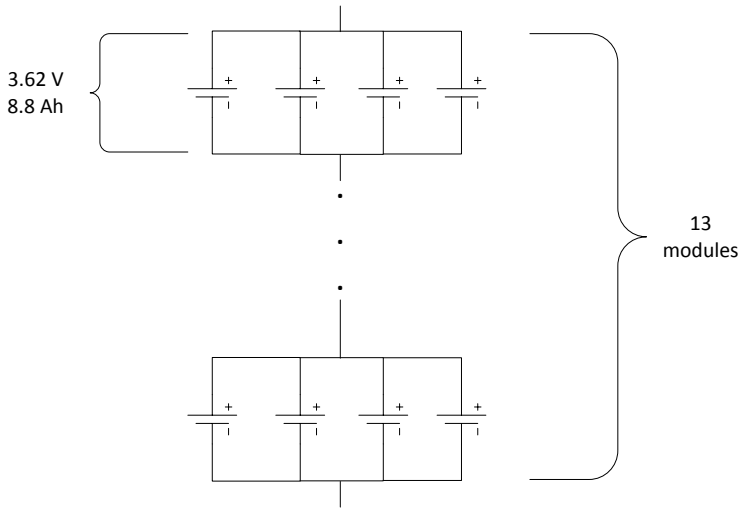

Figure 4.1 Configuration of the BionX Electric Bicycle battery pack

The following variables are of interest and were recorded during test: voltage, current, time and temperature. This test is the very first test before any further experiments (HPPC, EIS).

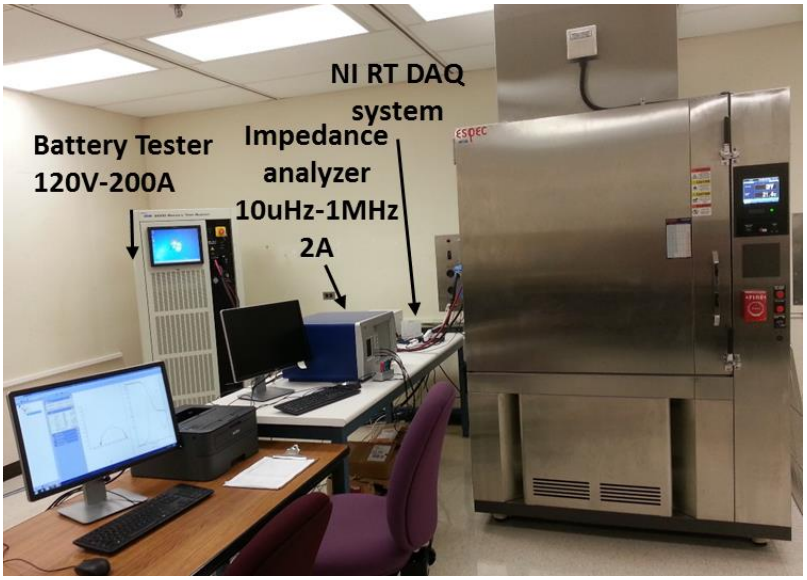

Figure 4.2 The experimental set ups

4.2.3 Experiment Results

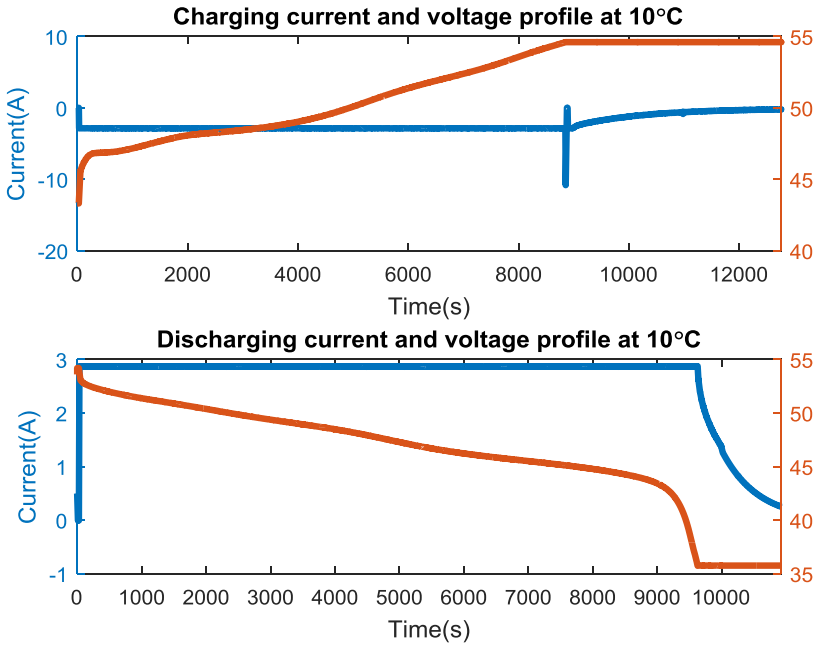

Figure 4.3 Example capacity test profiles for both charging and discharging at 10 ºC

An example measurement profile at 10ºC is depicted in Figure 4.3. The small overshoot on the top graph at the beginning of constant voltage (CV) mode is caused by controller overshoot in the tester. Based on the descriptions of the experiment above, charge capacity and discharge capacity at each temperature can be calculated by integrating the current measurement during each period of test, as derived from (4.1). Results from a built-in capacity calculator in battery tester are compared with the calculated ones in Figure 4.4.

As the CV mode ends, the total capacity can be captured at the end of the each cycle. It can be seen from Figure 4.4 that the calculated and measured ones are similar.The difference could be either the result of compensation mechanism in the battery tester or the accumulated error of current measurement. Due to uncertainties of these factors and for similicity, the calculated ones are applied for further study.

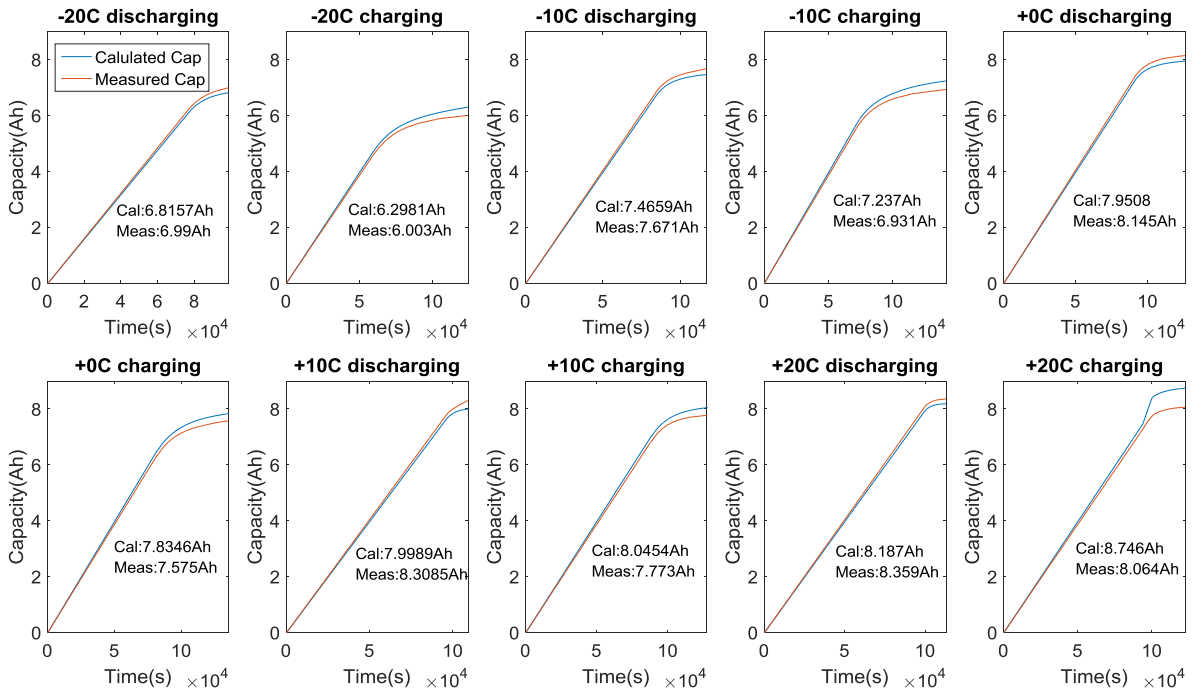

Figure 4.4 Discharge and charge capacities at each temperature of interest

The 3D relationship among temperature, SOC and pack voltage is given in

Figure 4.5 and Figure 4.6. In this case, SOC is a function of temperature T defined as follows:

$$SOC(T) = {CAP_{residual}(T)}\Big/{CAP_{total}(T)} \tag{4.2}$$

where, $CAP_{residual}$ indicates the current capacity. CAP_{total} is the total capacity at the corresponding temperature T.

In addition, a 2D relationship among them is shown in Figure 4.7 and Figure 4.8 to show the effect of temperature on the battery usable capacity. Concluded from these plots, the capacity will be significantly affected by the temperature. The trend is that total capacity is decreasing with temperature. The same phenomena/trend has been observed by other researchers for a variety of chemistries [63] [64].One of the main reasons is that Lithium Ions are resisted from

flowing since kinetics of the ions are slower at lower temperatures. At very low temperatures liquid electrolytes can be frozen, which dramatically increases Li-ion flow resistance. The capacity usage can be summarized in Table 4.2. A look-up-table of capacity will be created in in a battery model. It should be noted that selecting -20 ℃ - 0 ℃ benefits understanding the behavior of the battery pack even though this temperature range is not practical or true usage of the electric bicycles.

Table 4.2: Discharge and charge capacity at different temperatures

Temperature (°C)	-20	-10	0	10	20
Charge CAP (Ah)	6.2981	7.237	7.8346	8.0454	8.746
Discharge CAP (Ah)	6.8157	7.466	7.95	7.9989	8.187

The reason why charging capacity is smaller than discharging capacity is the battery was over discharged at low temperature due to the failure of overdischarging control. This problem should have been fixed, but due to the limitation of the time for the experiments it was not realistic to re-do these capacity tests at that time.

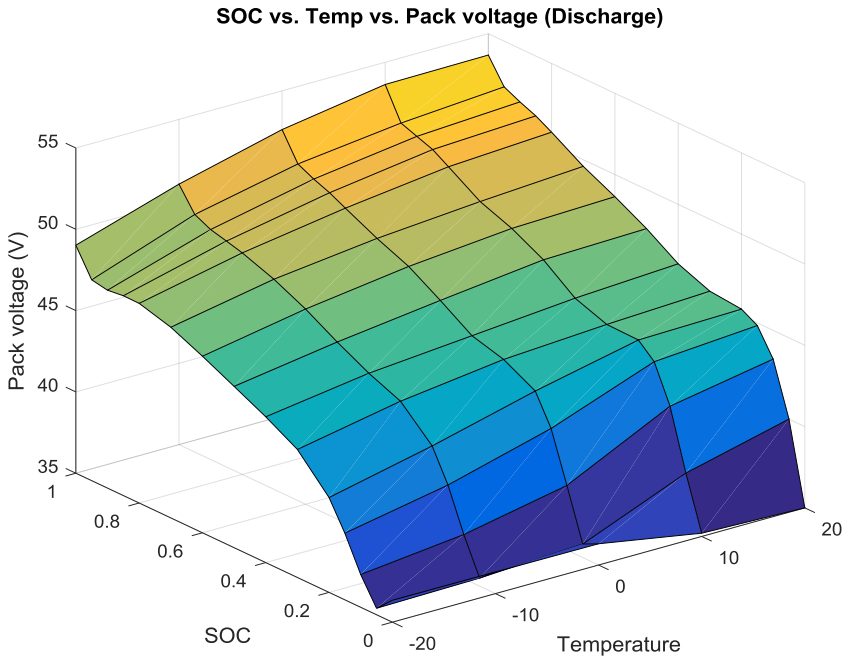

Figure 4.5 Relationship of temperature, SOC and pack voltage for discharging the battery

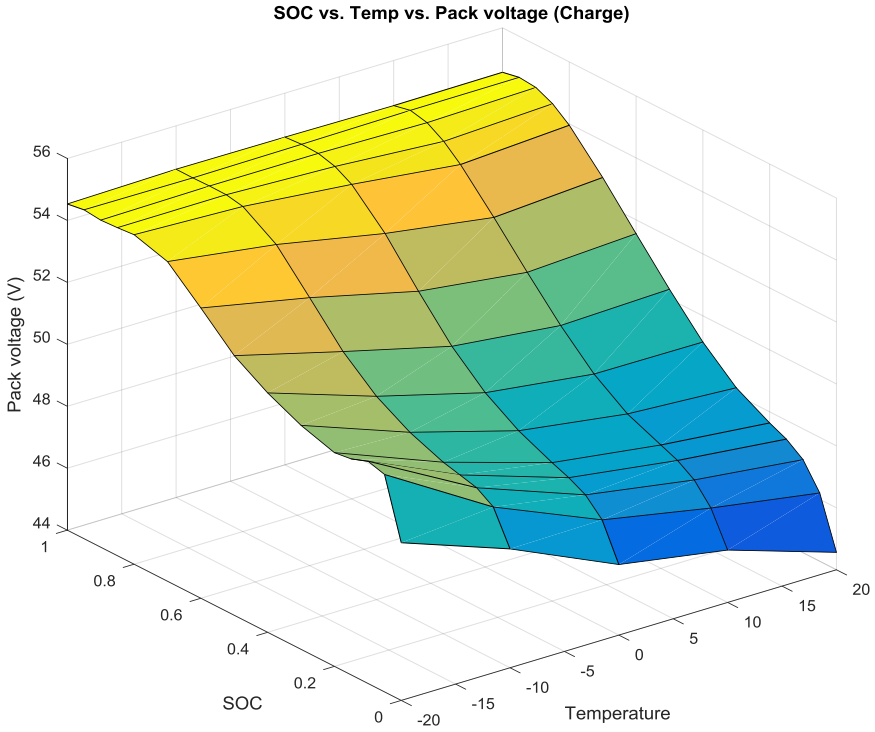

Figure 4.6 Relationship of temperature, SOC and pack voltage for charging the battery

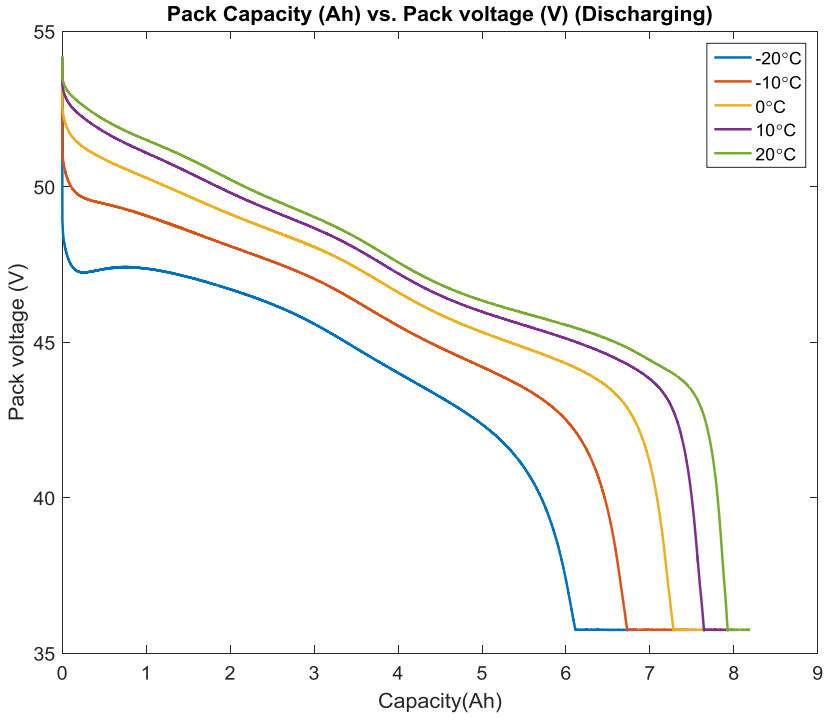

Figure 4.7 Capacity versus pack voltage at different temperatures for discharging the battery

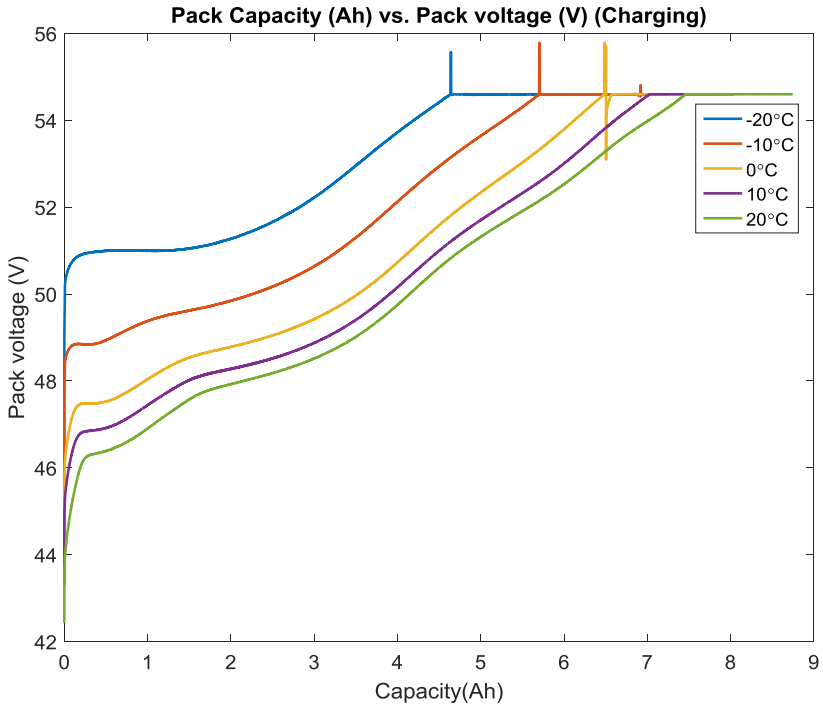

Figure 4.8 Capacity versus pack voltage at different temperatures for charging the battery

4.3 Time Domain Experiments

4.3.1 Hybrid Power Pulse Characterization

The HPPC test is intended to determine dynamic power capability as well as identify parameters. The procedure applies 10-40 s constant current discharge and regenerative (charging) pulses separated by rest periods, at each SOC level and temperature of interest. At the same time, voltage response will be recorded [61]. Typical desired responses are shown in Figure 4.9 a). Ideally the voltage response is desired to be within voltage limits and not be clipped. Some level of guesswork is used to determine the magnitude of the constant current pulses, particularly at the extreme operating points. Usually HPPC employs conservative current pulses.

Figure 4.10 illustrates the time domain battery ECM model and how certain elements relate to measured voltage responses. The blue line denotes the voltage response from a constant current pulse. It can be derived that the battery ECM model can be divided in two responses: instantaneous voltage drop/increase excited by ohmic resistance, and dynamic voltage decay/growth triggered by RC pairs [65]. The number of RC pairs can be chosen as many as desired to achieve sufficient accuracy [66].

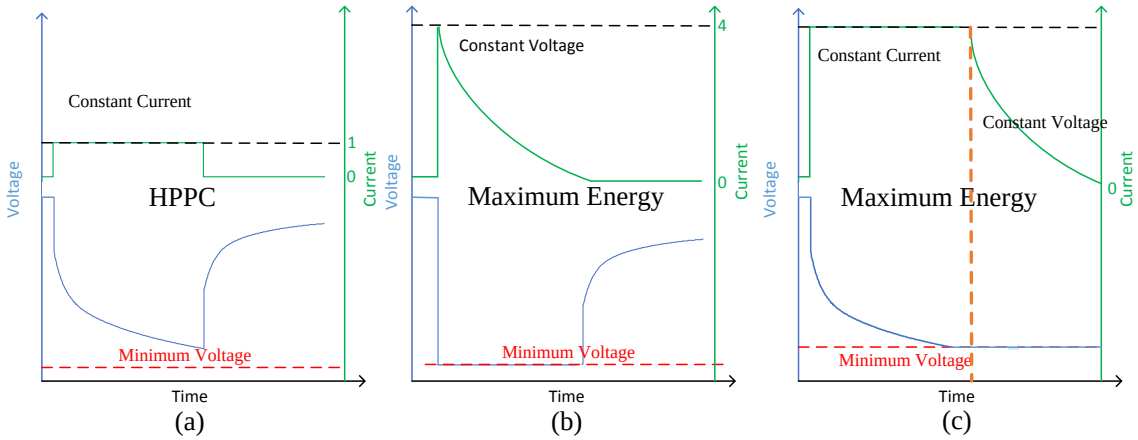

Figure 4.9 Diagrams of voltage response and current pulses for (a) HPPC and (b) and (c) MEP test

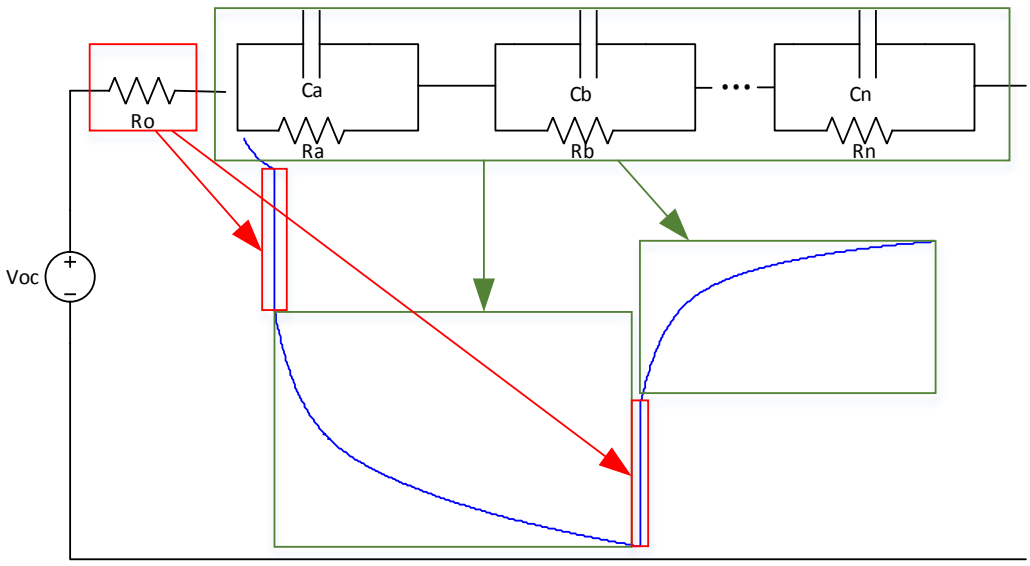

Figure 4.10 Time Domain Equivalent circuit model

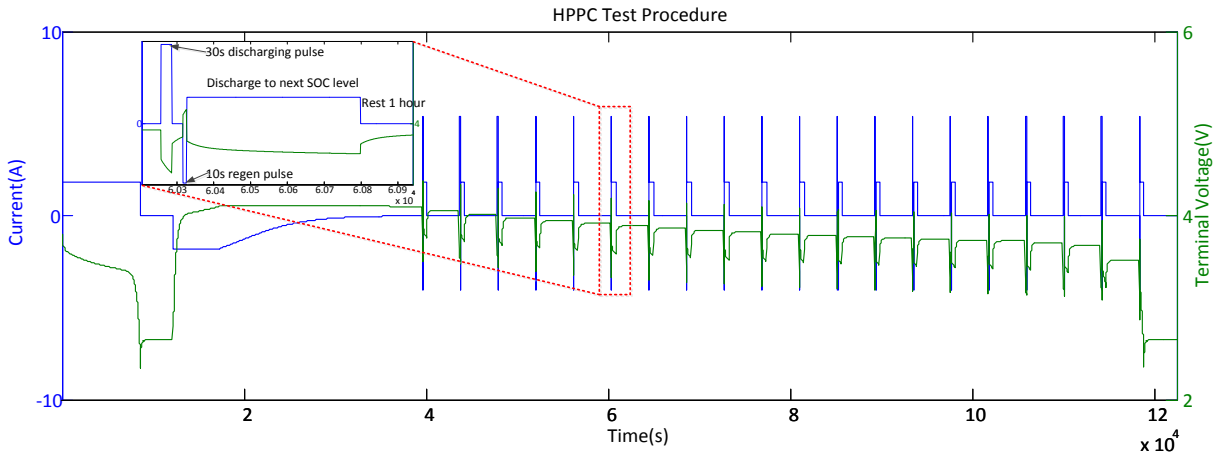

Figure 4.11 HPPC test discharging sequence

4.3.2 Maximum Energy Pulse Tests

The MEP test is applied such that the battery is operated at its maximum limits during the duration of the pulse. The same pulse duration as with HPPC is used. The battery is charged/discharged at its maximum current until the voltage limit is reached, then a constant voltage condition is held there for the remaining duration of the pulse. Integrating power during such a pulse results in the maximum energy the battery can provide during that pulse. Benefits of doing MEP test are that it avoids determination of appropriate current magnitudes, and can directly yield conservative power capability by using the power measured at the end of the pulse. An idealized response predominately in constant voltage mode in illustrated in Figure 4.9 (b).

This test is roughly same with HPPC test, the only difference is the discharge and regen current pulses. Those pulses are replaced by maximum discharge and regen current instead of 1 C-rate and 0.75 C-rate. Note the maximum instant discharge/regenerative current amplitude are not given in battery datasheet. But referring to the maximum continues discharging current mentioned in the datasheet, the maximum instant discharge/regenerative current is chosen as 10 A.

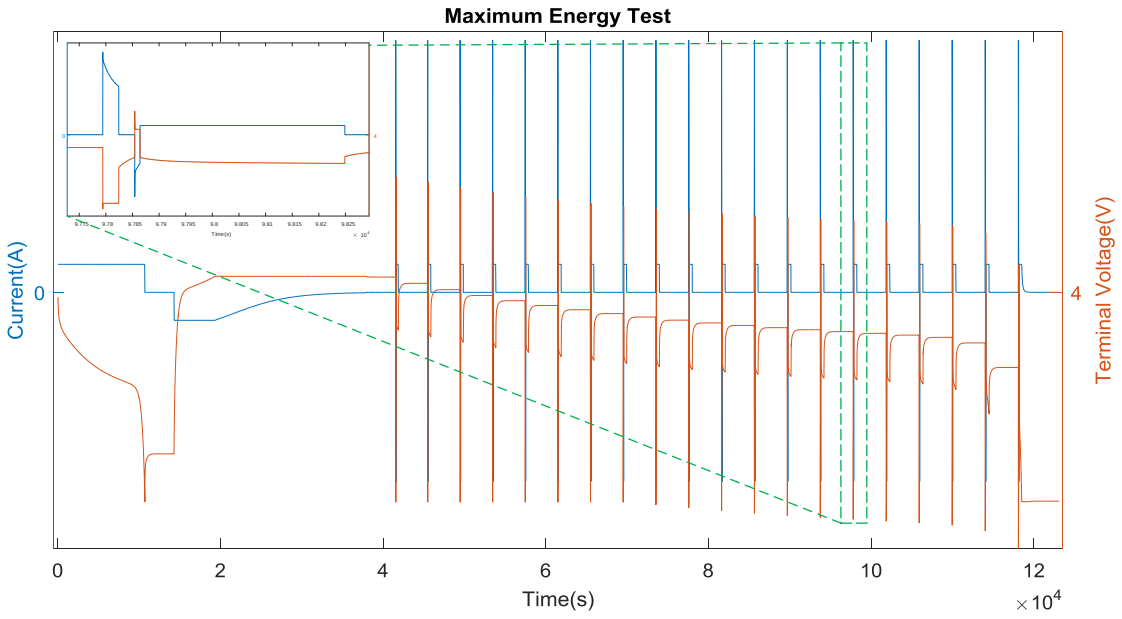

Figure 4.12 MEP test discharging sequence

These max current pulses will lead to two possible results: (1) when the voltage reaches its limit value before the current does, the battery will remain in constant voltage mode, and the current will fade slowly. Because the current fades, the constant voltage mode will never be converted to the constant current mode. (2) When the current reaches its limit value before the battery voltage does, the battery will maintain a constant current state, and the voltage will continue to change slowly. The constant current mode will be converted to the constant voltage mode once the voltage reaches the limit value.

4.3.3 Simulated Time-Domain Power Capability Testers

The motivation of having simulated HPPC and MEP results is to enable sensitivity study of fitting algorithm, perform model validation, and help design the HPPC/MEP test procedures.

The whole simulated testes are finalized by ‘State Flow’ tool box in MATLAB/Simulink, shown in Figure 4.13. The PI controller is used to gradually adjust the current to zero when the voltage is constant (CV mode). There is a smart switch between PI controller and current generator in

State Flow block. It enables the current from PI controller when the battery is under CV charging mode. The addition of noise is used for SOx sensitivity study that is described later in the thesis. The battery model consists of 1-3 RC pairs. It will be described comprehensively in Chapter 4.

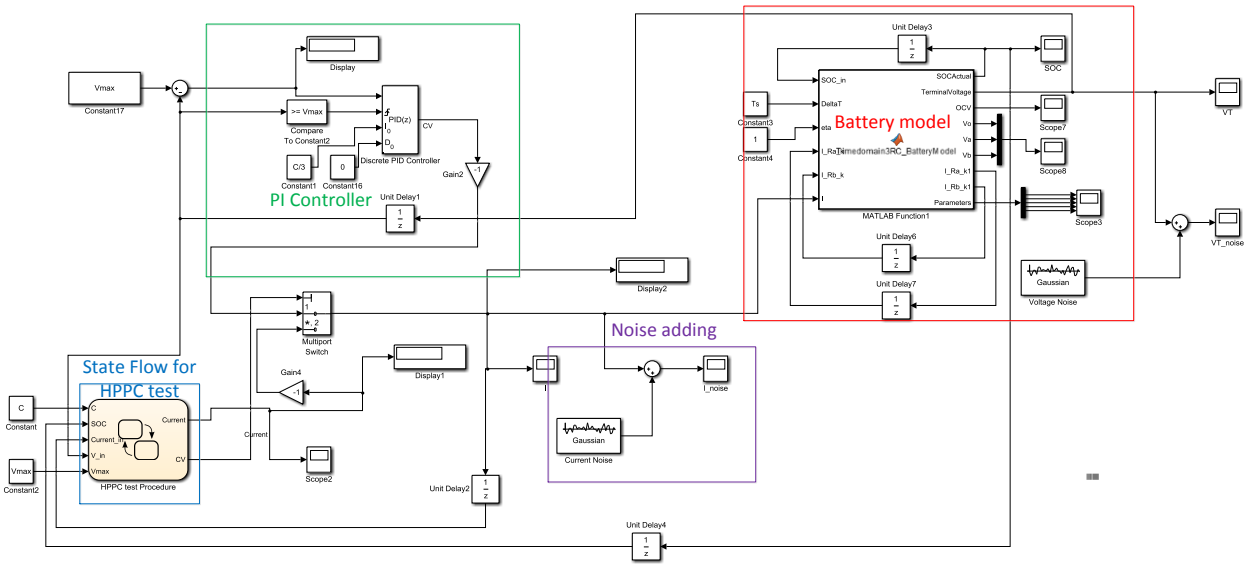

Figure 4.13 MATLAB schematic of HPPC tester

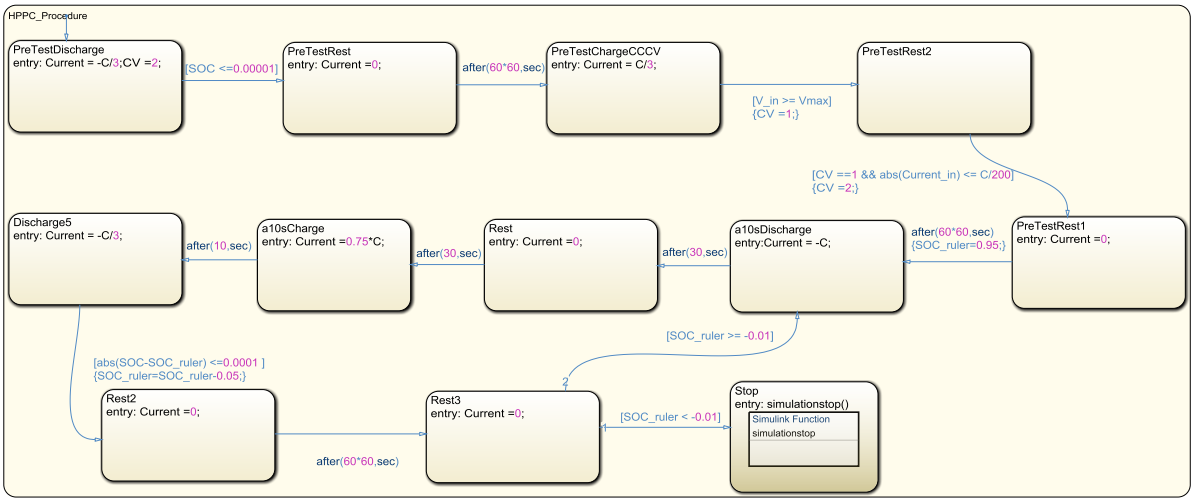

Figure 4.14 State flow of HPPC tester

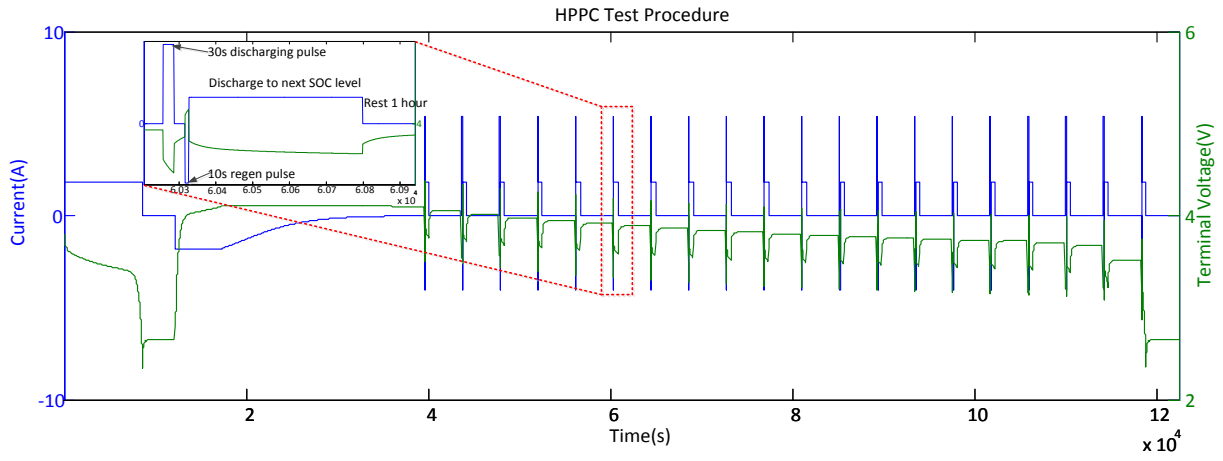

Figure 4.15 Inserting current signal and voltage response

The state flow block is following the HPPC/MEP procedure described earlier in the chapter.. The C-rate can be tuned based on different capacities of the battery. This block features smart stop. It means whenever the battery voltage hits the lower or higher limit, the signal generator will switch to CV mode to protect the battery from over discharging/charging.

Compared to HPPC signal generator, the maximum energy tests require not only the CV mode for discharging but also for charging. Because each discharging and charging current pulse will make the voltage reach either highest or lowest voltages. Once it happens, the CV modes will be followed. Therefore, an extra PI controller is needed to make sure the voltage is not over the lower limit when the high C-rate discharging pulses are applied. This PI controller should have faster responsiveness due to short and high-amplitude current pulses.

In order to do so, embedded MATLAB PID tuner is used. Since the maximum energy pulses are high-amplitude, in order to have better accuracy, the sampling rate is set as 0.1s. 0.1s will be the slowest response time for PI controller. For the simplicity, 0.1s is picked as the response time as shown in the Figure 4.16.

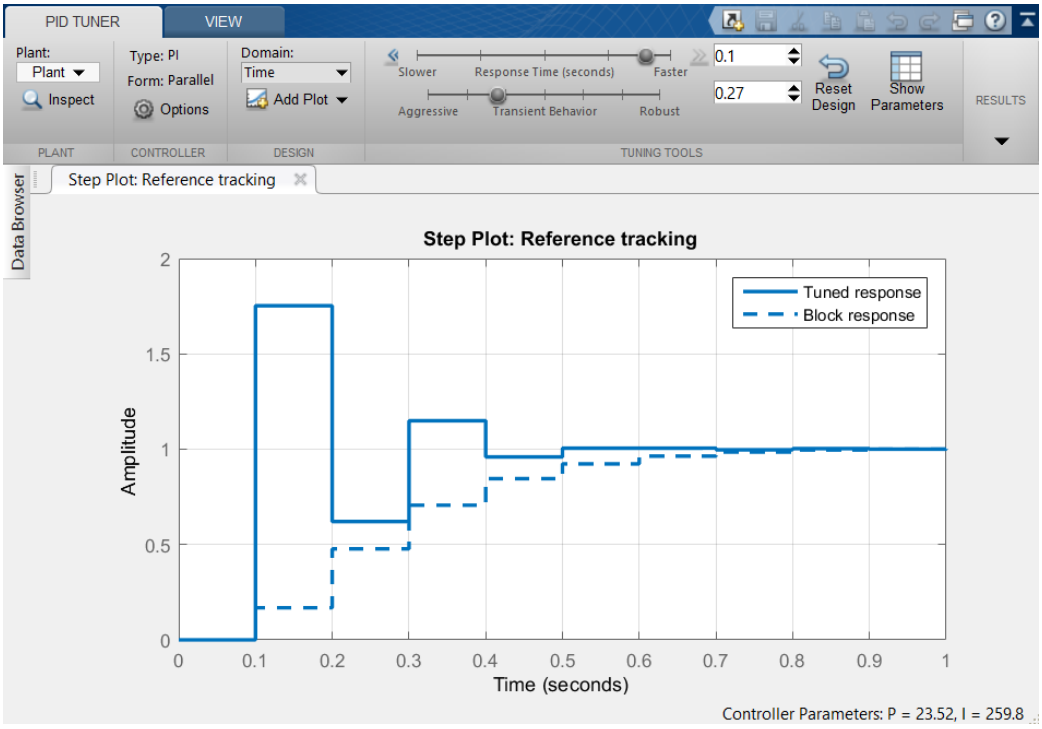

Figure 4.16 PID tuner presentation

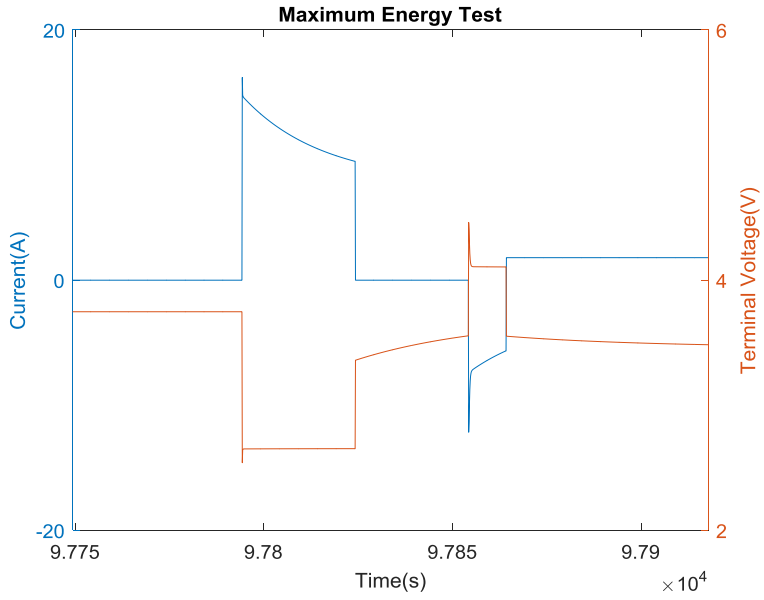

Figure 4.17 Performance of PI controller in simulation

The Figure 4.17 shows the performance of the tuned PI controller. It overshoots temporarily and converges significantly to the reference voltage. In this case, the current pulse is at 3 C-rate.

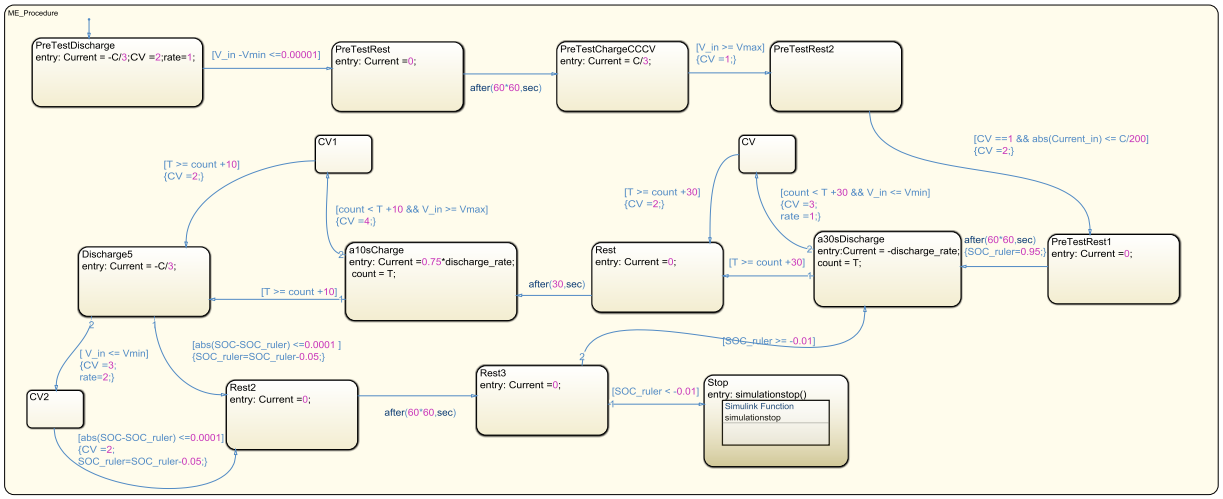

Figure 4.18 State flow of MEP tester

4.4 Time Domain Fitting Tool

As shown in Figure 4.11 and

Figure 4.12, there are normally at least 30 pulses at different SOC operation points, depending on the required level of accuracy. A few researchers tried to fit the resistances, capacitances and OCV-SOC curve pulse by pulse [32] [66]. As a result, a large amount of time could be consumed on fitting each pulse to obtain the battery parameters at a single SOC level. When the higher accuracy is needed, i.e. the interval between each SOC breakpoint is shorter, computational cost is raised. More importantly, the possibly high variability from pulse to pulse could lead to the difficulties to converge due to relatively inaccurate initials. A novel optimization based fitting tool is proposed, which is not dependent on the initials. It will not only speed up the whole fitting process but eliminate the possibility of diverging.

What can be extracted from the HPPC test normally is the capacity, OCV-SOC curve, resistances, capacitances, time constants (R×C). According to (4.1), total capacity is equal to the integration of current if the SOC varies from 0-100%. Therefore, complete voltage profile is clipped. Due to discretization of data acquisition, the integration of current is replaced by accumulation.

$$CAP = \sum_{k=1}^{n} i_k \Delta t_k \Big/ 3600 \tag{4.3}$$

where, Δt_k denotes $t_k - t_{k-1}$. It is assumed that the current maintains approximately constant during Δt. The rest of parameters will fit a comprehensive battery model. As Chapter 2 reviewed, the ECM presents a practical approach for modelling and its parameterization is described here.

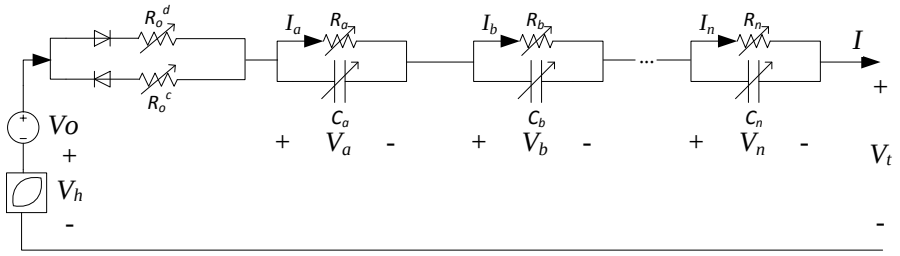

Figure 4.19 Equivalent circuit model of battery with n RC pairs

ECM with n asymmetric RC pairs is depicted in Figure 4.19. The asymmetric RC pairs are mimicking the different time constants under charging and discharging. Basically, the number of RC pairs relies on the accuracy requirements for the model. One to three RC pairs are normally selected [68]. The detailed modeling will be described in Chapter 6. It should be noted that the RC pairs are asymmetric, which is described in look-up-tables. The look-up-tables are functions of current direction, SOC and temperature.

This section describes the fitting algorithms developed and employed on the battery characterization data. According to the time domain modeling for battery,

$$V_k = V_{OC} - R_o I_k - R_a I_{a,k} - R_b I_{b,k} - \ldots - R_n I_{n,k} \tag{4.4}$$

By applying Kirchhoff's Current Law, the current I_n is derived as:

$$\frac{di_n(t)}{dt} = -\frac{1}{R_n C_n} i_n(t) + \frac{1}{R_n C_n} i(t) \tag{4.5}$$

A zero-order holder (ZOH) discretization approach was used to derive discretization expression as follows

$$I_{n,k} = e^{-\Delta t / \tau_n} I_{n,k-1} + (1 - e^{-\Delta t / \tau_n}) I_{k-1} \tag{4.6}$$

Quadratic programming is to find a vector $\boldsymbol{x}$ to minimize $\mathbf{x^T Q x + p^T x}$ subject to $\mathbf{Ax \le b}$. It can be found that quadratic programming can be applied when time-constant parameters are fixed. The cost function can be derived as follows:

$$\begin{aligned} &\min \mathbf{x^T Q x + p^T x} \\ &\min \textstyle\sum_{k=1}^{n} (V_k - \hat{V}_k)^2 = \min(\mathbf{Cx - v})^{\mathbf{T}} (\mathbf{Cx - v}) \\ &= \min(\mathbf{x^T (C^T C) x} - 2(\mathbf{v^T C})\mathbf{x} + \mathbf{v^T v}) \end{aligned} \tag{4.7}$$

where, $\mathbf{x} = [\mathbf{V_{oc}}^{\mathbf{T}}\ \mathbf{V_h}^{\mathbf{T}}\ \mathbf{R_o}^{\mathbf{T}}\ \mathbf{R_a}^{\mathbf{T}}\ \mathbf{R_b}^{\mathbf{T}} \ldots \mathbf{R_n}^{\mathbf{T}}\ \tilde{\mathbf{R}}_{\mathbf{o}}^{\mathbf{T}}\ \tilde{\mathbf{R}}_{\mathbf{a}}^{\mathbf{T}}\ \tilde{\mathbf{R}}_{\mathbf{b}}^{\mathbf{T}} \ldots \tilde{\mathbf{R}}_{\mathbf{n}}^{\mathbf{T}}]^{\mathbf{T}}$. $\mathbf{V_{oc}}$ denotes an open circuit voltage vector for full SOC range based on the SOC breakpoints of interests. $\mathbf{V_h}$ stands for hysteresis voltage. $\mathbf{R_n}$ and $\tilde{\mathbf{R}}_{\mathbf{n}}$ refer to n_{th} resistor and non-linear resistor on RC pair,

respectively. Vector **v** is measured voltage profile. **C** represents a regression matrix with **θ,** Mathematically, $\mathbf{C}=[\mathbf{c_1}^T\ \mathbf{c_2}^T\ \dots\ \mathbf{c_k}^T]^T$, k denotes the index of time interval.

4.4.1 Derivation of QP Fitting Tool for 1 RC Symmetric ECM

According to the analysis of battery modeling, a simple time-domain 1RC symmetric ECM example is shown below.

$$\begin{aligned}
V_{a,1} &= \theta V_{a,0} + R_a(1-\theta)I_0 \\
V_{a,2} &= \theta^2 V_{a,0} + R_a\theta(1-\theta)I_0 + R_a(1-\theta)I_1 \\
&\vdots \\
V_{a,k} &= \underbrace{\theta^k V_{a,0}}_{\substack{=0 \\ \text{assume zero} \\ \text{initial conditions}}} + R_a \underbrace{\sum_{j=0}^{k-1}\theta^{k-1-j}(1-\theta)I_j}_{\varphi_{a,k}} \\
I_{a,0} &= 0 \\
I_{a,k} &= \theta I_{a,k-1} + (1-\theta)I_{k-1} \\
\theta &= e^{-\frac{\Delta t}{\tau}} \\
V_{a,k} &= \theta V_{a,k-1} + R_a(1-\theta)I_{k-1}
\end{aligned} \tag{4.8}$$

where, τ is the time constant on the first RC pair (R×C). Since there is a long term rest (2 hours) before every pulse in HPPC test, the system is assumed stable (initial V_a is equal to zero).

$$\begin{aligned}
V_k &= V_{OC} - R_o I_k - R_a I_{a,k} \\
&= \begin{bmatrix} 1 & -I_k & -I_{a,k} \end{bmatrix} \begin{bmatrix} V_{oc} \\ R_o \\ R_a \end{bmatrix} = \mathbf{c}_k^T \mathbf{x}
\end{aligned} \tag{4.9}$$

$$\min \sum_{k=1}^{n} (V_k - \hat{V}_k)^2 = \min \left(\begin{bmatrix} V_{Data1} \\ \vdots \\ V_{Data} \end{bmatrix} - \mathbf{Cx} \right)^T \left(\begin{bmatrix} V_{Data1} \\ \vdots \\ V_{Data} \end{bmatrix} - \mathbf{Cx} \right) \tag{4.10}$$

$$\hat{V}_k = \left[\begin{bmatrix}1 & -I_k & -I_{a,k}\end{bmatrix} \otimes \mathbf{z}_k^T\right] \begin{bmatrix} V_{OCV}^{SOC=0\%} \\ \vdots \\ V_{OCV}^{SOC=100\%} \\ R_o^{SOC=0\%} \\ \vdots \\ R_o^{SOC=100\%} \\ R_a^{SOC=0\%} \\ \vdots \\ R_a^{SOC=100\%} \end{bmatrix} = \mathbf{c}_k^T \mathbf{x} \tag{4.11}$$

where, $\mathbf{z}_k^T = \begin{bmatrix}0 & \cdots & 0 & \lambda & 1-\lambda & 0 & \cdots & 0\end{bmatrix}$ which is a masking vector that selects the appropriate parameters to fit for the given data point. Kronecker Vector product is used to determine which R at SOC = x% is fitting.

$$\begin{bmatrix}a & b & c\end{bmatrix} \otimes \begin{bmatrix}X & Y\end{bmatrix} = \begin{bmatrix}aX & aY & bX & bY & cX & cY\end{bmatrix} \tag{4.12}$$

Subtleties to note are that 1) the RC states are reset between data time intervals and 2) SOC as a function of time interval number is precalculated and assumed constant during an interval. The value of λ is determined by the closest two SOC interval points. In order for the parameterization methods to correctly work, the entire SOC range needs to be excited by the data.

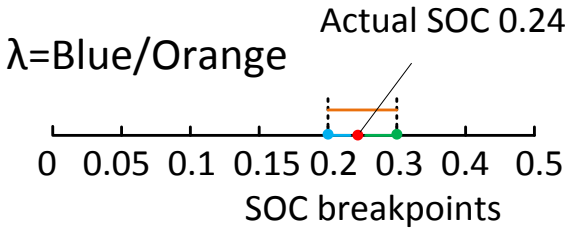

Figure 4.20 Diagram of how to calculate λ

An example is described below for explaining how the λ is calculated. Assuming the predefined fitting OCV breakpoints are at [0 0.05 0.1 0.15 0.2 0.3 0.4 0.5 0.6 0.7 0.8 0.85 0.9 0.95 1] SOC breakpoints. However, the actual SOC at i_{th} time interval is most likely not equal to the one of the elements in the OCV breakpoints vector, e.g. consider SOC=0.24. So it can attribute to the two closest SOC breakpoints calculated proportionally (0.2 and 0.3). The effect of 0.2 SOC on the OCV can be quantified as $(0.24-0.2)/(0.3-0.2)=0.4$. Similarly, the breakpoint 0.3 will have 60% influence on the OCV at 0.24 SOC as depicted in Figure 4.20. It is also applicable for resistance fitting. Therefore, λ can be derived as follows

$$z_k(i)=\lambda=\begin{cases}1, & SOC^{OCV/R}(i)=SOC_k \\ (SOC_k-SOC^{OCV/R}(i_1))\Big/(SOC^{OCV/R}(i_2)-SOC^{OCV/R}(i_1)), & any\ SOC^{OCV/R}\neq SOC_k\end{cases} \quad (4.13)$$

where, SOC_k represents the actual SOC pre-calculated by coulomb counting at time interval *k*. $SOC^{OCV/R}(i)$ denotes the *i* th SOC breakpoint for OCV-SOC profile and R-SOC profiles. i_1 refers to the closest index of SOC breakpoint on the left side of SOCk, shown in Figure 4.20 as blue point. i_2 is the closest index of SOC breakpoint on the right side of SOC_k, shown in Figure 4.20 as green point.

As a result, the method can be applied for a general profile spanning a large SOC range. More importantly, it can be employed on arbitrary profiles such as application usage cycle profiles. i.e. An online parameter optimization is finalized without extra observers, such as RLS and KF.

4.4.2 Other Features

Asymmetric RC Model

It has been observed by some researchers that the impedance of battery depends on whether the battery is charging or discharging [40] [69]. Therefore, the impedance should be not only a function of SOC and temperature but also a function of current direction. Including asymmetric impedance can improve the accuracy of the battery model.

For asymmetric RC model, the following evolution discrete-time dynamics result is derived.

$$
\begin{aligned}
&V_{a,1} = R_a^c(1-\theta^c)I_0^- + R_a^d(1-\theta^d)I_0^+ \\
&V_{a,2} = \theta_1^{\,2}(R_a^c(1-\theta^c)I_0^- + R_a^d(1-\theta^d)I_0^+) + R_a^c(1-\theta^c)I_1^- + R_a^d(1-\theta^d)I_1^+ \\
&\quad\vdots \\
&V_{a,k} = \underbrace{R_a^c\sum_{j=0}^{k-1}\left(\prod_{i=j}^{k-1}\theta_i\right)(1-\theta^c)I_j^-}_{I_{a,k}^c} + \underbrace{R_a^d\sum_{j=0}^{k-1}\left(\prod_{i=j}^{k-1}\theta_i\right)(1-\theta^d)I_j^+}_{I_{a,k}^d} \\
&I_{a,0}^c = 0,\ I_{a,0}^d = 0 \\
&I_{a,k}^c = \theta_{k-1}I_{a,k-1}^c + (1-\theta^c)I_{k-1}^-,\ I_{a,k}^c = \theta_{k-1}I_{a,k-1}^d + (1-\theta^d)I_{k-1}^+ \\
&\theta_k = \begin{cases} 1 & k=0 \\ \theta^c & k>0\ \&\ I_{k-1}<0 \\ \theta^d & k>0\ \&\ I_{k-1}>0 \\ \theta_{k-1} & k>0\ \&\ I_{k-1}=0 \end{cases}
\end{aligned}
\tag{4.14}
$$

$$
\hat{V}_k = \left[\begin{bmatrix} 1 & -I_k^+ & -I_k^- & -I_{a,k}^+ & -I_{a,k}^- \end{bmatrix} \otimes \mathbf{z}_k^T\right] \begin{bmatrix} \mathbf{V}_{OCV}^{SOC} \\ \mathbf{R}_{o,c}^{SOC} \\ \mathbf{R}_{o,d}^{SOC} \\ \mathbf{R}_{a,c}^{SOC} \\ \mathbf{R}_{a,d}^{SOC} \end{bmatrix} = \mathbf{c}_k^T\mathbf{x} \tag{4.15}
$$

where,

$$
\begin{aligned}
&\mathbf{V}_{OCV}^{SOC} = [V_{OCV}^{SOC=0\%} \quad \dots \quad V_{OCV}^{SOC=100\%}]^T,\quad \mathbf{R}_{o,c}^{SOC} = [R_{o,c}^{SOC=0\%} \quad \dots \quad R_{o,c}^{SOC=100\%}]^T \\
&\mathbf{R}_{o,d}^{SOC} = [R_{o,d}^{SOC=0\%} \quad \dots \quad R_{o,d}^{SOC=100\%}]^T,\quad \mathbf{R}_{a,c}^{SOC} = [R_{a,c}^{SOC=0\%} \quad \dots \quad R_{a,c}^{SOC=100\%}]^T \\
&\mathbf{R}_{a,d}^{SOC} = [R_{a,d}^{SOC=0\%} \quad \dots \quad R_{a,d}^{SOC=100\%}]^T
\end{aligned}
\tag{4.16}
$$

The subscript or superscript *c* and *d* indicate charging and discharging, respectively.

Hysteresis Voltage

Similar with asymmetric impedance, hysteresis voltage is a factor that can improve the fidelity of the battery model. At the same SOC level, many studies have shown different OCV values when the battery is charging and discharging [22] [70] [71] [72]. Normally, charging OCV is greater than discharging OCV at each SOC breakpoint, as it can be seen from Figure 4.21. The 'major loop' is the path that will be followed when the battery is fully charged (0% - 100%) or discharged (100% - 0%). The 'minor loop' will be followed when the battery is partially charged or discharged. For instance, when the battery is charged from start point C, the OCV curve will go along from C to D instead of major loop.

The hysteresis behavior is minimal in Lithium-Ion batteries; instead it is a major concern when it comes to Ni-MH batteries [70]. In order to build a general fitting tool, hysteresis effect is included, the expression of zero-state hysteresis is derived below

$$V_{h,k} = -s_k M(SOC_k), \quad s_k = \begin{cases} 1, & i_k > \varepsilon \\ -1, & i_k < -\varepsilon \\ s_{k-1}, & |i_k| \le \varepsilon \end{cases} \tag{4.17}$$

where, s_k indicates the sign of the current with history stored. ε is a small and positive value to recognize whether the battery is in rest period. $M(SOC_k)$ is the average value of discharge/charge curve of 'major loop'.

The one-state hysteresis model is summarized as follows

$$\begin{aligned} V_h &= V_h^{\max} \cdot v_h \\ \frac{dv_h}{dt} &= -\gamma I(\text{sgn}(I)v_h + 1) \\ v_{h_k} &= -\text{sgn}(I_{k-1}) + (v_{h_k} + \text{sgn}(I_{k-1}))e^{-\gamma|I_{k-1}|\Delta t} \end{aligned} \tag{4.18}$$

where, V_h is the hysteresis voltage. γ is a time constant which offers time decay. $V_h^{\max}$ is the maximum hysteresis voltage which happens on 'major loop' at each SOC breakpoint. The readers are referred to [8] and [40] for more details of one-state hysteresis modeling.

For better accuracy, one-state hysteresis model is used. In simulation, v_h should be pre-calculated and added to C matrix to identify $V_h^{\max}(SOC)$. A small change should be made to (4.9) to apply hysteresis voltage fitting, as derived in (4.19).

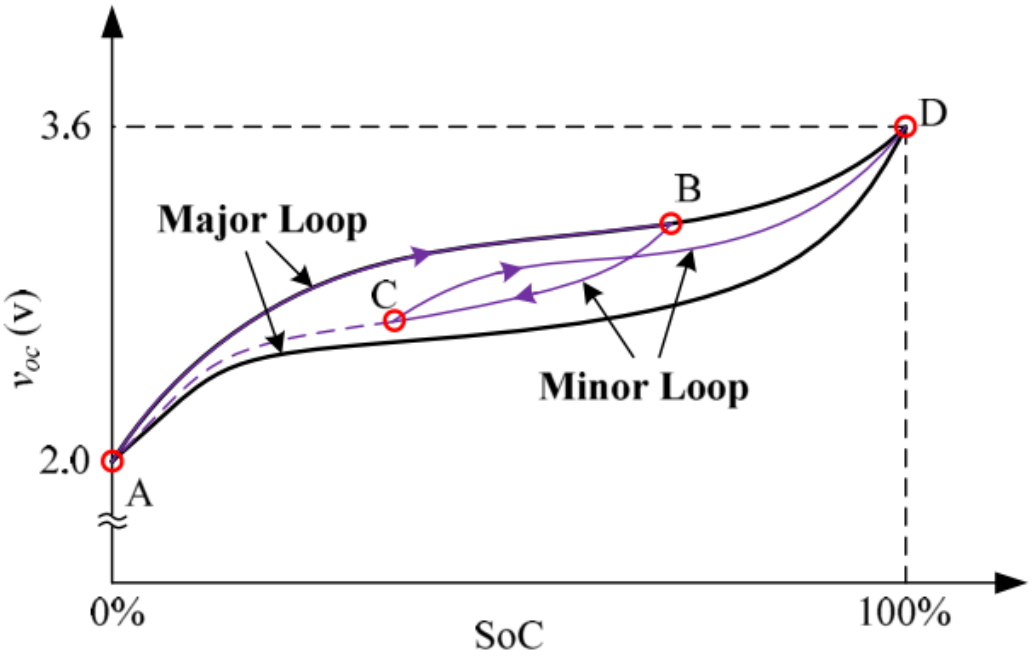

Figure 4.21 Conceptual influence of the battery hysteresis effect on OCV-SOC curve (adopted from [73])

$$\begin{aligned} V_k &= V_{OCV} + V_h - R_o I_k - R_a I_{a,k} \\ &= \begin{bmatrix} 1 & v_h & -I_k & -I_{a,k} 1 \end{bmatrix} \begin{bmatrix} V_{OCV} \\ V_h^{\max} \\ R_o \\ R_a \end{bmatrix} = \mathbf{c}_k^T \mathbf{x} \end{aligned} \tag{4.19}$$

Current-Dependent Resistance

According to the Butler-Volmer equation [74], charge transfer resistance is actually not ideally a linear function of current and voltage. For small current density charge or discharge *j*, which is an indicator of current in electrochemical area, overpotential is linearly generated as follows:

$$\eta = R_{ct} j \tag{4.20}$$

However, for large $|j|$, the overpotential is proportional to the log of the current, where the slope known as the Tafel slope [74] will be captured by the time-domain fitting tool. Figure 4.22 shows the general idea about the current-dependent resistance. When $|\eta|$ or $|j / i_0|$ is higher than linear area (0-50 mV or few amperes), nonlinearity is gradually appearing, where the Butler-Volmer equation converges to Tafel approximations (dotted). The readers should be referred to [74] for more details.

In this study, the charge transfer resistance R_{ct} is proposed to be modelled as

$$V_{ct,k} = R_{ct} I_{ct,k} + R_{ct.k}^{slope}(SOC) \cdot \log(1 + |I_{ct,k}|) \tag{4.21}$$

where, $R_{ct,k}^{slope}$ represents the Tafel slope of the charge transfer resistance. The slope is also a parameter that is going to be fitted. This equation can reflect this nonlinear behavior accurately, as shown in Figure 4.22.

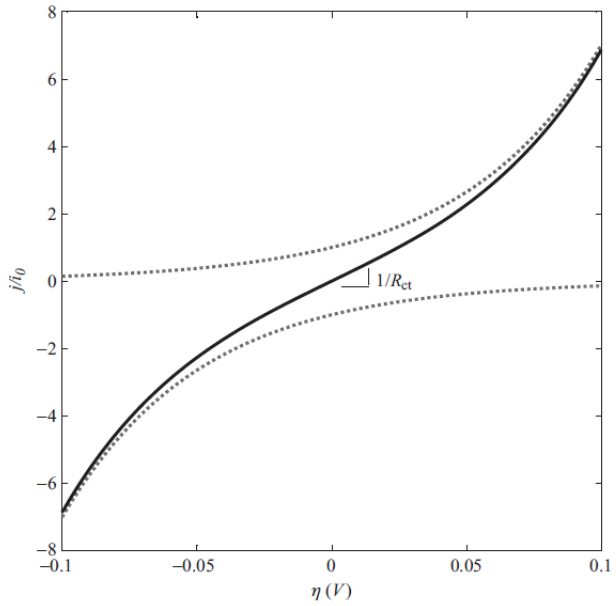

(a)

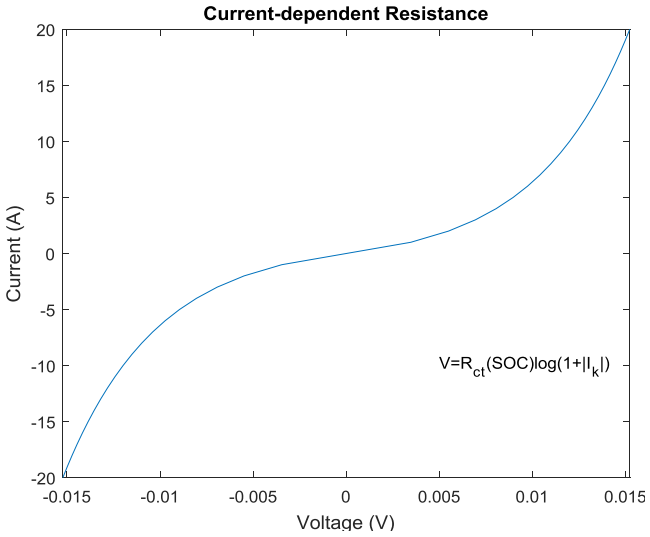

(b)

Figure 4.22 Comparison between (a) Tafel approximations (dotted) and Butler-Volmer equation (Solid) (adopted from [74]), (b) Approximated Current-dependent resistance from (4.21).

An extra modification can be made to (4.9) to apply current-dependent resistance fitting, as derived in (4.22).

$$V_k = V_{OCV,k} + V_{h,k} - R_o I_k - R_a I_{a,k} - R_a^{slope} \cdot \log(1+|I|)$$
$$= \begin{bmatrix} 1 & v_h & I_k & I_{a,k} & \log(1+|I|) \end{bmatrix} \begin{bmatrix} V_{OCV} \\ V_h^{\max} \\ R_o \\ R_a \\ R_a^{slope} \end{bmatrix} = \mathbf{c}_k^T \mathbf{x} \quad (4.22)$$

Two-Stage Optimization Algorithm

In some cases the local minimum would yield an unrealistic result with exceptionally large resistances and time-constants. A two stage optimization algorithm is employed where an inner-loop optimization assumes that the τ=RC time-constants are held constant. Using such a simplification, the inner-stage fitting can be formulated as a QP, i.e. as the formulation in (4.11) and (4.15). The outer-loop optimization searches a reduced dimensional space to find optimal values of the time constant parameters.

This approach is applicable to both time-domain and frequency domain data and characterization. It greatly speeds up the fitting routine since efficient globally optimal QP solvers can be readily employed, for example Matlab quadprog. The flowchart is shown in Figure 4.23.

Constrains $\mathbf{Ax} \le \mathbf{b}$ can be chosen to assign known values, e.g. open circuit voltage based on SOC operating point, parameter smoothness, non-negativity and bounded value constraints. The QP finds optimal values for a given time-constant value.

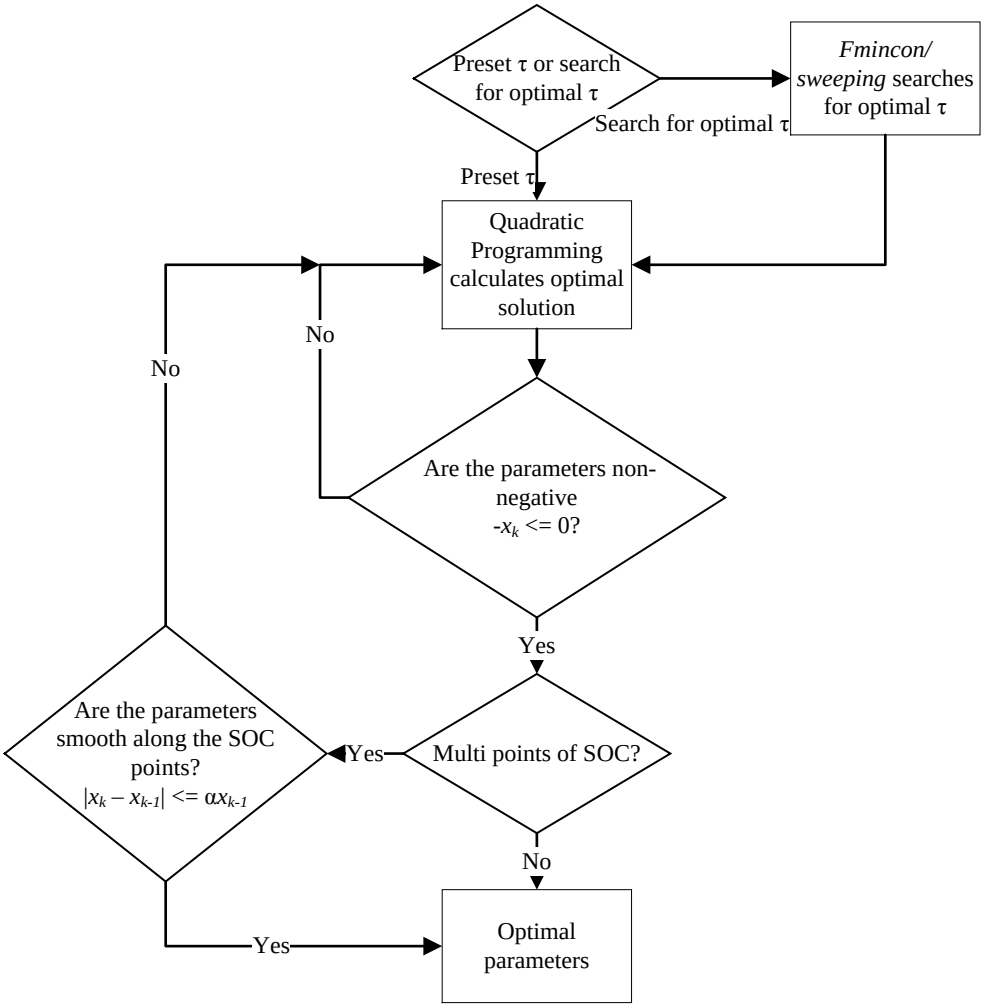

Figure 4.23 Global parameterization fitting method with smoothness control and nonnegetivity constraint.

A known battery model with 1-RC pair (31 s time constant) and 2-RC pair (31 s and 81 s time constants) is used to verify the two-stage algorithm's ability to find the optimal time constants. The simulated HPPC generator is employed to excite the battery model to obtain the HPPC profile. Figure 4.24 shows a voltage response from the known 1-RC battery model to a short-term current pulse. The optimization algorithm shown in Figure 4.23 is applied to obtain the optimal time constant. It can be observed from Figure 4.24 that the accurate 31 s time constant is captured by the algorithm. The same result can be obtained based on 2-RC battery model. The

exact 31 s and 81 s time constants are found, as shown in Figure 4.25. As a result, the optimization algorith is able to find the global minimum .

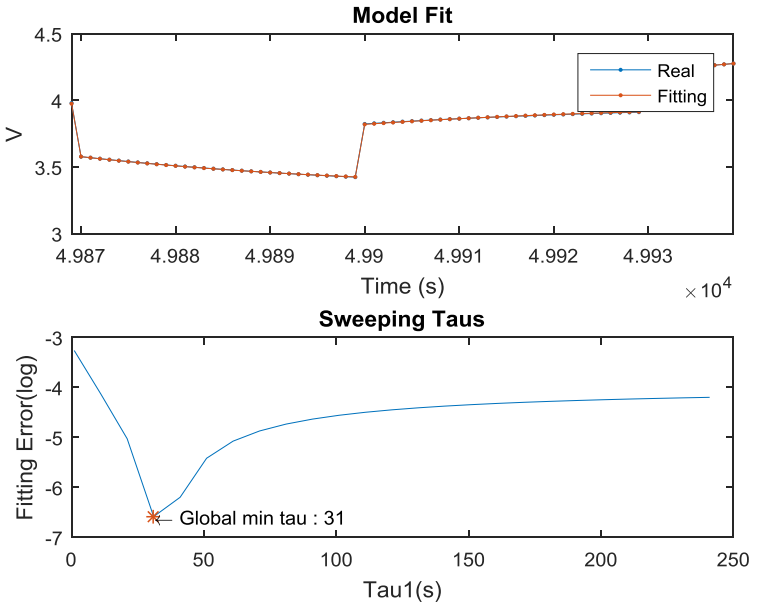

Figure 4.24 1-RC battery model and time constant optimization

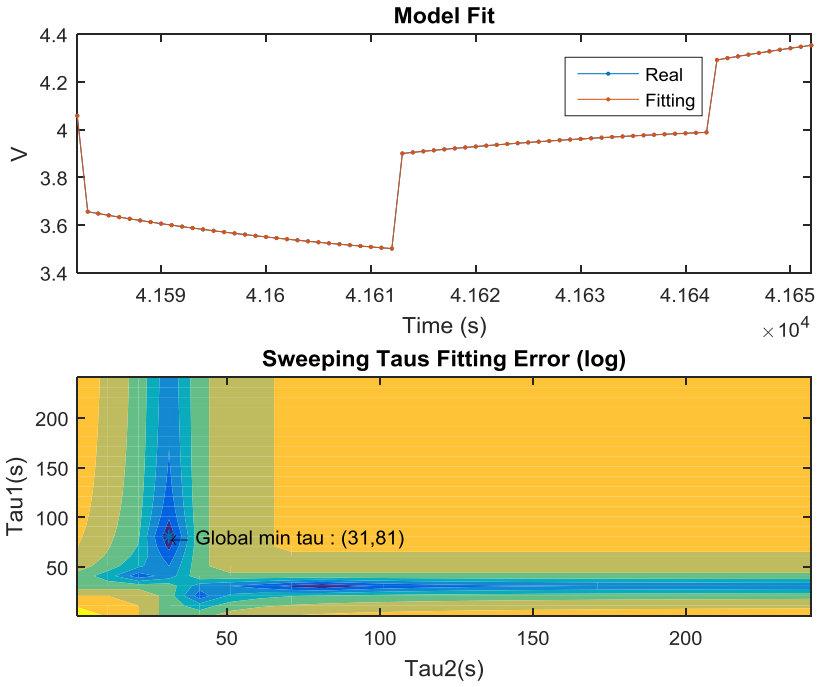

Figure 4.25 2-RC battery model and time constant optimization

4.5 Fitting Results

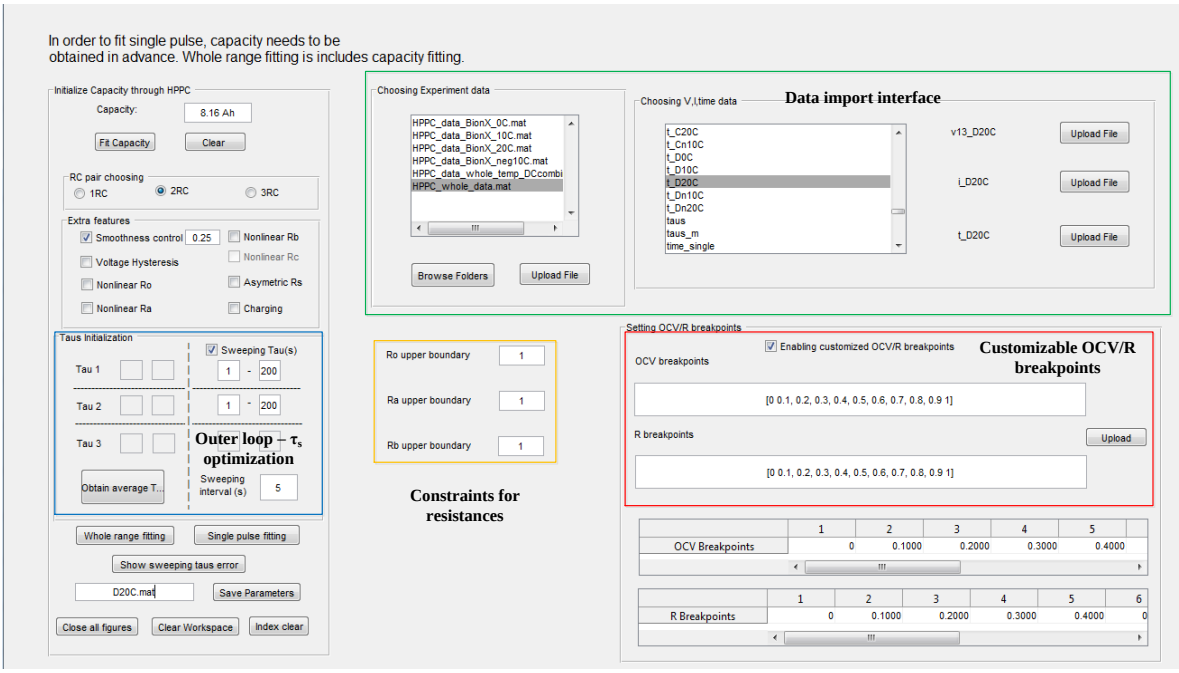

Figure 4.26 Graphic user interface for time domain parameterization

A graphic user interface (GUI) powered by MATLAB is developed to systematically integrate all the functionalities, as shown in Figure 4.26. It features outer-loop optimization for time constants selection, the switches of smoothness control and current-dependent resistance, and customizable OCV/R breakpoint vectors, etc. This GUI was applied to the rest of study.

Table 4.3: Fitted results comparison between QP-based fitting and fmincon

HPPC Test	**Ro**	**Ra**	**Rb**	**Ca**	**Cb**	**Time**
QP based fitting error	0.7%	0.85%	0.2%	0.86%	0.2%	0.166s
Fimincon based fitting error	0.7%	1.3%	0.2%	0.84%	0.13%	25.5s

A comparison study on QP and Fmincon is performed based on HPPC data generated by simulated tester developed in Section 4.5, to emphasize the advantages of the proposed fitting algorithm, as shown in Table 4.3. From the table the proposed QP-based fitting can give the

same accuracy level but within 1/200 of the computation time compared to fmincon only optimizer

In addition, different levels of measurement noise are added to assess the sensitivity of the parameter fitting approaches. Sample results of the fitting algorithm performance and sensitivity using synthetic data are shown in Figure 4.27.

Figure 4.27 highlights the parameter estimates are insensitive to the addition of typical measurement noise; the level of measurement noise is chosen to match the specifications of the battery testing equipment.

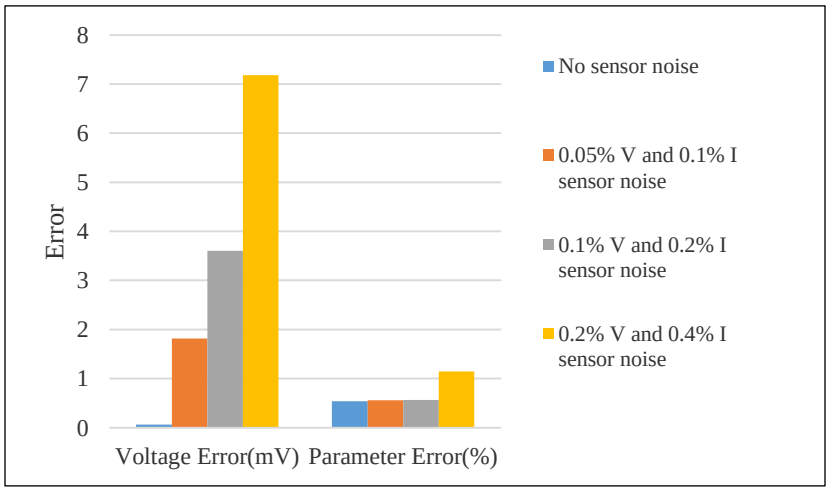

Figure 4.27 Effect of sensor noises on QP based fitting tool

The experimental HPPC test is performed between upper limit and lower limit of terminal voltage at every 5% SOC intervals. The test was performed at -10, 0 and 20 °C. In order to balance the accuracy and complexity of the battery model, 2-RC battery model is selected for parameter fitting and future modeling validation.

The proposed QP fitting algorithm is used to process the experimental results. The fitting results based on single pulse fitting (SPF) are shown in Table 4.4. Regarding SPF, the time constants are optimized at each SOC breakpoint. On the other hand, full range fitting (FRF) is performed to

compare with SPF in terms of accuracy and complexity. It is noted that the time constants in full SOC range fitting are fixed as the average value of the results from SPF. As a result, it reduces the time of searching for optimal time constants. The both results are compared in Table 4.4. The difference of measured terminal voltage and fitted terminal voltage is analyzed. The mean error at three temperatures is less than 3 mV for SPF and 8 mV for FRF, which shows the ability to accurately fit the battery dynamic response. The detailed fitting results and parameters are shown in Figure 4.28 - Figure 4.30.

Table 4.4: Results of HPPC fitting algorithm

	Temperature (°C)	**-10**	**0**	**20**
Single Pulse Fitting	**Mean Error (mV)**	2.952	2.403	2.053
	RMS Error (mV)	4.20	3.40	2.58
	Max Error (mV)	49.10	41.76	11.85
Full Range Fitting	**Mean Error (mV)**	7.69	6.81	5.12
	RMS Error (mV)	11.13	11.83	5.12
	Max Error (mV)	266.97	197.55	60.403

The reasons why SPF outweighs FRF are described as follows: a) the time constants are optimized at every single pulse for SPF. Due to variability of parameters, inaccurate time constants would lead to biased voltage, b) SPF is only applied to the period of time when current pulses are inserted. i.e. SPF is not able to fit relaxation time. This is highlighted in Figure 4.29 (a) and Figure 4.30 (a). It is because the impedance is highly dependent on SOC, so during two consequent charging and discharging pulses SOC is assumed not varying much. Based on this

assumption, SPF is able to be applied. However, FRF has the ability to track the SOC-dependent impedance, as described in (4.15). Some errors for FRF are caused by fitting relaxation time that is not covered by SPF so this phenomenon could be observed in Figure 4.28 (a) - Figure 4.30 (a) as the blue line is straight, c) overcharging in the experiments leads to distortion of voltage profile at low voltage, highlighted in Figure 4.29 (a) and Figure 4.30 (a).

Additional smooth control comparison was performed and one example is shown in Figure 4.31. One is chosen as 1, another one is selected as 0.05. When the smooth factor is smaller, the parameter fitting curve is smoother. Even though it might cause losing fidelity on fitted parameters at some SOC points, as shown in Figure 4.31 (b). The voltage fitting results for both smooth factors have similar accuracy. It can be concluded that smooth control would help the fitting algorithm filter some odd points out of impedance curve, since the relationship between impedance and SOC follows exponential distributions.

4.6 Conclusion

In this chapter, a capacity test to BionX battery pack was performed at five temperatures. The corresponding capacities were used for HPPC test and battery modeling as reference. The theory of HPPC and MEP tests were explained. Simulated HPPC and MEP testers are proposed to enable the sensitivity study on fitting tools and help design battery's architecture. A graphic user interface is developed based on proposed algorithm. A comparison between fmincon and QP based fitting algorithms reveals QP is more accurate and faster. Additional sensitivity study on QP shows the insensitivity and robustness to measurement noises. The experimental fitting results concludes that SPF offers high accuracy but longer processing time to find the optimal time constants. On the other hand, FRF balances the accuracy and computational complexity.

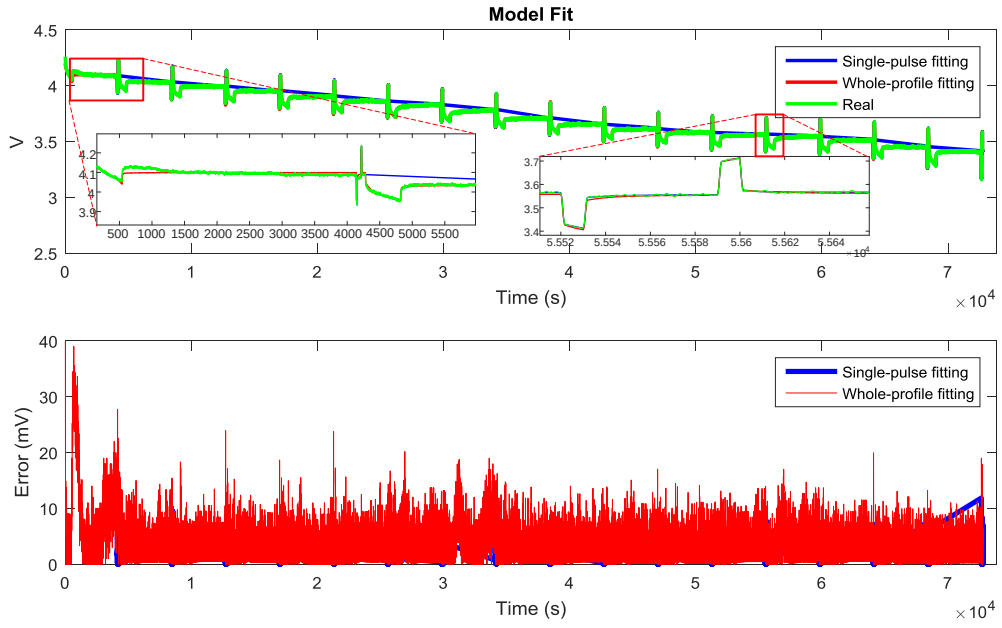

(a)

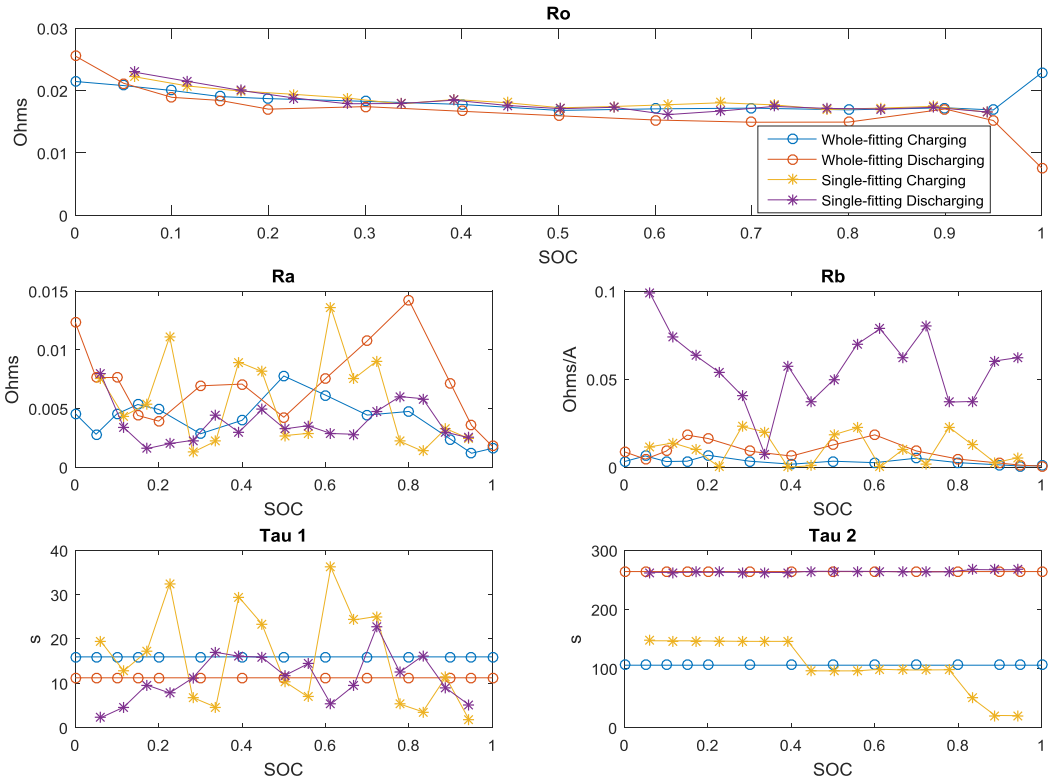

(b)

Figure 4.28 Comparison between single pulse and whole range fitting at 20 ºC

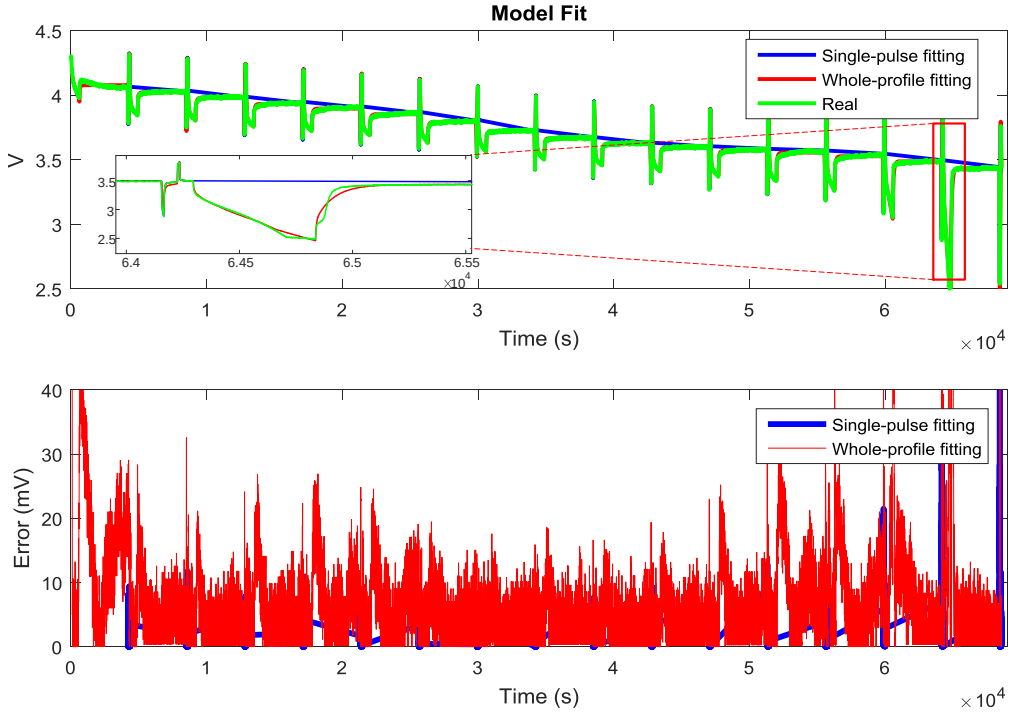

(a)

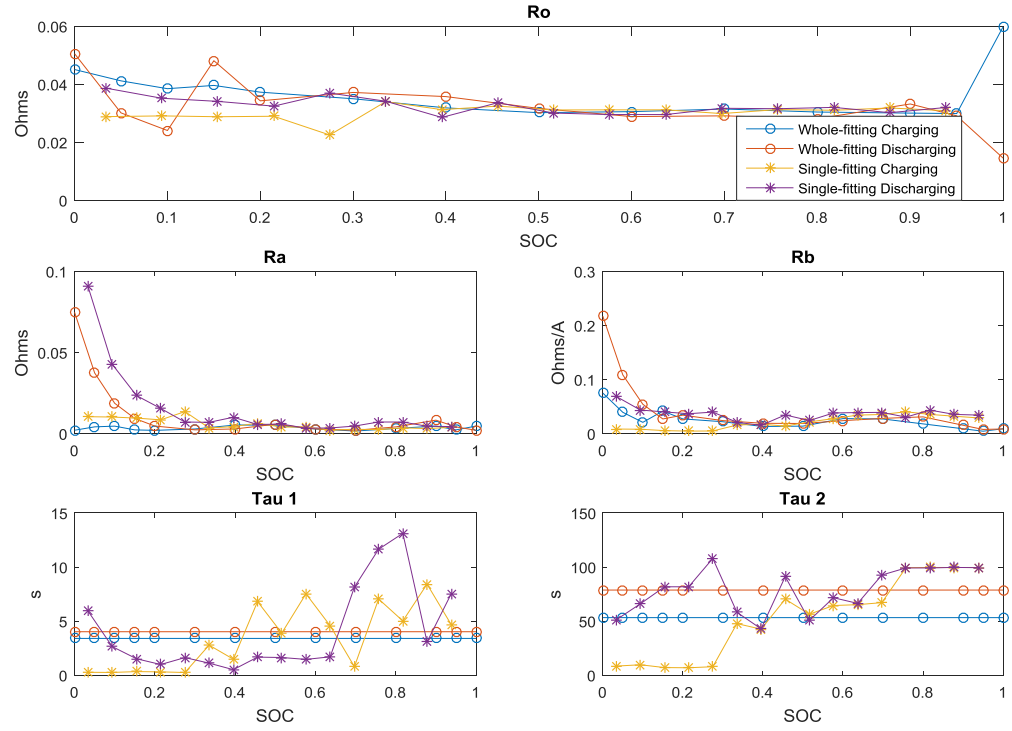

(b)

Figure 4.29 Comparison between single pulse and whole range fitting at 0 ºC

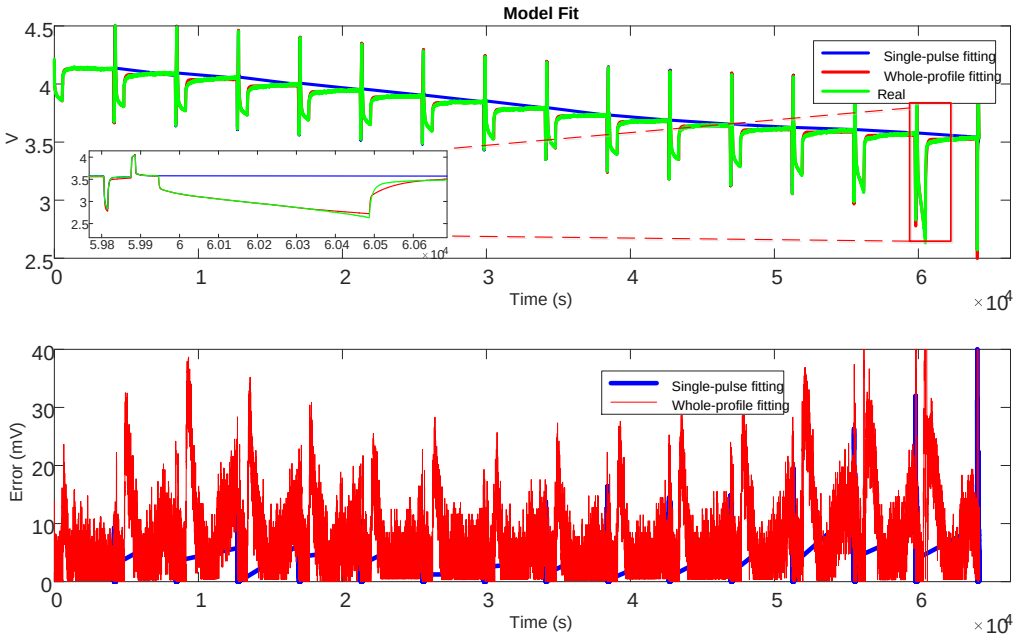

(a)

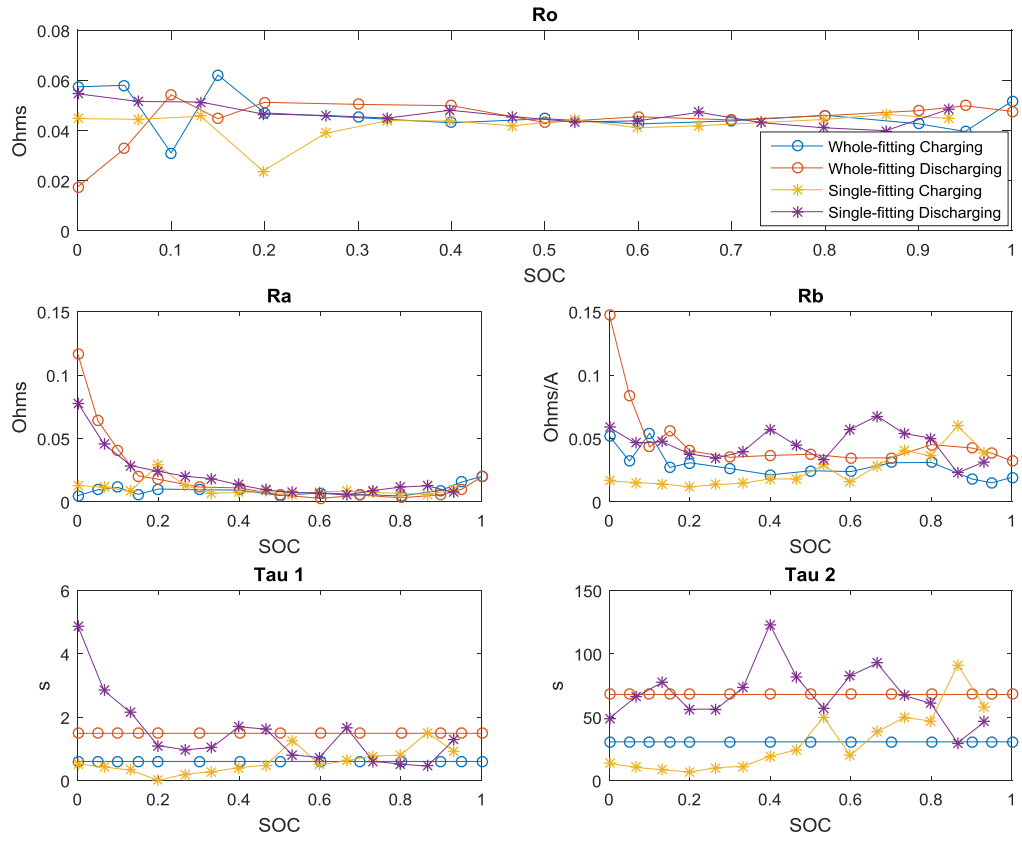

(b)

Figure 4.30 Comparison between single-pulse and whole-profile fitting results at -10 ºC

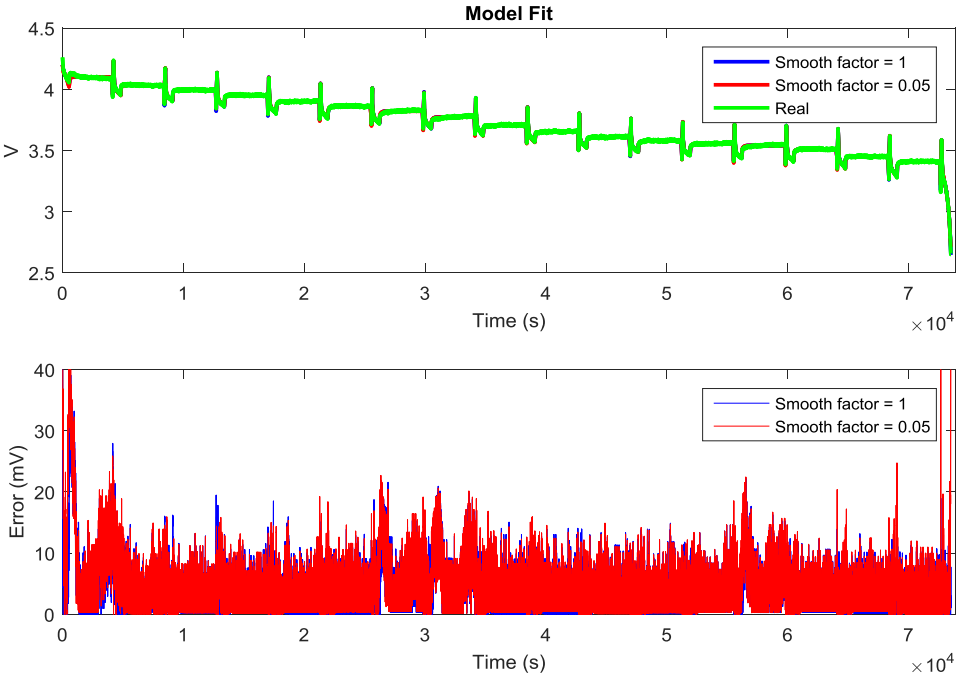

(a)

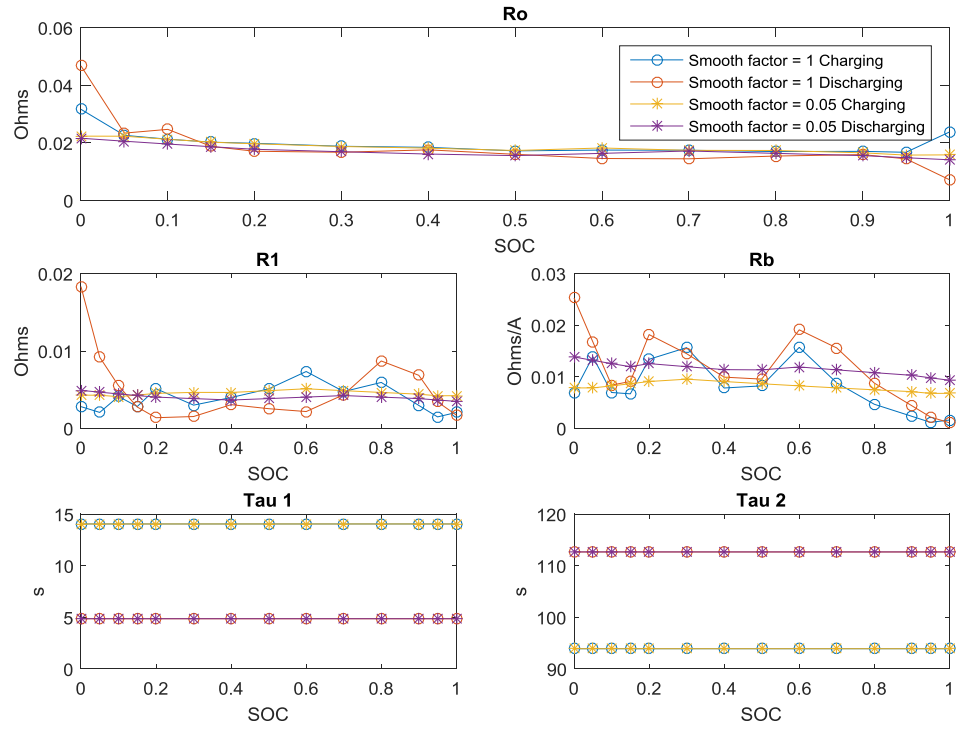

(b)

Figure 4.31 Comparison between smooth factor =1 and smooth factor = 0.05 fitting results at 20 ºC

Chapter 5

FREQUENCY DOMAIN EXPERIMENTS AND CHARACTERIZATION

5.1 Introduction

EIS test is a non-destructive identification test procedure. Due to the fact that the battery cannot be treated as a pure resistance, the voltage response from current would be lagged for a certain phase angle. The impedance can be calculated as

$$Z = \frac{\Delta V}{\Delta I} = \frac{V_{\max}}{I_{\max}} e^{j\phi} \tag{5.1}$$

One of the advantages of the EIS is that it can reflect the electrochemical structure of the battery directly. However, a systematic analysis about frequency domain algorithm is needed. Even though HPPC and EIS both can be interpreted to a certain battery model, the difference or similarity between them has not been compared.

Therefore, in this chapter, the contributions are described as follows: 1) a novel QP based fitting algorithm is proposed and verified via simulation and experiments, 2) based on the QP, the algorithm is extended to fit the EIS curves at multiple SOC points to dramatically increase the speed, 3) a comparison between time domain and frequency domain fitted parameters is performed.

The rest of chapter is divided into three sections. The interpretation of EIS from battery model point of view is explained in Section 5.2. The QP based algorithm for single and multiple SOC points is theoretically described in Section 3. Section 4 includes the simulation and experimental validation of the fitting tool. A subset of the work in this chapter is part of publication [60].

5.2 Interpreted Electrical Elements from EIS

A so called Nyquist diagram can be plotted by using real part of impedance as x-axis and imaginary part as y-axis (typically inverted). Figure 5.1 shows the typical shape of an EIS test at some operating points; note the frequency information is not fully depicted in this plot. Extra plots, such as Bode, will be needed for frequency analysis. The specific patterns can be interpreted as electrical elements. The EIS curve normally consists of four parts, as shown in Figure 5.1.

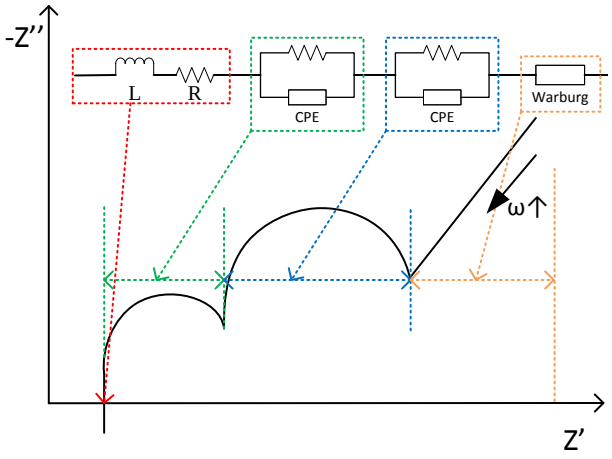

Figure 5.1 Frequency domain equivalent circuit model

5.2.1 Ohmic Resistance and Inductance

The internal resistance always exists in batteries, this is caused by several factors. For example, the conductivity of the anodes and cathodes and the electrolyte [75]. Due to the thermal-sensitivity of these chemical components, the Ohmic resistance is typically highly dependent on

temperature. Besides, it has been found the SOC, charging/discharging history and aging dramatically affect the changes of this resistance [76].

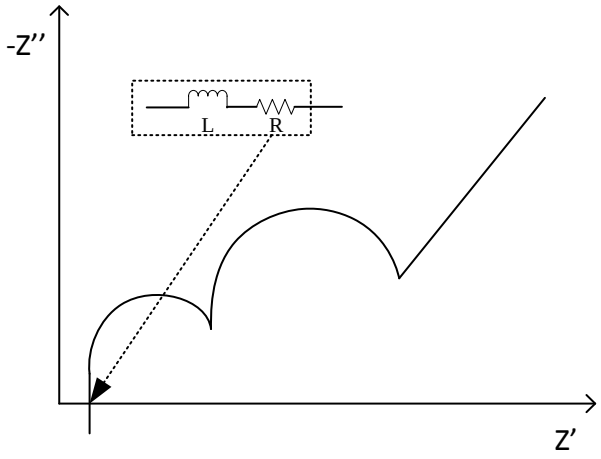

Figure 5.2 Interpretation of Ohmic resistance in EIS

In time domain, the Ohmic resistance is expressed as an instantaneous voltage drop when a current pulse is applied. Similarly, in complex plane, the Ohmic resistance appears at phase = 0 (Im|Z| = 0), i.e. it corresponds to the intersection of the EIS curve and the x-axis.

It has been observed that the imaginary part continuously increases at high frequencies while real part maintains constant (value of Ohmic resistance) [75]. This inductive behavior is essentially the self-inductance of the conductive loop formed by the terminals, connectors and electrodes of the battery cell [77]. It can be modeled by a lumped constant inductance *L*.

5.2.2 ZARC Elements

The well-known semi-circles in EIS plots, presented in Figure 5.3, are caused by a so-called ZARC element. ZARC elements consist of a parallel pair of a charge transfer resistor and a CPE. CPEs applied in electrochemical area were proposed by Cole and Cole [78], the dielectric

response can be decomposed into the ZARC elements. It is one of the most widely used distributions to describe the appearance of depressed semi-circle in EIS curves [51].

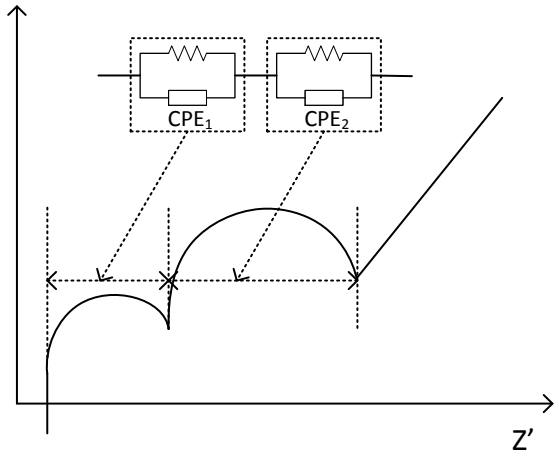

Figure 5.3 Interpretation of ZARC in EIS

A pure capacitor is a specialized CPE with depression factor α equal to 1, according to the definition (5.2).

$$Z_{CPE} = \frac{1}{C(j\omega)^{\alpha}} \tag{5.2}$$

where C indicates a generalized capacity. The depression factor α with a range between 0-1 reflects the depression of the semi-circle in EIS curve depicted in Figure 5.1. The ZARC elements can be described as follows:

$$Z_{ZARC} = \frac{1}{1/R + C(j\omega)^{\alpha}} \tag{5.3}$$

There are two extremes to help understand the responsibility of CPE in ZARC element. 1) When α = 0, ZARC can be replaced by a pure resistor. 2) For α = 1, ZARC represents an ideal RC pair

with a time constant $\tau = RC$. The effect of different values of α is summarized in Figure 5.4. It can be observed that the curve is flatter with α smaller.

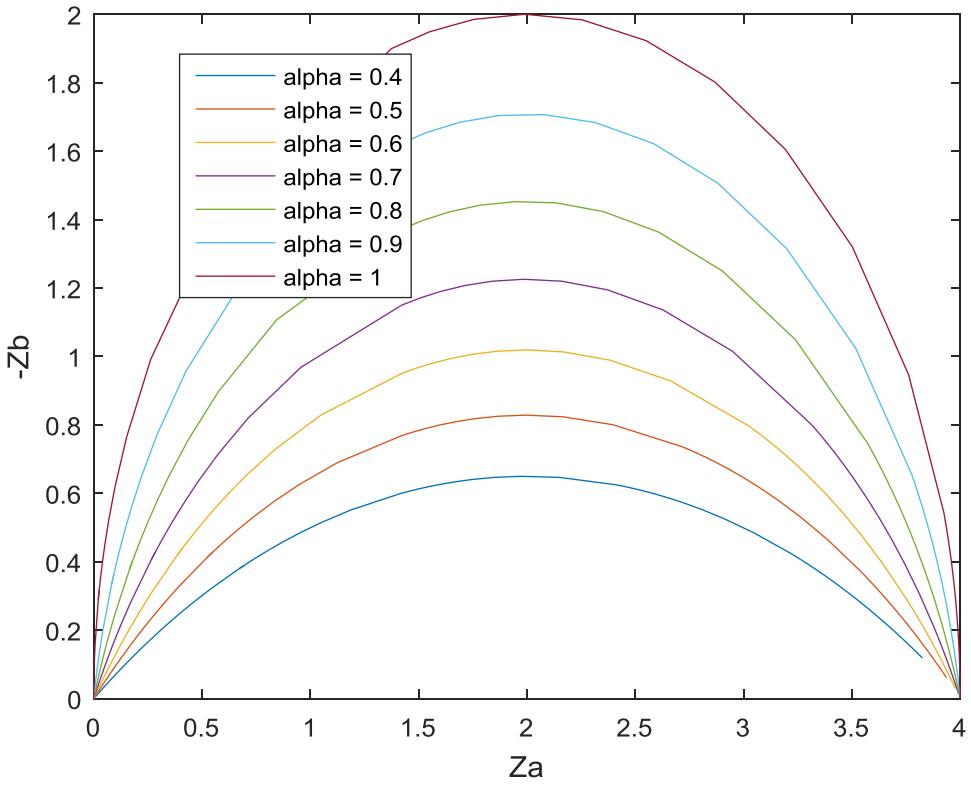

Figure 5.4 The effect of different values of α on the semi-curve

ZARC is beneficial to model the depression behavior, which is the characteristic for Lithium-ion cells [79]. The CPE relates better to the double layer capacitance of the cell porous electrodes than a pure capacitor circuit element, because the depression of semi-circles in impedance spectra are the characteristic for lithium-ion cells [79]. However, due to lack of Laplace transformation, ZARC elements is not able to be transferred in time domain without approximations [51].

5.2.3 Warburg Impedance

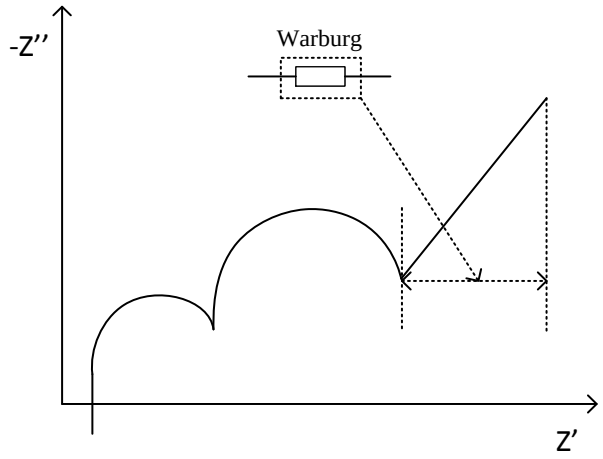

Figure 5.5 Interpretation of Warburg impedance in EIS

It is common to see a linear slope with an angle of 45º at low frequencies, e.g. typically 1 mHz – 1 Hz, in EIS curves, which is expressed as Warburg impedance, as shown in Figure 5.5. Warburg impedance at the low frequency end is used to characterize the diffusion process in batteries [79]. In brief, whenever diffusion effects completely dominate the electrochemical reaction mechanism, the impedance is called Warburg Impedance.

There are three expressions to describe Warburg Impedance. They are based on three different boundary conditions for the molarity *m* [75]:

- Semi-infinite diffusion: $m = m_0 = \text{const.}$ for $x \to \infty$

$$Z_{W\infty} = \frac{RT}{m_0 n^2 F^2 A_e} \frac{1}{\sqrt{j\omega D}} = \frac{\sigma}{\sqrt{\omega}}(1-j)$$
$$\sigma = \frac{RT}{m_0 n^2 F^2 A_e \sqrt{2D}} \tag{5.4}$$

where D is the diffusion constant of the diffusing species and A_e is the electrode surface.

- Ideal reservoir with constant molarity m_0 at finite distance l $m = m_0 = \text{const.}$ for $x = l$

$$Z_{WI} = \frac{RT}{m_0 n^2 F^2 A_e} \frac{\tanh(l \cdot \sqrt{j\omega / D})}{\sqrt{j\omega D}} \tag{5.5}$$

- Non-permeable wall with zero flux at finite distance l where $dm/dx = 0$ for $x = l$

$$Z_{WL} = \frac{RT}{m_0 n^2 F^2 A_e} \frac{\coth(l \cdot \sqrt{j\omega / D})}{\sqrt{j\omega D}} \tag{5.6}$$

where, n refers to number of electrons transferred. The expressions of the Warburg impedance should be selected based on different fitting situations. For example, if a linear slope of 45º can be observed, the first expression (5.4) should be applied to the fitting algorithm.

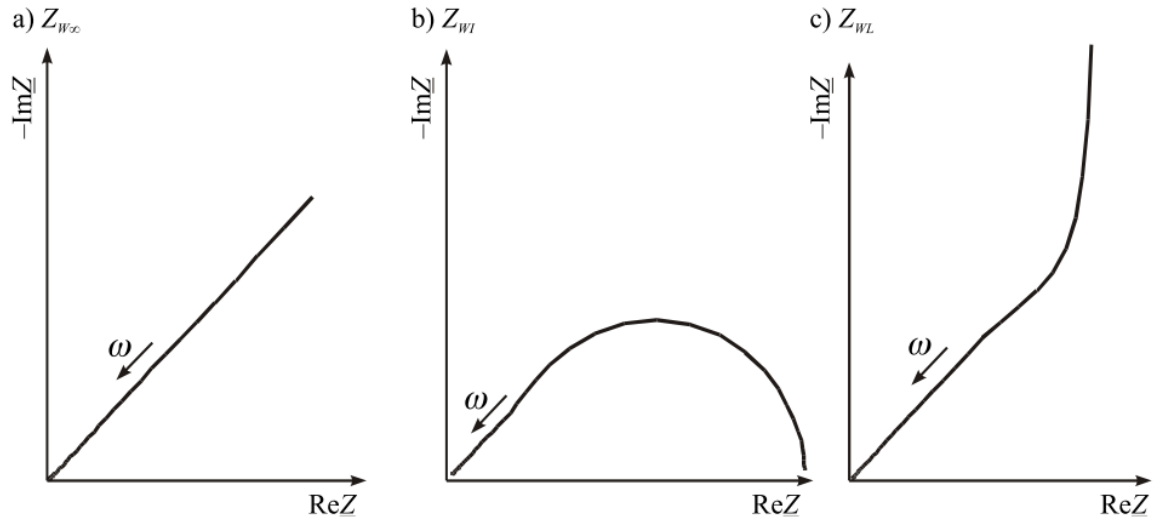

Figure 5.6 Theoretical plots of Warburg impedances with (a) semi-infinite diffusion layer, (b) limited diffusion layer and ideal reservoir at the boundary, (c) limited diffusion layer and non-permeable wall at the boundary (adopted from [75])

5.3 Fitting Algorithm

In order to fit the parameters of the ECM in Figure 5.1, an optimization algorithm should be applied. However, according to the literature review, it can be easily found that few studies are systematically and mathematically focusing on the fitting algorithm. In addition, more accurate extracted parameters lead to effective SOC/SOH estimation in frequency domain.

In this section, a novel quadratic programming based optimization algorithm will be applied to both single- and multi- curves fitting. This technique is able to achieve many features with regard to high accuracy, robustness and computation speed.

5.3.1 Single-Curve Fitting

Normally, the information obtained from EIS measurements are frequency, real part and imaginary part impedances; these are collected at one SOC level and temperature. Complex data points $Z_k = X_k + jY_k$ consist of real part X_k and imaginary part Y_k. Subscript k indicates the kth impedance and frequency point. The whole swept impedance data at specified SOC level is summarized as two complex data vectors as follows

$$\begin{aligned} \mathbf{x} &= \left[X_1, X_2, ..., X_n \right]^T \\ \mathbf{y} &= \left[Y_1, Y_2, ..., Y_n \right]^T \end{aligned} \tag{5.7}$$

Quadratic programming tool box in MATLAB is employed finding the optimal solution of $\bar{\mathbf{x}}$ to minimize the cost function shown in (5.8). Meanwhile, the boundary conditions and constraints can be defined for avoiding unrealistic results, e.g. fitted impedance is not supposed to be negative.

$$\min \bar{\mathbf{x}}^{\mathbf{T}}\mathbf{Q}\bar{\mathbf{x}} + \mathbf{p}^{\mathbf{T}}\bar{\mathbf{x}},$$
$$\text{Subject to } \begin{cases} \mathbf{A}\bar{\mathbf{x}} \le \mathbf{b} \\ \mathbf{A}_{\mathbf{eq}}\bar{\mathbf{x}} = \mathbf{b}_{\mathbf{eq}} \\ \mathbf{lb} \le \bar{\mathbf{x}} \le \mathbf{ub} \end{cases} \tag{5.8}$$

According to the analysis about the frequency-domain ECM in previous section, the model consists of a pure Ohmic resistance, two ZARC elements and a Warburg impedance, depicted in Figure 5.1. The reasons why two ZARC elements are selected are: 1) to have the same platform (2 RC model) with time-domain algorithm to compare these two parameter identification methods in terms of accuracy and robustness to sensor error, and 2) it has been validated two ZARC components provides more precise fitting results in [76] and [79].

The objective is to minimize the difference between measured complex impedance and fitted complex impedance, the objective function needs subtle changes in order to employ QP. The following equations are derived:

$$\begin{aligned} &\min \sum_{k=1}^{n} \left(\left(\hat{X}_k - X_k \right)^2 + \left(\hat{Y}_k - Y_k \right)^2 \right) \\ &= \min \left(\left(\mathbf{C}\boldsymbol{\theta} - \mathbf{x} \right)^T \left(\mathbf{C}\boldsymbol{\theta} - \mathbf{x} \right) + \left(\mathbf{D}\boldsymbol{\theta} - \mathbf{y} \right)^T \left(\mathbf{D}\boldsymbol{\theta} - \mathbf{y} \right) \right) \\ &= \min \left(\boldsymbol{\theta}^T \left(\mathbf{C}^T\mathbf{C} - \mathbf{D}^T\mathbf{D} \right)\boldsymbol{\theta} - 2\left(\mathbf{x}^T\mathbf{C} + \mathbf{y}^T\mathbf{D} \right)\boldsymbol{\theta} + \mathbf{x}^T\mathbf{x} + \mathbf{y}^T\mathbf{y} \right) \end{aligned} \tag{5.9}$$

where, **x** and **y** can be referred to (5.7). $\hat{X}_k = \mathbf{c}_k^T\boldsymbol{\theta}$, $\hat{Y}_k = \mathbf{d}_k^T\boldsymbol{\theta}$ with linear regressed parameters vector $\boldsymbol{\theta} = \begin{bmatrix} R_o & R_1 & R_2 & \dots & R_n & W_g \end{bmatrix}^T$ and $\mathbf{c}_k$ and $\mathbf{d}_k$ are functions of not only frequency but also time constants and depression factors. The reason why the latter two elements are included as known variables will be explained later in the chapter. A set of $\mathbf{c}_k$ and $\mathbf{d}_k$ over the whole

frequency range formed the matrix functions $\mathbf{C}=\begin{bmatrix}\mathbf{c}_1 & \mathbf{c}_2 & \dots & \mathbf{c}_m\end{bmatrix}^T$ $\mathbf{D}=\begin{bmatrix}\mathbf{d}_1 & \mathbf{d}_2 & \dots & \mathbf{d}_m\end{bmatrix}^T$. In both matrices, *m* stands for the number of frequency points.

Based on (5.9), corresponding matrices **C**, **D** and **θ** can be derived. In frequency domain, the admittance of the CPE is $C(j\omega)^{\alpha}$. As described previously, *C* denotes a generalized capacitance and α refers to the depression factor. So the impedance of CPE can be derived as follows:

$$\begin{aligned}\frac{1}{\frac{1}{R_i}+(j\omega)^{\alpha_i}C_i} &= \frac{R_i}{1+\tau_i(j\omega)^{\alpha_i}} \\ &= \frac{R_i}{1+\tau_i\omega^{\alpha_i}\cos(\frac{\pi}{2}\alpha_i)+j\tau_i\omega^{\alpha_i}\sin(\frac{\pi}{2}\alpha_i)} \\ &= \frac{R_i(1+\tau_i\omega^{\alpha_i}\cos(\frac{\pi}{2}\alpha_i)-j\tau_i\omega^{\alpha_i}\sin(\frac{\pi}{2}\alpha_i))}{1+2\tau_i\omega^{\alpha_i}\cos(\frac{\pi}{2}\alpha_i)+\tau_i^2\omega^{2\alpha_i}(\sin^2(\frac{\pi}{2}\alpha_i)+\cos^2(\frac{\pi}{2}\alpha_i))} \\ &= R_i\Big(\underbrace{\frac{1+\tau_i\omega^{\alpha_i}\cos(\frac{\pi}{2}\alpha_i)}{1+2\tau_i\omega^{\alpha_i}\cos(\frac{\pi}{2}\alpha_i)+\tau_i^2\omega^{2\alpha_i}}}_{Part\ of\ matrix\ \mathbf{C}} - j\underbrace{\frac{\tau_i\omega^{\alpha_i}\sin(\frac{\pi}{2}\alpha_i)}{1+2\tau_i\omega^{\alpha_i}\cos(\frac{\pi}{2}\alpha_i)+\tau_i^2\omega^{2\alpha_i}}}_{Part\ of\ matrix\ \mathbf{D}}\Big)\end{aligned} \tag{5.10}$$

where, according to Euler's formula and polar form for fractional powers of complex numbers $\left(re^{j\phi}\right)^{\alpha}=r^{\alpha}e^{j\phi\alpha}$

$$\begin{aligned}(j\omega)^{\alpha} &= (\omega j e^{j\frac{\pi}{2}})^{\alpha} = \omega^{\alpha} j e^{j\frac{\pi}{2}\alpha} \\ &= \omega^{\alpha}\left(\cos(\frac{\pi}{2}\alpha)+j\sin(\frac{\pi}{2}\alpha)\right)\end{aligned} \tag{5.11}$$

Obviously, R_i shows highly nonlinear behavior with $\tau_i = R_iC_i$ and α_i, which means that τ_i and α_i are not optimizable through QP. QP can only be applied when τ_i and α_i are assumed as constants.

Instead, the values of τ_i and α_i are determined by an outer loop by sweeping possible τ_i and α_i values within a certain range. Another assumption is made: τ_i and α_i remain constant at the same SOC range not considering varying frequencies. This assumption is validated and applied by Jong-Hak Lee and Woojin Choi [39]. So R_i would be a part of fitted parameters in vector $\boldsymbol{\theta}$, and the rest parts in (5.10) would be assigned to corresponding matrices **C** and **D** as described above.

Because of the equation's simplicity and generality for most cases, (5.4) has been selected as the prior expression of Warburg impedance in frequency-domain fitting.

Therefore, the impedance can be derived as

$$\begin{aligned}\hat{Z}_k = & \underbrace{R_o}_{\text{Ohmic resistance}} + \underbrace{\sum_{i=1}^{n}\left[R_i\left(\frac{1+\tau_i\omega_k^{\alpha_i}\cos(\frac{\pi}{2}\alpha_i)}{1+2\tau_i\omega_k^{\alpha_i}\cos(\frac{\pi}{2}\alpha_i)+\tau_i^2\omega_k^{2\alpha_i}} - j\frac{\tau_i^2\omega_k^{\alpha_i}\sin(\frac{\pi}{2}\alpha_i)}{1+2\tau_i\omega_k^{\alpha_i}\cos(\frac{\pi}{2}\alpha_i)+\tau_i^2\omega_k^{2\alpha_i}}\right)\right]}_{\text{ZARC elements}} \\ & + \underbrace{\frac{Wg}{\sqrt{\omega_k}}(1-j)}_{\text{Warburg impedance}} \\ = & \hat{X}_k + j\hat{Y}_k = \mathbf{c}_k\theta + j\mathbf{d}_k\theta\end{aligned} \tag{5.12}$$

$$\mathbf{c}_k = \left[1 \quad \underbrace{\frac{1+\tau_1\omega_k^{\alpha_1}\cos(\frac{\pi}{2}\alpha_1)}{1+2\tau_1\omega_k^{\alpha_1}\cos(\frac{\pi}{2}\alpha_1)+\tau_1^2\omega_k^{2\alpha_1}} \quad \cdots \quad \frac{1+\tau_n\omega_k^{\alpha_n}\cos(\frac{\pi}{2}\alpha_n)}{1+2\tau_n\omega_k^{\alpha_n}\cos(\frac{\pi}{2}\alpha_n)+\tau_n^2\omega_k^{2\alpha_n}}}_{\text{n ZARC elements}} \quad \frac{1}{\sqrt{\omega_k}}\right]^T \tag{5.13}$$

$$\mathbf{d}_k = \left[0 \quad \underbrace{\frac{-\tau_1\omega_k^{\alpha_1}\sin(\frac{\pi}{2}\alpha_1)}{1+2\tau_1\omega_k^{\alpha_1}\cos(\frac{\pi}{2}\alpha_1)+\tau_1^2\omega_k^{2\alpha_1}} \quad \cdots \quad \frac{-\tau_n\omega_k^{\alpha_n}\sin(\frac{\pi}{2}\alpha_n)}{1+2\tau_n\omega_k^{\alpha_n}\cos(\frac{\pi}{2}\alpha_n)+\tau_n^2\omega_k^{2\alpha_n}}}_{\text{n ZARC elements}} \quad \frac{1}{\sqrt{\omega_k}}\right]^T \tag{5.14}$$

Equations (5.12)-(5.14) can be substituted into (5.8) to utilize the built-in QP function in MATLAB. These all are based on fixed/known time constants and depression factors, which leads to the demand of a pre-process to determine these values and feed them back to the main QP function. A two-stage algorithm is summarized in Figure 5.7.

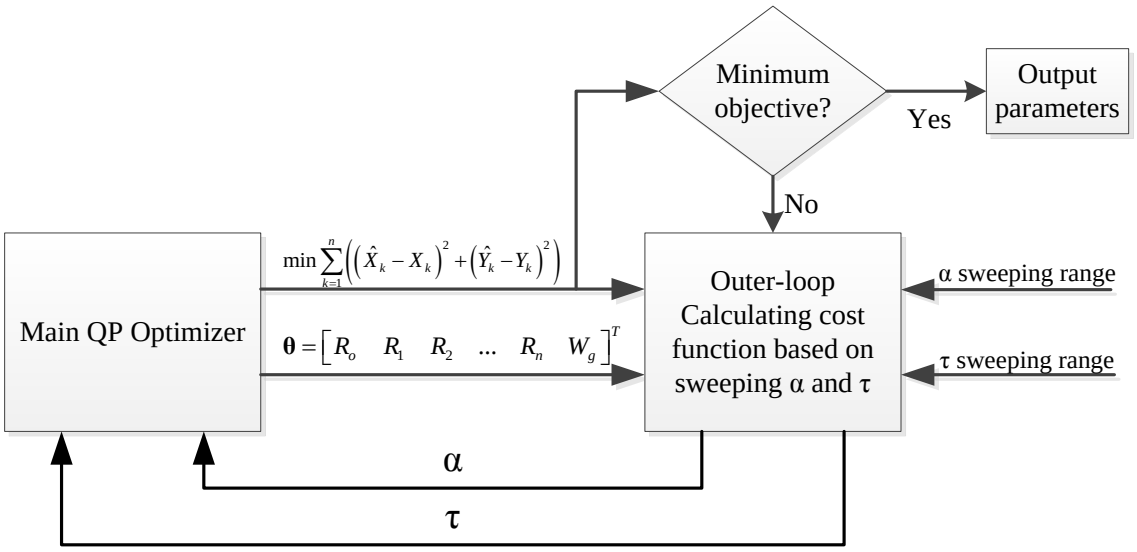

Figure 5.7 Overall frequency domain fitting algorithm

5.3.2 Multi-Curve Fitting

As Section 4.4.1 stated about time domain fitting based on full SOC range, an auxiliary vector is necessary to apply single level fitting to multi-level fitting. The vector, $\mathbf{z}_k^T = \begin{bmatrix} 0 & \cdots & 0 & \lambda & 1-\lambda & 0 & \cdots & 0 \end{bmatrix}$ is employed here; a detailed explanation of this vector has been given in Section 4.4.1. The parameter vector is expanded to full SOC range:

$$\boldsymbol{\theta} = \left[R_o^{SOC=0\%} \ldots R_o^{SOC=100\%} \underbrace{R_1^{SOC=0\%} \ldots R_1^{SOC=100\%} \ldots R_n^{SOC=0\%} \ldots R_n^{SOC=100\%}}_{n \text{ ZARC elements}} Wg^{SOC=0\%} \ldots Wg^{SOC=100\%} \right]^T \quad (5.15)$$

Correspondingly, the new vectors **c** and **d** are derived as follows

$$\mathbf{c}_k = \left[1 \quad \underbrace{\frac{1+\tau_1\omega_k^{\alpha_1}\cos(\frac{\pi}{2}\alpha_1)}{1+2\tau_1\omega_k^{\alpha_1}\cos(\frac{\pi}{2}\alpha_1)+\tau_1^2\omega_k^{2\alpha_1}} \quad \cdots \quad \frac{1+\tau_n\omega_k^{\alpha_n}\cos(\frac{\pi}{2}\alpha_n)}{1+2\tau_n\omega_k^{\alpha_n}\cos(\frac{\pi}{2}\alpha_n)+\tau_n^2\omega_k^{2\alpha_n}}}_{\text{n ZARC elements}} \quad \frac{1}{\sqrt{\omega_k}} \right] \otimes \mathbf{z}_k^T$$

$$\mathbf{d}_k = \left[0 \quad \underbrace{\frac{-\tau_1\omega_k^{\alpha_1}\sin(\frac{\pi}{2}\alpha_1)}{1+2\tau_1\omega_k^{\alpha_1}\cos(\frac{\pi}{2}\alpha_1)+\tau_1^2\omega_k^{2\alpha_1}} \quad \cdots \quad \frac{-\tau_n\omega_k^{\alpha_n}\sin(\frac{\pi}{2}\alpha_n)}{1+2\tau_n\omega_k^{\alpha_n}\cos(\frac{\pi}{2}\alpha_n)+\tau_n^2\omega_k^{2\alpha_n}}}_{\text{n ZARC elements}} \quad \frac{1}{\sqrt{\omega_k}} \right] \otimes \mathbf{z}_k^T \tag{5.16}$$

5.3.3 Cost Functions for Outer-Loop Function

The outer-loop function has a purpose for minimizing a cost function to determine suitable time constants and depression factors based on a global minimum. A few candidates of cost functions have been investigated and are listed in (5.17), (5.19) and (5.20).

$$\text{Cost} = \sum_{i=1}^{k}[\gamma\frac{(\hat{Z}_{mol,i}-Z_{mol,i})}{Z_{mol,i}}+(1-\gamma)\frac{(\hat{\theta}_{mol,i}-\theta_{mol,i})}{\theta_{mol,i}}] \tag{5.17}$$

$$\begin{aligned} Z_{mol,i} &= 20\log(\sqrt{Z'+Z''^2}) \\ \theta &= \arctan(Z''/Z')\times 360/2\pi \end{aligned} \tag{5.18}$$

$$\text{Cost} = \log(\sum_{i=1}^{k}\gamma(\hat{Z}_i'-Z_i')+(1-\gamma)(\hat{Z}_i''-Z_i'')) \tag{5.19}$$

$$\text{Cost} = \log(\sum_{i=1}^{k}\gamma(\hat{Z}_i'-Z_i')+(1-\gamma)(\hat{Z}_i''-Z_i''))^2 \tag{5.20}$$

where, γ refers to the weighting which can be tuned adjustly.

5.4 Simulation and Experimental Validations

5.4.1 Simulation and Sensitivity Study

In order to validate the fitting algorithm and the most suitable cost function, as shown before, an artificial EIS curve is generated by (5.12) in MATLAB. Given the pre-defined parameters summarized in Table 5.1, the simulated EIS curve is plotted in Figure 5.8 for the purpose of validation.

Table 5.1: Parameters of artificial EIS curve

Parameters	R_o	R_a	C_a	R_b	C_b	α_1	α_2	*Warburg*
Value	$3\,\Omega$	$4\,\Omega$	0.5 F	$10\,\Omega$	10 F	1	1	0.1

The time constants for two ZARC elements are set as 2 s and 100 s, respectively. As described previously, the time constants should be pre-determined by sweeping possible solutions based on three cost functions. The sweeping range is from 1-50 s for τ_1 and 1-100s for τ_2. Then the most promising time constants will be outputted. For initialization of θ in the QP based algorithm, only R_o is initialized by the minimum of Za in EIS. This is because normally the minimum of Za is at the intersection of real axis and EIS curve, which is interpreted as Ohmic resistance. It is the best guess of R_o. Other parameters remain initialized as zeros; this is acceptable thanks to the highly robust fitting algorithm. The ability to find the global fitting minimum is one of the advantages of the proposed QP based algorithm.

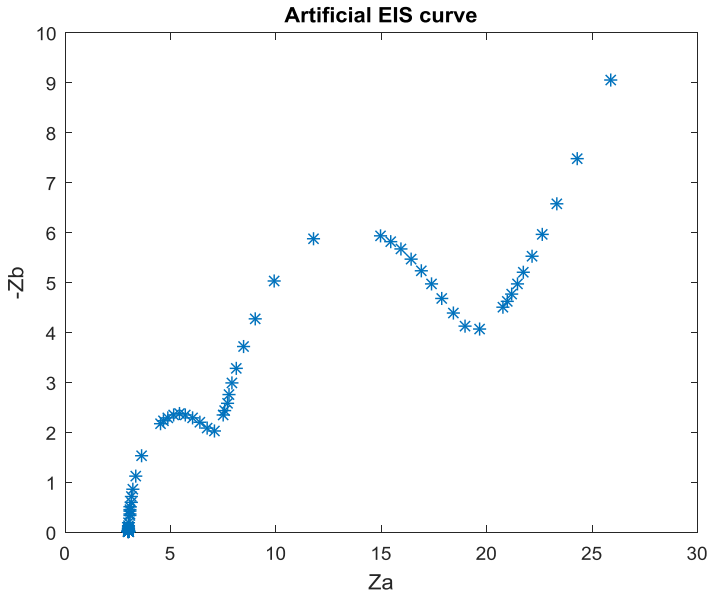

Figure 5.8 Artificial EIS curve based on the parameters in Table 5.1

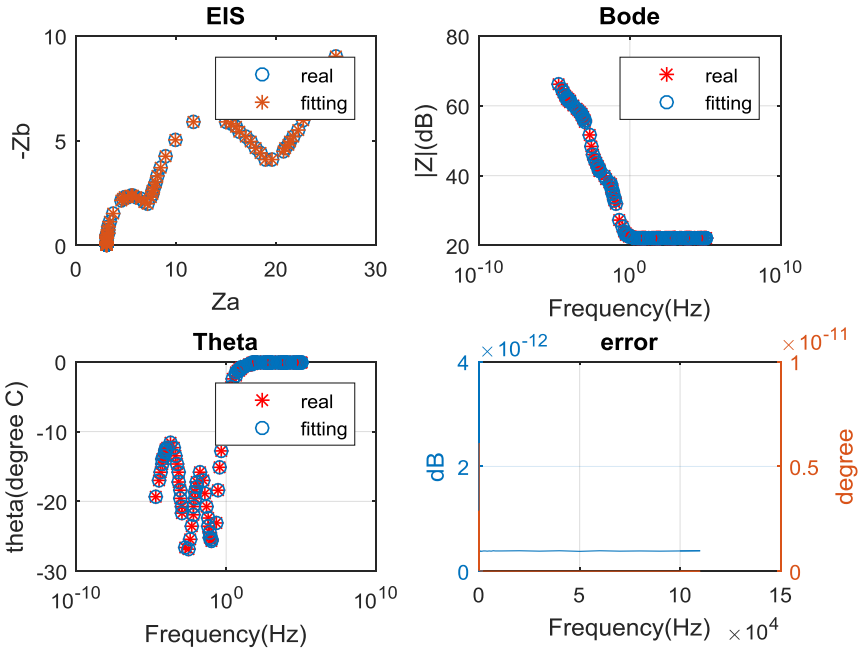

Figure 5.9 Fitting results based cost function 1, left top: EIS fitting, right top: Bode magnitude plot, left bottom: Bode phase plot, right bottom: error based on Bode magnitude and phase

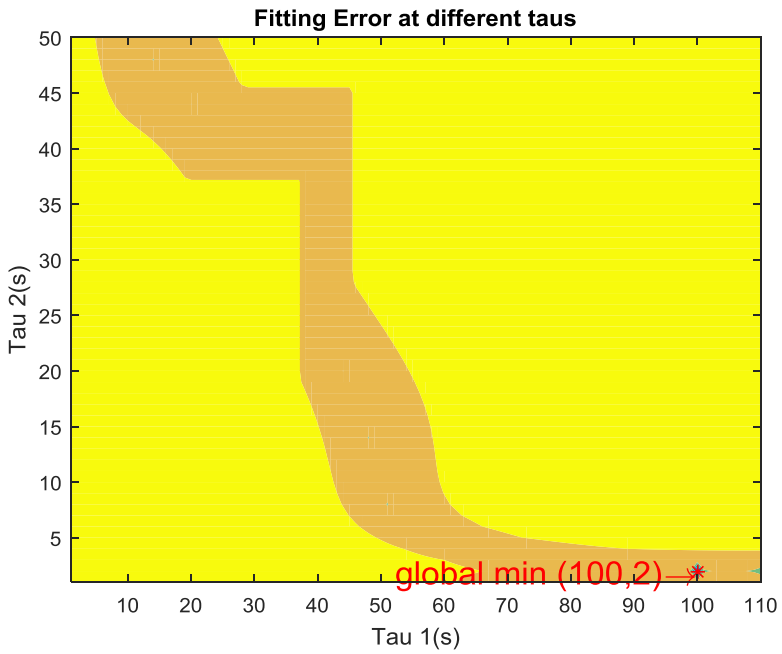

Figure 5.10 Result of sweeping τ based on cost function (5.17)

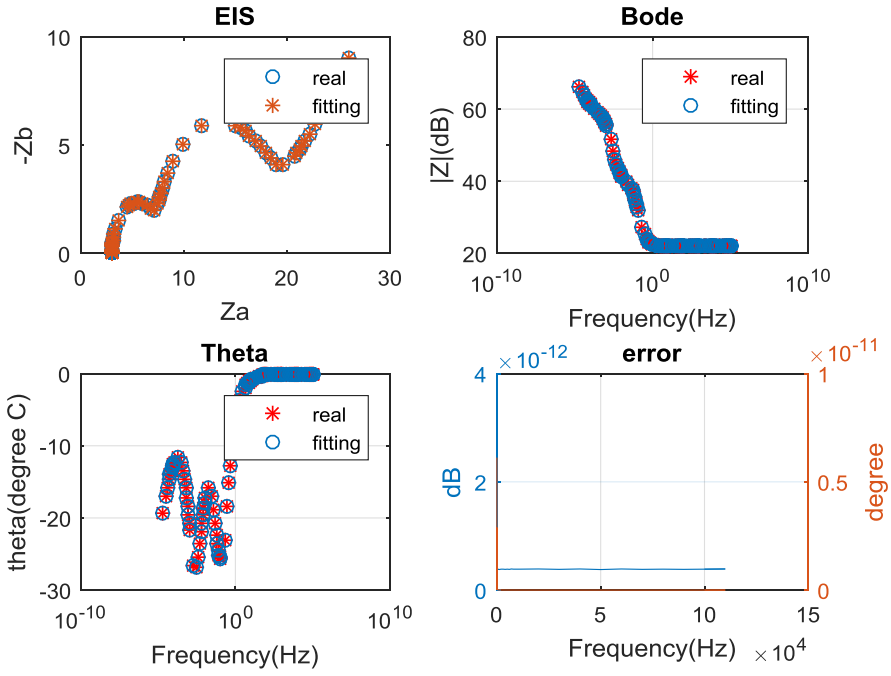

Figure 5.11 Fitting results based cost function 1, left top: EIS fitting, right top: Bode magnitude plot, left bottom: Bode phase plot, right bottom: error based on Bode magnitude and phase

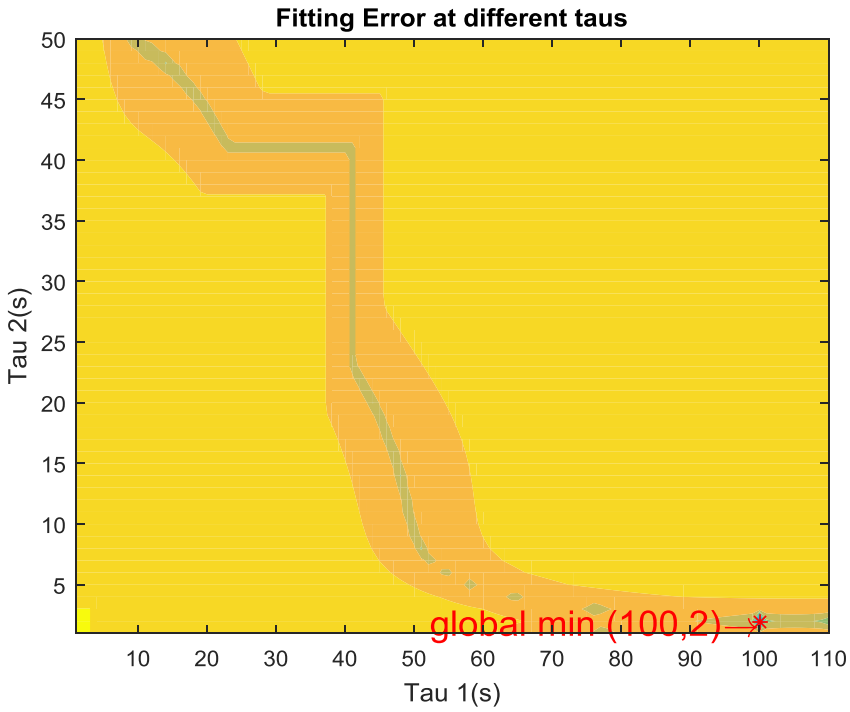

Figure 5.12 Result of sweeping τ based on cost function (5.19)

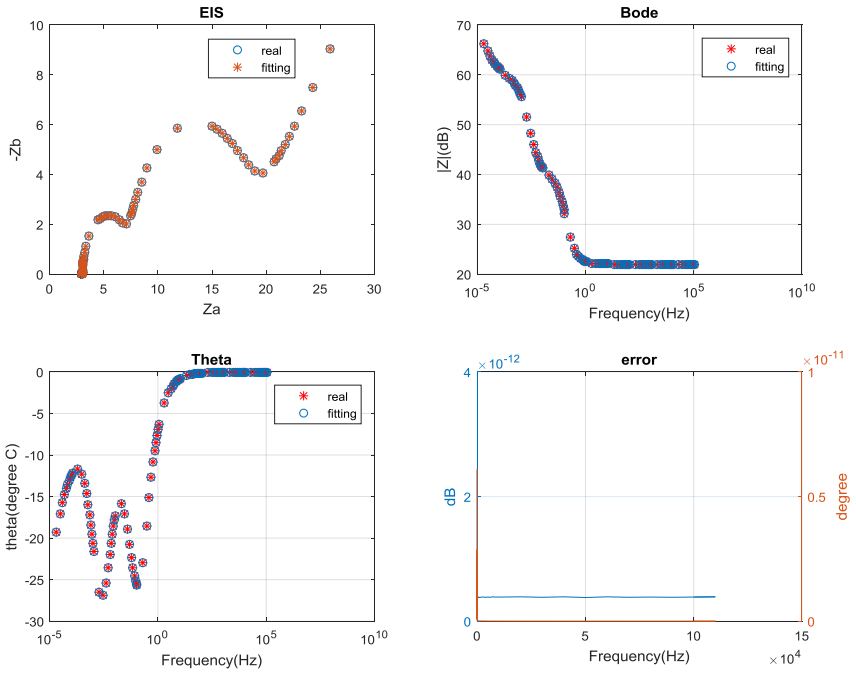

Figure 5.13 Fitting results based cost function 3, left top: EIS fitting, right top: Bode magnitude plot, left bottom: Bode phase plot, right bottom: error based on Bode magnitude and phase

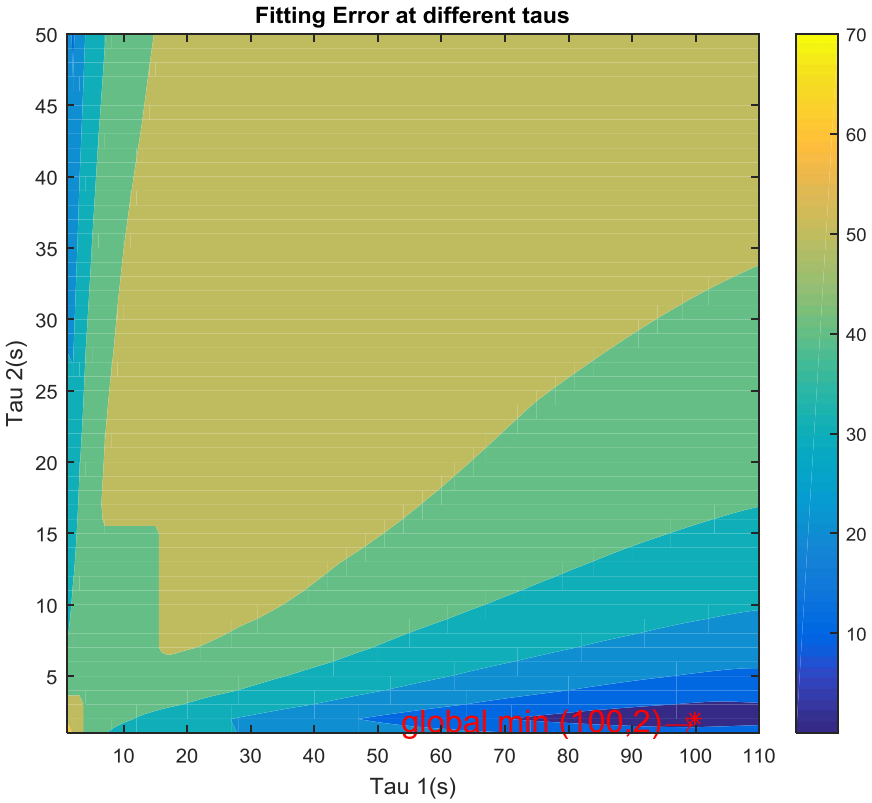

Figure 5.14 Result of sweeping τ based on cost function (5.20)

Table 5.2: Fitted parameters of artificial EIS curve

Parameters	R_o	R_a	C_a	R_b	C_b	α_1	α_2	***Warburg***
True Value	3Ω	4Ω	0.5 F	10Ω	10 F	1	1	0.1
Cost Function 1	3Ω	4Ω	0.5 F	10Ω	10 F	1	1	0.1
Cost Function 2	3Ω	4Ω	0.5 F	10Ω	10 F	1	1	0.1
Cost Function 2	3Ω	4Ω	0.5 F	10Ω	10 F	1	1	0.1

Figure 5.9 and Figure 5.10 show the fitting results of EIS curve and sweeping τ. In Figure 5.10, the cooler the color is, the less the fitting error is. Due to lack of frequency information in Nyquist plot, two bode plots express the magnitude and phase shift of the frequency response. It can be observed that the minimum of τ is determined as 2 s and 100 s based on cost function (5.19), leading to perfect estimation between estimated EIS and known EIS. The situations for cost function (5.19) and cost function (5.20) are basically similar with cost function (5.17), shown in Figure 5.11 and Figure 5.14. A summary table of the fitted parameters is given in Table 5.2

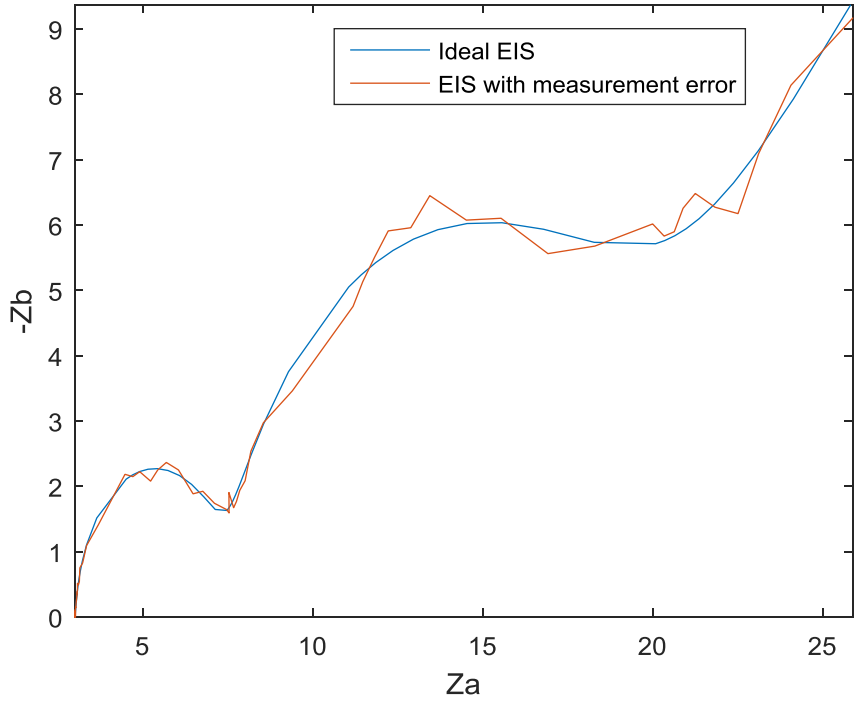

Figure 5.15 The comparison between ideal EIS curve and EIS curve with +/- 1 % amplitude and +/- 0.5º phase angle measurement noise

Additional comparisons were performed in simulation considering the accuracy of a Frequency Response Analyzer (FRA) from Solartron Analytical. According to its manual, this FRA would give the results of amplitudes and phase angel with +/- 0.1 % and +/- 0.1º error, respectively. Inserting this error into the artificial EIS curve would reflect this tool's practical fitting

performance in. MATLAB functions 'awng' and 'normrng' are used for adding the error of amplitude and phase angle. +/- 0.1% amplitude and +/- 0.1° are too little to have influence on the EIS curve, higher errors are added using +/- 1% amplitude and +/- 1° phase angle. The comparison between ideal EIS curve and EIS curve with error is shown in Figure 5.15. In addition, 0.8 and 0.9 depression factors for two ZARC elements are added to validate the fitting tool under more realistic condition.

Table 5.3: Comparison between fmincon and QP based algorithms on fitting results

Parameters	R_o	R_a	C_a	R_b	C_b	α_1	α_2	**Warburg**
True Value	3Ω	4Ω	0.5 F	10Ω	15 F	0.7	0.9	0.1
Fmincon 1.53 s	2.9608 (1.31%)	4.3676 (9.19%)	0.5021 (0.42%)	9.3575 (6.43%)	20.5724 (37.1%)	0.6707 (4.19%)	0.9415 (3.73%)	0.1029 (2.9 %)
QP 1.38 s	2.9699 (1%)	3.9297 (1.75%)	0.4836 (3.28%)	10.0202 (0.2%)	14.9863 (0.09%)	0.7053 (0.76%)	0.9024 (0.27%)	0.1006 (0.6%)

As a comparison, 'fmincon' optimization toolbox function in MATLAB is used to fit the same EIS curve. The same cost function (5.17) and initialization are used in both fmincon and quadratic programming. As a result, a comparison table is summarized in Table 5.3 including the accuracy level of fitted parameters and computing time. This simulation is run on a laptop with i7-6700 HQ 2.5GHz CPU and 16 GB RAM.

It can be concluded from Table 5.3 that 1) QP is running faster than fmincon, 1.38 s vs. 1.53 s. 2) Robustness: measurement noise has less effect on the accuracy of QP based algorithm than fmincon function.

These two advantages are basically the result of convex model that QP algorithm applies. This least square based algorithm can directly find the global minimum instead of falling into local minimum.

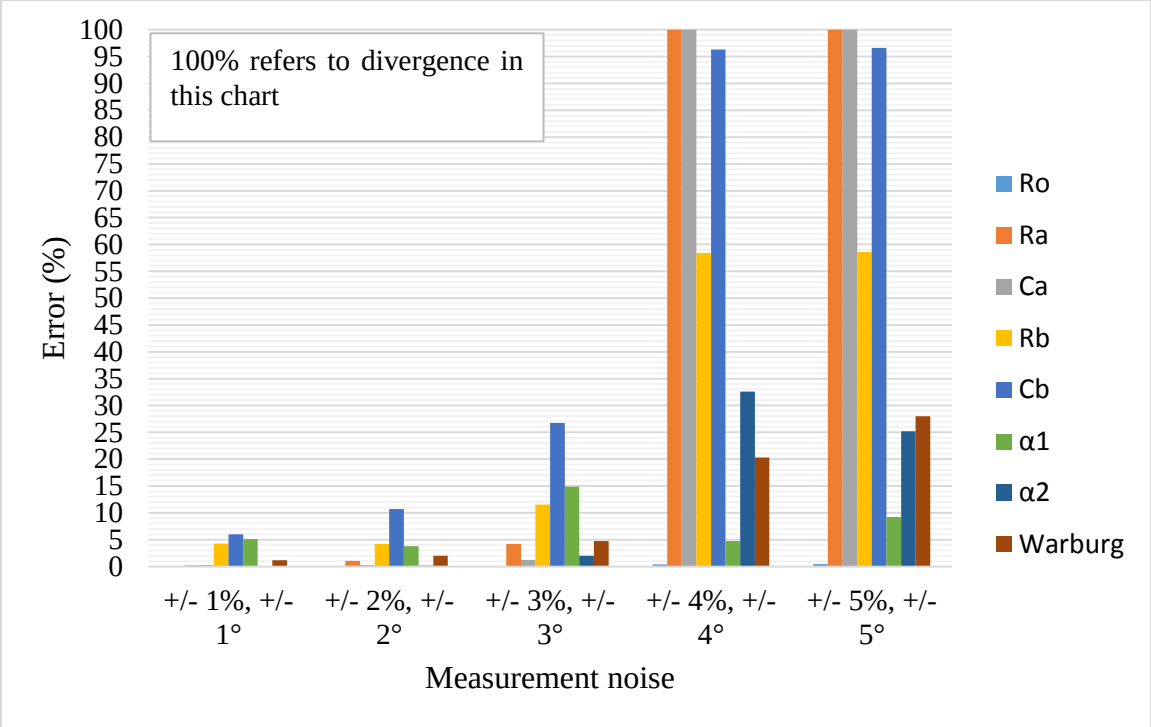

(a)

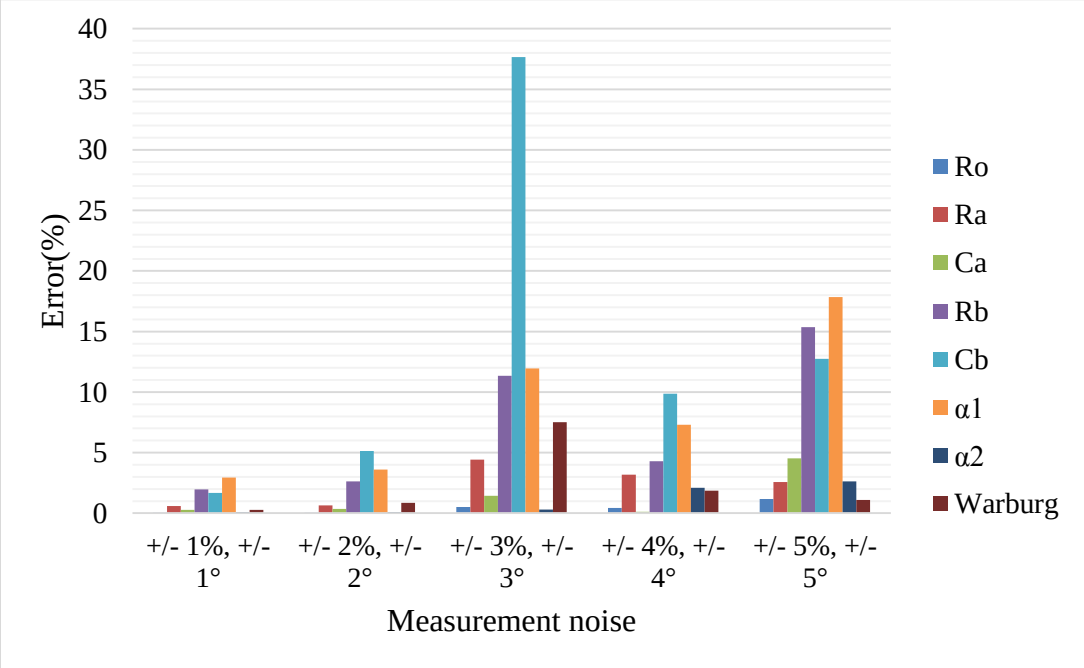

(b)

Figure 5.16 Fitting errors of ECM parameters for (a) fmincon, (b) QP

In addition to the noise level mentioned above, extensive sensitivity study is carried out based on +/- 1% - +/- 5% amplitude noise and +/- 1° - +/- 5° phase angle noise to determine which approach is better. Two graphs illustrating the error on each ECM element for both fmincon and QP based fitting algorithms are plotted in Figure 5.16. It is noted that '100% error' refers to divergence in Figure 5.16, i.e. the approach is not able to capture the parameters in a reasonable range.

There are two conclusions that can be drawn from this figure. 1) Even though, at certain noise level (3%), fmincon based method outperforms QP based approach by 10% on fitting C_b element, QP based algorithm has better accuracy. 2) As summarized before, quadratic programming is more likely to find the global minimum. It is the reason why QP is more robust. On the contrary, fmincon can easily be trapped in local minimum, which explains why this method diverges under high-level noise (4% and 5%).

5.4.2 Experimental Results

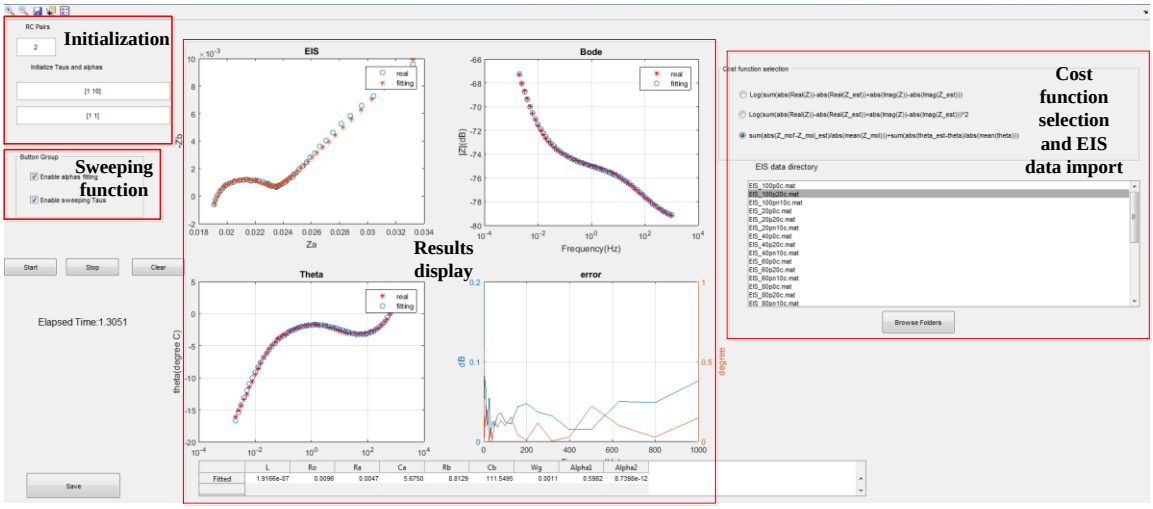

Figure 5.17 Graphical user interface for EIS curve fitting

An EIS fitting tool with GUI is developed and is used for the rest of the study, as shown in Figure 5.17. The EIS tests are performed at three different temperatures (-10, 0 and 20 ºC) and every 20% SOC. The 20% SOC is calculated by the capacity at each corresponding temperature. For instance, the nominal capacity is captured as 8.187 Ah at 20 ºC. Once 8.187 Ah × 20% = 1.64 Ah is discharged, it refers to 20% SOC is removed from the battery pack. The EIS curves at -10, 0 and 20 ºC are illustrated in Figure 5.18 - Figure 5.20.

At lower temperatures, both semi-circles expand in a more significant way; this is also observed by other researchers [80]. The first semi-circle is dominated by solid electrolyte interface (SEI). The second semi-circle is associated with charge transfer resistance and double layer capacity. The phenomenon can be explained by lower kinetic energy when the ions have less thermal energy; therefore ions have difficulties to pass through the interface.

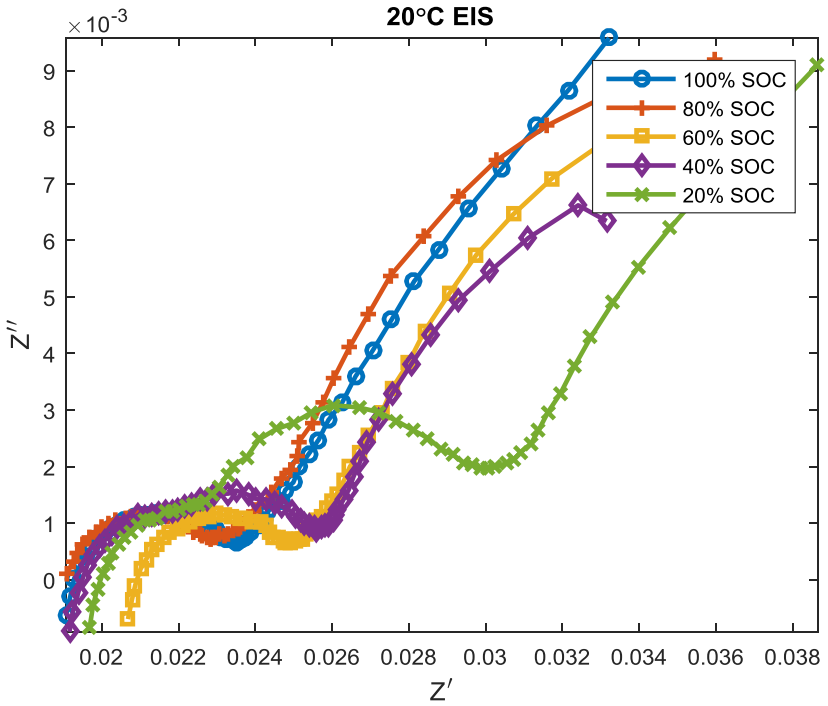

Figure 5.18 EIS curves at 20 ºC

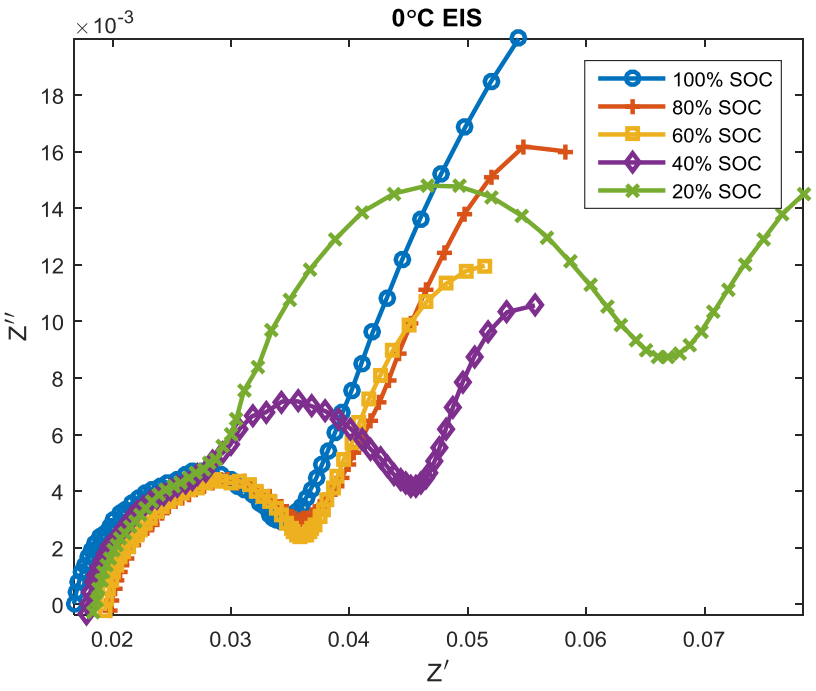

Figure 5.19 EIS curves at 0 ºC

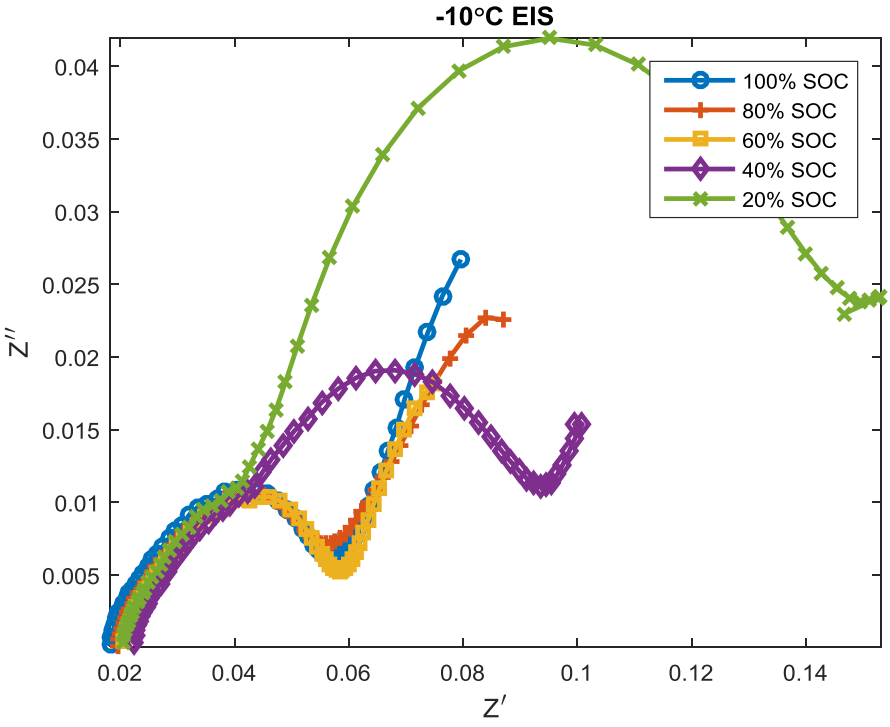

Figure 5.20 EIS curves at -10 ºC

It is reflected as higher resistance in EIS. Another interesting trend can be also found. The semi-circles appear at low SOC, such as the 20% SOC curve in Figure 5.18, the 20% and 40% SOC curves in Figure 5.19, and the 20% and 40% SOC curves in Figure 5.20. It shows that the charge transfer and diffusion resistance are dependent on not only temperature but SOC/voltage.

The three EIS curves are fitted employing the proposed frequency domain fitting algorithm. Two of the samples are shown in Figure 5.21 and Figure 5.22 to reflect the performance of the fitting tool. Amplitude and phase angle errors are depicted as well. They are more suitable to assess a Nyquist plot since the frequency information is included. It can be seen from Figure 5.21 that the amplitude and phase angle errors are less than 0.05 dB and 0.1° (1% error), respectively.

The proposed fitting tool is able to capture most characterizations accurately except at low frequency. Slight misinterpretations can be observed at the low frequency where Warburg contributes to the frequency response. It is caused by the model of Warburg coefficient used in the algorithm. A simple function is used to express Warburg coefficient in (5.4), which reflects a perfect 45º slope in Nyquist. However, in the experimental data, the slope at low frequency cannot be ideally modeled as perfect 45º. Instead, it should be exhibited by a combination of equations (5.4) - (5.6). This can be done in the future to increase the fidelity of this fitting tool.
The parameters extracted from EIS tests are illustrated in Figure 5.23. The results further validate the theoretical analysis above. The SEI resistance *Ra* and charge transfer resistance *Rb* show the dependency on temperatures and SOC. The inductance *L* has no clear relationship with temperature, which is also observed in [80], since the inductivity is mainly caused by the current conduction which is insensitive to temperature.

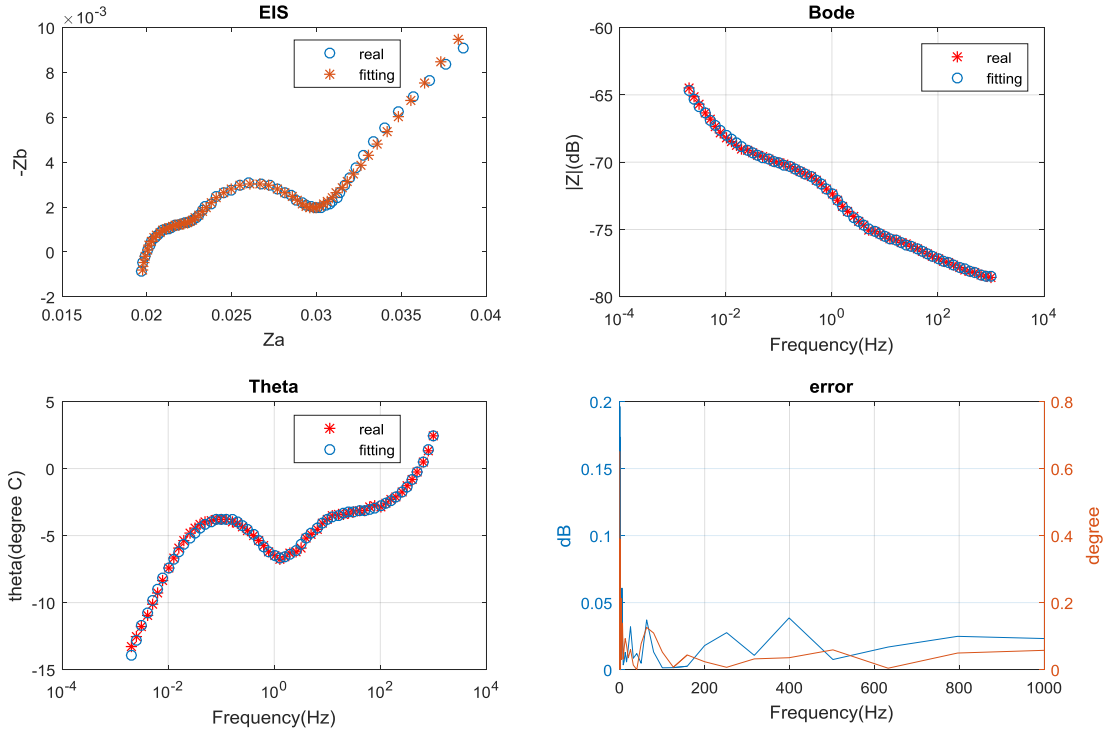

Figure 5.21 Fitting results at SOC = 20% and temperature at 20 ºC

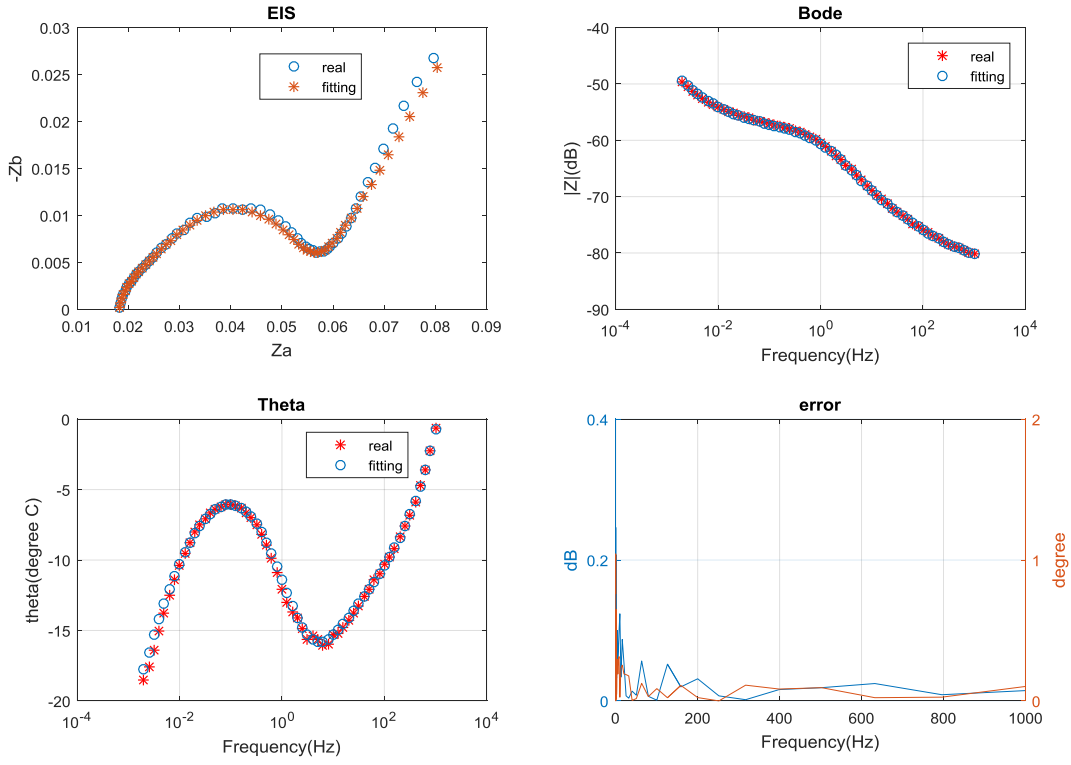

Figure 5.22 Fitting results at SOC = 100% and temperature at -10 ºC

It might be expected to observe that Ohmic resistance *Ro* elevates with decreasing temperature due to descending viscosity of the electrolyte [80]. However, in this case, Ro intends to fluctuate around a certain value. Since the EIS test is conducted based on a module level instead of cell level, it probably can be explained by the fact that the cells' Ohmic resistances and sensitivities to temperature in a module are unbalanced. There is another possible explanation of this phenomenon. The EIS tests are usually performed without bias DC current. It has been observed by many researchers that the EIS curves shift right with DC bias current, i.e. higher Ohmic resistance is observed at higher DC bias current [81]. On the contrast to EIS tests, HPPC test is performed at certain level of current pulse. It is expected to see Ohmic resistance extracted from EIS matches the resistance extracted from HPPC test when DC bias current is inserted in EIS tests.

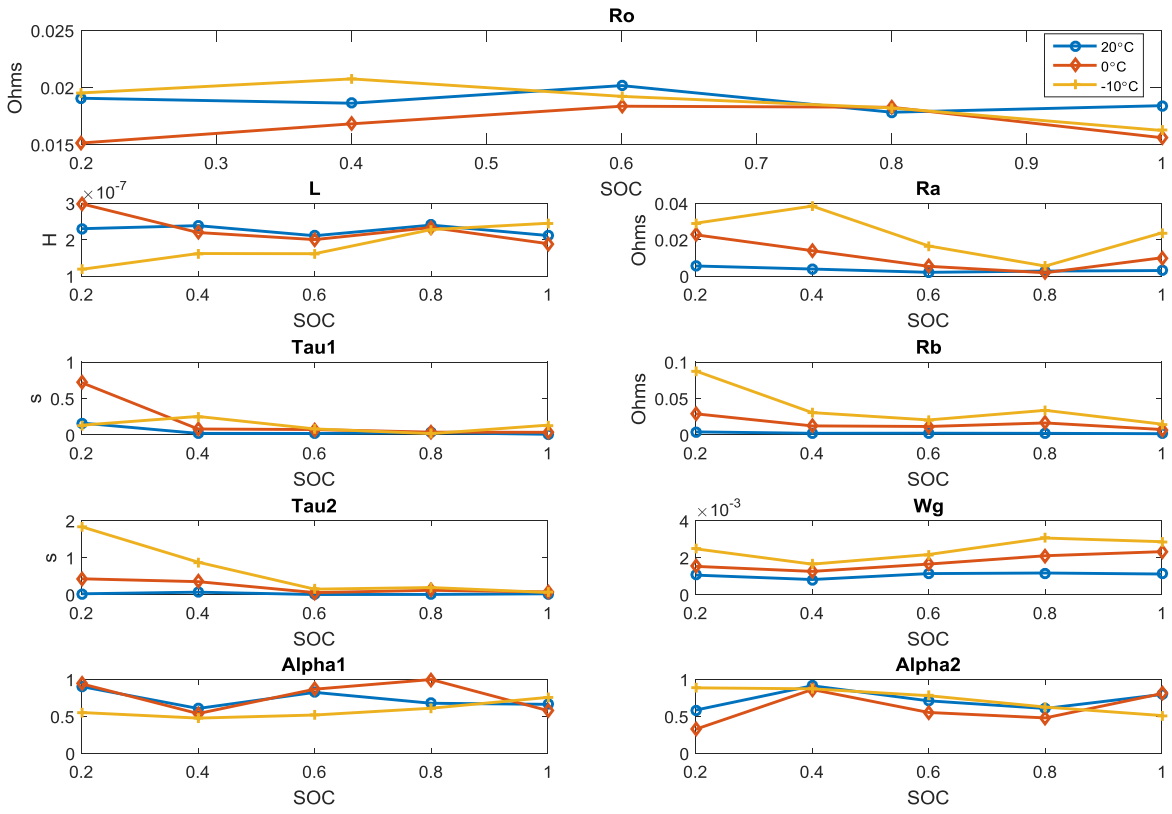

Figure 5.23 ECM parameters extracted from experimental EIS curves

The parameters extracted from HPPC and EIS tests are compared in Figure 5.24. Only resistances are illustrated because the EIS ECM and HPPC ECM have agreements on theses parameters. Others, e.g. CPE which cannot be modeled in time domain, are excluded. That is, it is comparable on resistances instead of CPE and Warburg impedance due to nontransferable parameters to time domain.

At 20 °C, R_o shows significant agreement on both tests. For 0 and -10 °C, R_o from HPPC tests is expected since the trend is that the Ohmic resistance grows with the decreasing temperature, this has been observed by many researchers [80] [82] [83]. However, R_o from EIS test shows insensitivity to temperature.

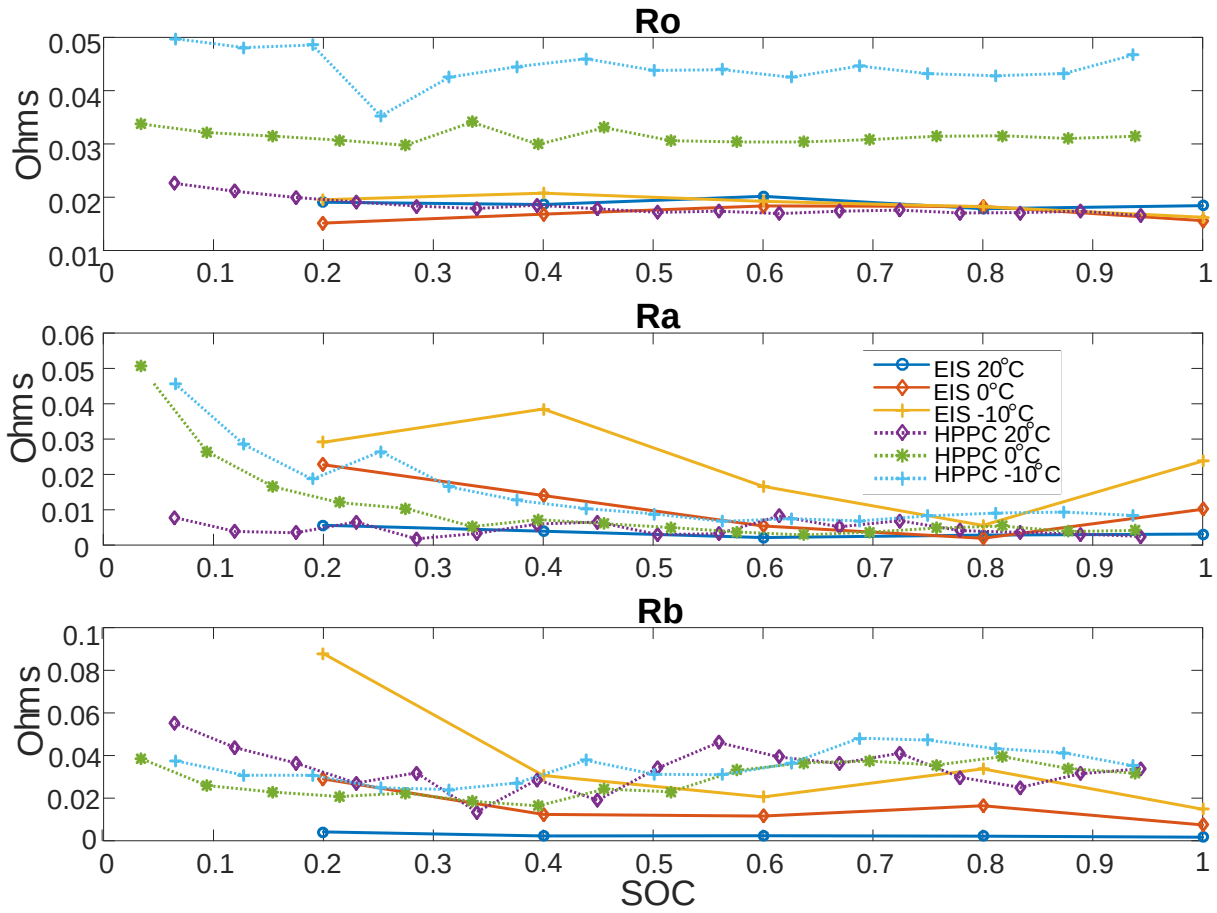

Figure 5.24 Comparison between the parameters extracted from experimental HPPC and EIS tests

5.5 Conclusion

A detailed EIS battery model has been described in this chapter. The modeling is further applied to a novel QP based fitting algorithm. The novel algorithm requires no initialization, so manual adjustments are not necessary even when the variations of each parameter are significant at a single SOC level. Applying a masking vector enables the multi-curve fitting to further speed up the fitting process. A sensitivity study on the proposed fitting algorithm shows its abilities to converge to true references when the measurement noises are dominant. Experimental EIS results are discussed about the dependency of EIS parameters to temperature and SOC level, and are processed by proposed fitting algorithm. Less than 1% amplitude and phase angle error are observed in fitting results. The correlation between the parameters extracted from HPPC and EIS was also discussed.

Chapter 6

BATTERY MODELING AND SOC ESTIMATION

6.1 Introduction

In order to accurately estimate SOC, the BMS employs a high fidelity model along with a robust state and parameter estimation strategy to extract valuable information based on the model. The accuracy of SOC depends mainly on model fidelity and estimation strategy robustness to modeling and sensor noise uncertainties. This chapter focuses mainly on battery modeling and SOC estimation since they are strongly tied to riding range which is of importance for riders.

In this chapter, the contributions can be summarized as a comparison among the extended Kalman filter, Sigma point Kalman filter, Cubature Kalman filter, and Joint extended Kalman filter for battery SOC estimation. The second-order equivalent circuit-based model has been used for the basis of comparison. Estimation strategies have been compared in terms of their accuracy, robustness and computational complexity. This chapter is organized as follows: Section 6.2 will be mainly focusing on validation of 2-RC battery model. SOC estimation comparison based on four KFs will be performed in Section 6.3. A subset of the material shown in this chapter is part of publication [84].

6.2 Equivalent Circuit Battery Model

Based on the previous work [84], in this thesis, the SOC estimation study has been expanded to second-order RC battery model and added JEKF to be compared in terms of accuracy, robustness and computation complexity.

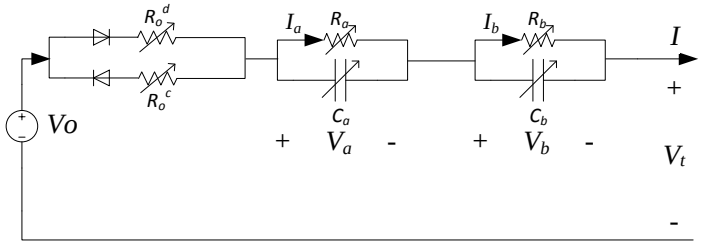

Figure 6.1 Equivalent circuit model of battery with 2 RC pairs

A 2-RC ECM is shown in the Figure 6.1. All the parameters are identified from HPPC fitting tool using the experimental data collected from the 8.8 Ah, 48V Li-Cobalt Electric Bicycle battery pack. The model is current driven and the corresponding terminal voltage can be derived as follows. In continuous time domain:

$$v_t(t) = v_{OC}(z(t)) - i_{R_a}(t) \times R_a - i_{R_b}(t) \times R_b - i(t) \times R_o \tag{6.1}$$

The RC dynamics evolve according to:

$$\frac{di_{Rn}(t)}{dt} = -\frac{1}{C_n R_n} i_{R_n}(t) + \frac{1}{C_n R_n} i(t), n = a, b \tag{6.2}$$

The equation need to be discretized. Therefore, they are converted to discrete time domain by ZOH method:

$$V_t(k) = V_{OC}(z(k)) - i_{R_a}(k) \times R_a - i_{R_b}(k) \times R_b - i(k) \times R_o \tag{6.3}$$

The solution for the discrete-time differential equation (6.2):

$$i_{R_n}(k+1) = e^{\frac{-\Delta t}{R_n \cdot C_n}} \cdot i_{R_n}(k) + (1 - e^{\frac{-\Delta t}{R_n \cdot C_n}}) \cdot i(k), n = a, b \tag{6.4}$$

$$z(k+1) = z(k) - \frac{\eta \cdot \Delta t}{CAP} i(k) \tag{6.5}$$

where $V_{OC}(z(k))$ is the open-circuit-voltage which is a function of the battery SOC $z(k)$, i(k) represents the input current where $(+)$ sign represents discharge and $(-)$ for charge, *CAP* is the nominal capacity, η represents the coulomb efficiency, $V_t(k)$ represents the battery terminal voltage, R_a and R_b represent the polarization resistances, and C_a and C_b indicate the capacitances, [16]. By doing so, the battery model can be simulated in MATLAB. It will be compared with the actual battery response to a certain driving cycle to quantify the fidelity of the fitted parameters and the battery model.

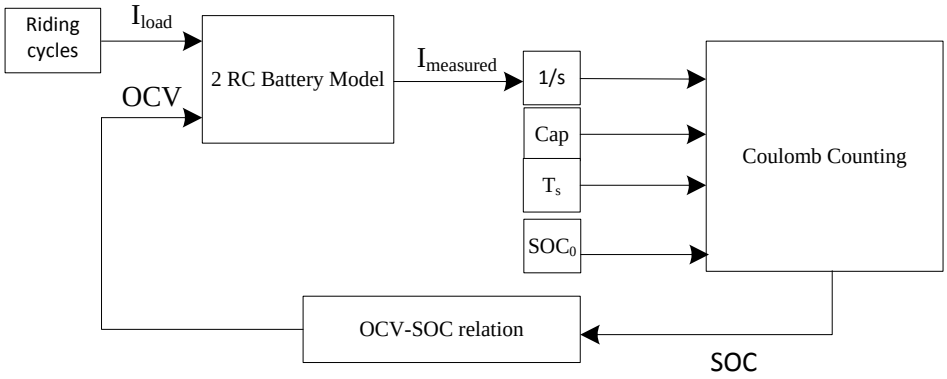

Figure 6.2 2-RC battery model in MATLAB/Simulink

Various variables such as battery current, voltage, and temperatures during charging, discharging, and rest phases are acquired at a maximum frequency of 10 Hz. The battery model has been implemented in MATLAB/Simulink environment as shown in Figure 6.2 below. The battery actual SOC is calculated using coulomb counting. The actual SOC has been used for estimation techniques comparisons. A controlled voltage source is used to simulate the OCV which is function of the battery calculated SOC. A 3D look-up-table with SOC and temperature inputs and OCV output is used in the controlled voltage source.

6.2.1 Experimental Results and Analysis

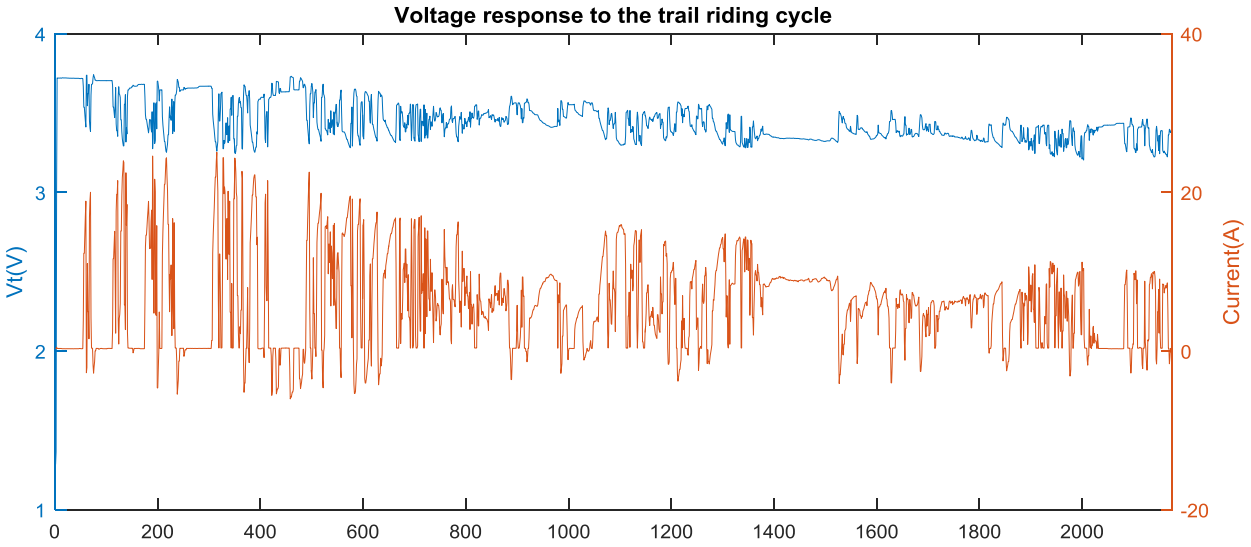

Figure 6.3 Current profile and voltage response to riding cycle

The predefined riding cycles collected from the data acquisition system are used to validate the proposed 2-RC battery model with fitted parameters from HPPC test. The details about riding cycles have been described in Chapter 3. The pack voltage profile has been scaled down to module level while ignoring cell-to-cell balancing and unbalanced cell parameters. The module-level voltage response based on riding cycle and its current load is shown in Figure 6.3. The battery model is driven by the same current profile and its voltage has been recorded. The 20 °C parameters are applied to the battery model since real-life riding is performed at ambient temperature (around 25 °C). The modeled and measured voltage responses are compared in Figure 6.4.

It can be concluded from the Figure 6.4 that the average error is less than 2.5 mV for riding cycles, which is comparable to another modeling study [15]. The max error is around 0.625%, and the average error is 0.06%. In other words, the fitted parameters and the proposed battery

model can present the dynamic behavior of the real battery. The battery model is applied in SOC estimation as estimation benchmarking.

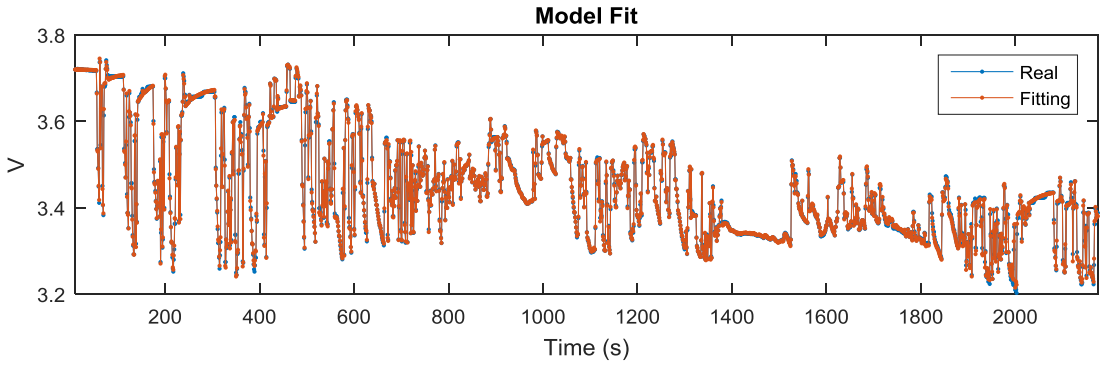

(a)

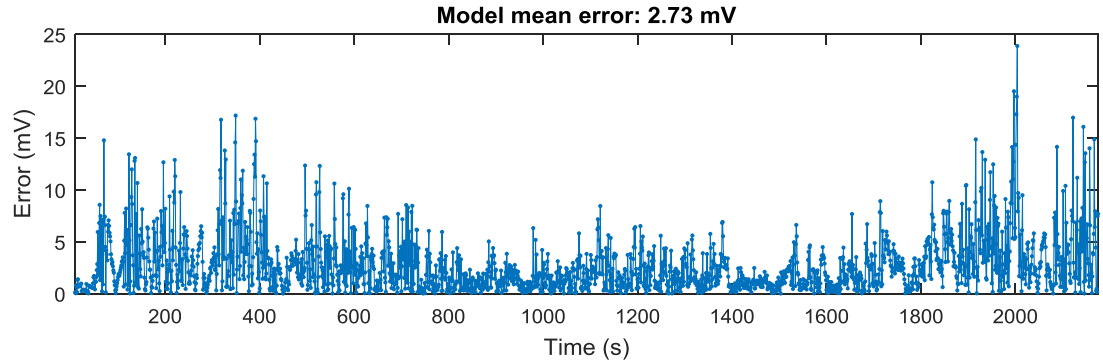

(b)

Figure 6.4 Comparison between actual battery and proposed battery model on terminal voltage based on real-life riding cycle: a) The real and fitted terminal voltage profile, b) fitting error

6.3 Non-Linear Estimation Techniques

6.3.1 Necessary Background of Applied Kalman Filtering Methods

In this section, a summary of estimation strategies that have been used in this thesis are presented. The contribution of this section is to systematically compare SOC based estimation strategies

(EKF, SPKF and CKF) and SOx based estimation (Joint EKF) [84] [86] in terms of SOC accuracy and individual advantages.

The second-order RC equivalent circuit battery model can be represented in state-space representation as follows:

$$\mathbf{x}_{k+1} = f(\mathbf{x}_k, u_k) = \mathbf{A}x_k + \mathbf{B}u_k + w \tag{6.6}$$

$$y_k = g(\mathbf{x}_k, u_k) = OCV(SOC_k) - V_{a,k} - V_{b,k} + Di_k + v \tag{6.7}$$

where,

$$\begin{cases} \mathbf{x}_k = \begin{bmatrix} V_{a,k} & V_{b,k} & SOC_k \end{bmatrix}^T \\ \mathbf{A}_k = \begin{bmatrix} \theta_{a,k} & 0 & 0 \\ 0 & \theta_{b,k} & 0 \\ 0 & 0 & 1 \end{bmatrix} \\ \mathbf{B}_k = \begin{bmatrix} R_{a,k} \cdot (1\text{-}\theta_{a,k}) & R_{b,k} \cdot (1\text{-}\theta_{b,k}) & -\dfrac{T_s}{CAP}\eta \end{bmatrix}^T \\ D_k = -R_0 \\ \theta_{n,k} = \mathrm{e}^{\frac{-T_s}{R_{n,k}C_{n,k}}}, \quad n = a, b \end{cases} \tag{6.8}$$

The input u_k and output y_k are the load current I and terminal voltage V_t, respectively. T_s represents the sampling time, CAP is the capacity of the battery, w and v represents the process and measurement noise which are assumed to be white and Gaussian. The process noise w has a covariance $\mathbf{Q}$ and measurement noise v has a covariance $\mathbf{R}$.

The Extended Kalman Filter

By using first-order Taylor series expansion, the battery model output equation is linearized at each time step k. The linearized matrix **C** is represented as follows, [17]:

$$\mathbf{C} = \left[\left.\frac{\partial g(x(1))}{\partial x(1)}\right|_{x=x_k} \quad \left.\frac{\partial g(x(2))}{\partial x(2)}\right|_{x=x_k} \quad \left.\frac{\partial g(x(3))}{\partial x(3)}\right|_{x=x_k} \right] \tag{6.9}$$

where, $x_k(1)$ and $x_k(2)$ represent the first and second states, i.e. voltage drop across the first and second RC branch $V_{a,k}$ and $V_{b,k}$. Similarly, $x_k(3)$ expresses the state of charge SOC_k. Therefore, the expression of **C** after linearization can be derived as

$$\mathbf{C}_k = [-1 \; -1 \; \frac{dOCV_k}{dSOC_k}] \tag{6.10}$$

Table 6.1: EKF Algorithm

States update
Predict the state based on previous states and input $\hat{\mathbf{x}}_{k+1\|k} = \mathbf{A}\mathbf{x}_k + \mathbf{B}u_k$ Predict the error covariance $\mathbf{P}_{k+1\|k} = \mathbf{A}\mathbf{P}_{k\|k}\mathbf{A}^T + \mathbf{Q}$
Measurement update
Kalman gain $\mathbf{K}_{k+1} = \mathbf{P}_{k+1\|k}\mathbf{C}^T(\mathbf{C}\mathbf{P}_{k+1\|k}\mathbf{C}^T + R)^{-1}$ Correct states according to the measurement $\mathbf{x}_{k+1\|k+1} = \hat{\mathbf{x}}_{k+1\|k} + \mathbf{K}_{k+1}(y_{k+1} - y(\hat{\mathbf{x}}_{k+1\|k}, u_{k+1}))$ Covariance update $\mathbf{P}_{k+1\|k+1} = \mathbf{P}_{k+1\|k} - \mathbf{K}_{k+1}\mathbf{C}\mathbf{P}_{k+1\|k}$

The only difference between EKF and KF appears in obtaining the Jacobian matrix **C**. As a result, equation (6.9) can be substituted to KF algorithm shown in Table 6.1. The EKF is

relatively efficient algorithm and requires small computational power; however, it might suffer from divergence problems due to linearization especially with systems with high level of nonlinearity. The reason leading to this error is, for example,

1) The assumption is $E[f(x)] = f(E[x])$, which is not accurate while f(x) has high level of nonlinearity.
2) The process of linearization needs Taylor-series expansion. However, the higher-ordered nonlinear components are ignored, which results in a loss of accuracy [88].

Sigma-point Kalman Filter

Sigma-point Kalman Filters do not require Taylor-series expansion to approximate the mean and covariance between states. Instead, these mean and covariance have been replaced by a set of points which are called sigma-points. Sigma points are injected into the output function as the mean μ and the covariance Σ. Then the new version of sigma-points are generated which can be treated as the approximation of the posterior mean and covariance. The sigma-points vectors can be represented as follows, [31]:

$$s = \{\mu, \mu + \sqrt{n\sum_i}^T, \mu - \sqrt{n\sum_i}^T\} \tag{6.11}$$

where n denotes the dimension of the state matrix with the mean u and covariance Σ. Note i is the component on i_{th} column. The non-linear function $g(x,u)$ is linearized as, [31]:

$$g(x,u)_{linearized} = \frac{1}{2n+1}\sum_{i=1}^{2n+1} g(s(i)_k, u_k) \tag{6.12}$$

After evaluating equations (6.11) and (6.12), the SPKF algorithm can be derived as shown in Table 6.2.

Table 6.2: SPKF Algorithm

States update

Predict the state based on previous states and input

$$\hat{\mathbf{x}}_{k+1|k} = \mathbf{A}\mathbf{x}_k + \mathbf{B}u_k$$

Predict the error covariance

$$\mathbf{P}_{k+1|k} = \mathbf{A}\mathbf{P}_{k|k}\mathbf{A}^T + \mathbf{Q}$$

Measurement update

$$\mathbf{x}^*_{i,k+1|k} = f(\mathbf{s}_{k|k}(i), u_k)$$

Predicted measurement

$$y_{i,k+1|k} = g(\mathbf{x}^*_{i,k+1|k}, u_{k+1})$$

$$\hat{y}_{k+1|k} = \frac{1}{2n+1}\sum_{i=1}^{2n+1} y_{i,k+1|k}$$

Innovation covariance and the cross covariance matrix

$$\mathbf{P}_{yy,k+1|k} = \frac{1}{2n+1}\sum_{i=1}^{2n+1} y_{i,k+1|k} y^T_{i,k+1|k} - \hat{y}_{k+1|k}\hat{y}^T_{k+1|k} + R$$

$$\mathbf{P}_{xy,k+1|k} = \frac{1}{2n+1}\sum_{i=1}^{2n+1} \mathbf{x}^*_{i,k+1|k} y^T_{i,k+1|k} - \mathbf{x}_{k+1|k}\hat{y}^T_{k+1|k}$$

Kalman gain

$$\mathbf{K}_{k+1} = \mathbf{P}_{xy,k+1|k} P^{-1}_{yy,k+1|k}$$

Correct states according to the measurement

$$\mathbf{x}_{k+1|k+1} = \hat{\mathbf{x}}_{k+1|k} + \mathbf{K}_{k+1}(y_{k+1} - \hat{y}_{k+1|k})$$

Covariance update

$$\mathbf{P}_{k+1|k+1} = \mathbf{P}_{k+1|k} - \mathbf{K}_{k+1}\mathbf{P}_{yy,k+1|k}\mathbf{K}^T_{k+1}$$

where, function *f* and *g* are state function (6.6) and output function (6.7), respectively.

Cubature Kalman Filter

The Cubature Kalman filter has been recently proposed in [32]. Similar to SPKF, it is assumed that the process and the measurement noises are additive Gaussian.

$$p(x_k \mid y_{k-1}) = \int p(x_{k-1} \mid y_{k-1}) p(x_k \mid y_{k-1}) dx_{k-1} \tag{6.13}$$

$$p(x_k \mid y_k) = \frac{p(x_k \mid y_{k-1}) p(y_k \mid x_k)}{\int p(x_k \mid y_{k-1}) p(y_k \mid x_k) dx_k} \tag{6.14}$$

State prediction and measurement update functions represented in (6.13) and (6.14) are derived to multi-dimensional Gaussian-weighted integrals of the form of (6.15). This equation can be computed by the third-degree cubature rule and spherical cubature rule, [19]; this is the reason why the derivative KF is called Cubature Kalman Filter.

$$I(f) = \int_{R^n} f(\mathrm{x})\, \mathrm{e}^{-x^T x}\, dx \tag{6.15}$$

By doing so, a standard Gaussian weighted integral is computed as follows, [20]:

$$I_N(f) = \int_{R^N} f(x) N(x;0,1) dx \approx \sum_{i=1}^{m} \omega_i f(\xi_i) \tag{6.16}$$

where:

$$\begin{aligned} \xi_i &= \sqrt{\frac{m}{2}} [\mathbf{1}]_i \\ [\mathbf{1}] &= \left\{ diag(\underbrace{1 \quad ... \quad 1}_{\text{the number of states}}), diag(\underbrace{-1 \quad ... \quad -1}_{\text{the number of states}}) \right\} \\ \omega_i &= \frac{1}{m}, \quad i = 1, 2, ..., m \end{aligned} \tag{6.17}$$

where m is the twice of the number of states, e.g. m=6 in second-order RC model, since the state vector consists of three elements. Cubature points are calculated as follows:

$$\mathbf{c}_{i,k|k} = \mathbf{S}_{k|k} \xi_i + \mathbf{x}_{k|k} \tag{6.18}$$

where $\mathbf{S}_{k|k}$ is calculated by factorizing $\mathbf{P}_{k|k} = \mathbf{S}_{k|k}\mathbf{S}_{k|k}^T$. The details about CKF algorithms are summarized in Table 6.3.

Table 6.3: CKF Algorithm

States update
Predict the state based on previous states and input $$\hat{\mathbf{x}}_{k+1\|k} = \mathbf{A}\mathbf{x}_k + \mathbf{B}u_k$$ Predict the error covariance $$\mathbf{P}_{k+1\|k} = \mathbf{A}\mathbf{P}_{k\|k}\mathbf{A}^T + \mathbf{Q}$$
Measurement update
$$\mathbf{P}_{k+1\|k} = \mathbf{S}_{k+1\|k}\mathbf{S}_{k+1\|k}^T,\ \mathbf{c}_{i,k+1\|k} = \mathbf{S}_{k+1\|k}\xi_i + \mathbf{x}_{k+1\|k},\ \mathbf{x}_{i,k+1\|k}^* = f(\mathbf{c}_{i,k+1\|k}, u_k)$$ Predicted measurement $$y_{i,k+1\|k} = g(\mathbf{c}_{i,k+1\|k}^*, u_{k+1}),\ \hat{y}_{k+1\|k} = \frac{1}{2n}\sum_{i=1}^{2n} y_{i,k+1\|k}$$ Innovation covariance and the cross covariance matrix $$\mathbf{P}_{yy,k+1\|k} = \frac{1}{2n}\sum_{i=1}^{2n} y_{i,k+1\|k}y_{i,k+1\|k}^T - \hat{y}_{k+1\|k}\hat{y}_{k+1\|k}^T + R,\ \mathbf{P}_{xy,k+1\|k} = \frac{1}{2n}\sum_{i=1}^{2n} \mathbf{x}_{i,k+1\|k}^* y_{i,k+1\|k}^T - \mathbf{x}_{k+1\|k}\hat{y}_{k+1\|k}^T$$ Kalman gain $$\mathbf{K}_{k+1} = \mathbf{P}_{xy,k+1\|k}\mathbf{P}_{yy,k+1\|k}^{-1}$$ Correct states according to the measurement $$\mathbf{x}_{k+1\|k+1} = \hat{\mathbf{x}}_{k+1\|k} + \mathbf{K}_{k+1}(y_{k+1} - \hat{y}_{k+1\|k})$$ Covariance update $$\mathbf{P}_{k+1\|k+1} = \mathbf{P}_{k+1\|k} - \mathbf{K}_{k+1}\mathbf{P}_{yy,k+1\|k}\mathbf{K}_{k+1}^T$$

where, i denotes the i_{th} column of ξ. Function f and g are state function (6.6) and output function (6.7), respectively.

Joint Extended Kalman Filter

Typically Kalman filtering methods estimate system states, however the same algorithm can be used to simultaneously estimate system parameters and state [91]. This approach is commonly called joint estimation. JEKF is a technique that can track parameters of interest based on

traditional EKFs. A related approach is so called dual estimation, e.g. Dual EKFs [41], where two simpler EKFs are run in parallel, one to estimate parameters, the other to estimate states. Although Dual EKF approach is less computationally expensive, estimation performance is generally worse since cross covariances between state and parameters are not used in the estimate update equations.

The first design of JEKF considers OCV-SOC relationship where nonlinearity appears. A homologous current integration multiplied by $dV_{oc}/dSOC$ is applied to calculate the variation on OCV, e.g. as shown in (6.20). Note that the differential $dV_{oc}/dSOC$ is calculated based on a look-up-table to reduce the computation complexity. It leads to the result of transferring nonlinear time varying functions to linear time varying functions. The state vector is shown below:

$$\mathbf{x}_k = [\theta_{a,k}, R_{a,k}, \theta_{b,k}, R_{b,k}, R_{o,k}, V_{oc,k}, V_{a,k}, V_{b,k}, \frac{1}{CAP_k}]^T \tag{6.19}$$

The discrete battery system can be represented as follows.

$$\begin{aligned} V_{n,k} &= \theta V_{n,k-1} + R_{n,k-1}(1-\theta_{n,k-1})I_{k-1}, \quad n = a,b \\ V_{OC,k} &= V_{OC,k-1} - \frac{dV_{OC}}{dSOC}\frac{\Delta t}{CAP} I_{k-1} \\ V_k &= V_{OC,k} - V_{a,k} - V_{b,k} - R_{o,k} I_k \end{aligned} \tag{6.20}$$

However, due to internal impedance's high sensitivity to aging history, the resistances/time constants and capacity are not always constant. The resistances will increase over time, because the SEI layer is thicker with age, which leads to difficulty of transferring electron [92]. The capacity will fade due to improper usage, such as over discharging/charging. As a result, non-updated resistance and capacity will probably lead to inaccuracy of SOC estimation. So it is not

wise to exclude resistance and capacity estimation while estimating SOC. JEKF has the ability to estimate both resistance and capacity.

Jacobian Matrices **A** and **C** for JEKF:

$$\mathbf{A}_k = \begin{bmatrix} 1 & 0 & 0 & 0 & 0 & 0 & 0 & 0 & 0 \\ 0 & 1 & 0 & 0 & 0 & 0 & 0 & 0 & 0 \\ 0 & 0 & 1 & 0 & 0 & 0 & 0 & 0 & 0 \\ 0 & 0 & 0 & 1 & 0 & 0 & 0 & 0 & 0 \\ 0 & 0 & 0 & 0 & 1 & 0 & 0 & 0 & 0 \\ 0 & 0 & 0 & 0 & 0 & 1 & 0 & 0 & -\frac{dV_{OC,k}}{dSOC_k} I_{k-1}\Delta t \\ V_{a,k-1} - R_{a,k-1}I_{k-1} & (1-\theta_{a,k-1})I_{k-1} & 0 & 0 & 0 & 0 & \theta_{a,k-1} & 0 & 0 \\ 0 & 0 & V_{b,k-1} - R_{b,k-1}I_{k-1} & (1-\theta_{b,k-1})I_{k-1} & 0 & 0 & 0 & \theta_{b,k-1} & 0 \\ 0 & 0 & 0 & 0 & 0 & 0 & 0 & 0 & 1 \end{bmatrix} \tag{6.21}$$

$$\mathbf{C}_k = \begin{bmatrix} 0 & 0 & 0 & 0 & -I_k & 1 & -1 & -1 & 0 \end{bmatrix} \tag{6.22}$$

6.3.2 Analytical Comparison among EKF/JEKF, SPKF and CKF

An analytical comparison is performed in [93]. It is briefly explained here so that the experimental results can be compared with the theoretical analysis. Due to the nonlinearity of the relationship between *x* and *y*, the distribution of *y* should be nonlinear even though *x* is assumed as linear based on Gaussian assumptions. The Gaussian distribution of EKF and SPKF output is illustrated in Figure 6.5 as dashed lines on the left hand side after approximation. We can find the bias between the real output and EKF output PDF is quite large from Figure 6.5, so EKF offers relatively low level of estimation accuracy especially when the system is highly nonlinear. It is because the covariance information is not included due to first-order Taylor series expansion. On the other hand, SPKF utilizes a set of Sigma points to approximate the mean and covariance of the nonlinear functions; this improves the robustness of SPKF even the nonlinearity of systems is significant.

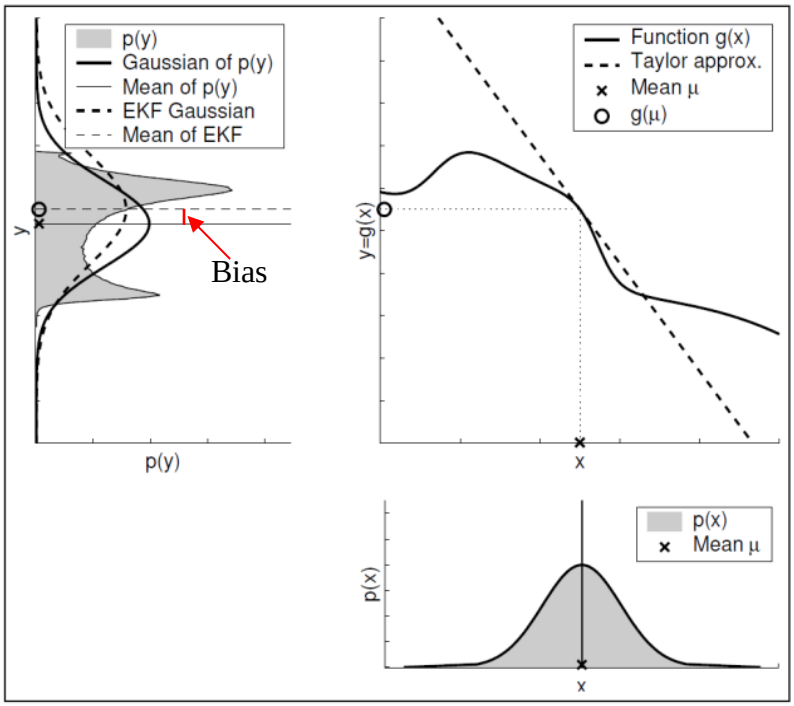

(a)

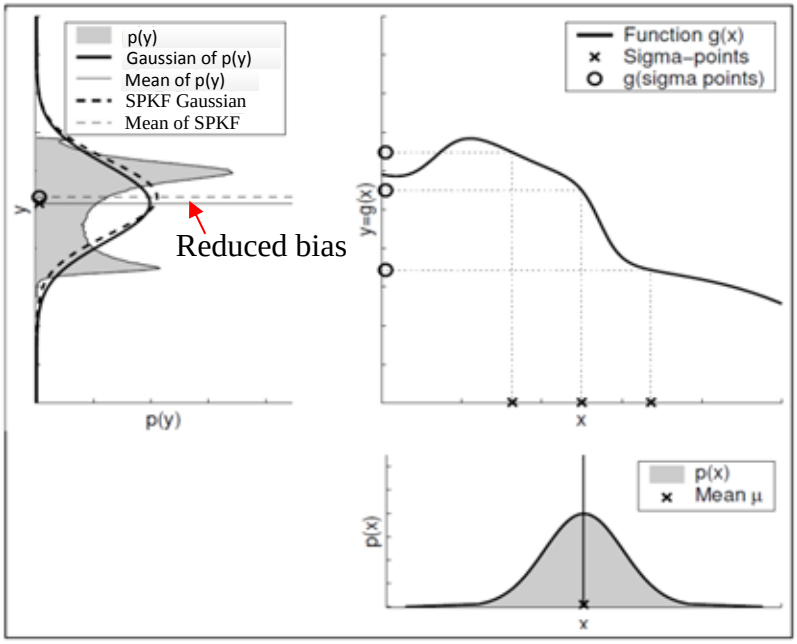

(b)

Figure 6.5 Visual comparison between a) EKF and b) SPKF, 1) the dot lines are the EKF function approximation and output PDF approximations. 2) The solid lines are real input and output PDF. 3) The solid squares are the sigma-points, in addition, the broken line represent SPKF output PDF (adopted from [93])

Similarly, CKF applies Cubature points based on third-order cubature rule to approximate the mean and covariance of nonlinear functions [90]. It improves the robustness of SPKF even the nonlinearity of systems is significant.

Table 6.4: Summary of analytical comparison

	EKF	SPKF	CKF	JEKF
Tunable parameters	P, Q, R	P, Q, R	P, Q, R	P, Q, R
Dimensions of tunable parameters	3, 3, 1	3, 3, 1	3, 3, 1	7,7,1
Additional calculations	Matrix **C**	Sigma points 2n+1	Cubature Points 2n	Matrix **C**
		Innovation covariance and the cross covariance matrix	Innovation covariance and the cross covariance matrix	
		Matrix factorization	Matrix factorization	

A summary of quantified comparison has been given in Table 6.4. The tunable parameters are identical in four methods; however, higher dimension of **P**, **Q** appears so that more tuning work is needed. Since EKF and JEKF have agreement on the basic algorithm, additional calculation is located on the linearized matrix **C** which is the result of first-order Taylor series expansion. Regarding SPKF and CKF, due to their similarity it is not simple to compare them. The detailed comparison between them has been done in [90]. CKF is theoretically more accurate than SPKF. For more detailed discussions on this topic readers are referred to[93].

6.3.3 Estimation Results on Experimental Riding Cycle

A predefined riding cycle (current information) is input to the battery model shown in Figure 6.2. The parameters extracted from 20ºC HPPC test are applied in the battery model. The SOC

generated from the battery model is used as the reference SOC to be compared with estimated SOC profiles. In addition, the voltage and current measurements are recorded and current sensor noise with $N(0, 0.05\ \mathrm{A})$ and voltage sensor noise with $N(0, 2\ \mathrm{mV})$ are introduced to the model. The initial SOC is set to 90%.

The estimated SOC (real SOC_0 = 0.8) with -20% and +10% initial SOC errors is illustrated in Figure 6.6 (a), (b). EKF, SPKF and CKF are compared on the basis of their SOC estimation accuracy, robustness to initial SOC error and computing time. For robustness and convergence analysis, SOC convergence is defined by SOC absolute error converging to 2%. Convergence time and root mean square error (RMSE) can be used to quantify performance of the estimators. Computational complexity of the methods is compared by using functions 'tic' and 'toc' in MATLAB to show calculation time of one script. The test has been carried out by a desktop computer with i5 CPU and 32GB RAM. Results are summarized in Table 6.5.

Table 6.5: Comparison of estimators' performance

	-20% Initial SOC error		**+10% Initial SOC error**		
	Convergence Time (s)	**RMSE %**	**Convergence Time (s)**	**RMSE %**	**Computation Time (s)**
EKF	729	0. 83	2051	1.509	2.28
SPKF	502	0. 73	559	0.0083	3.81
CKF	702	0. 51	816	0. 59	3.7
JEKF	562	0.55	540	0.0061	3.52

Table 6.6: Covariance matrices for EKF, SPKF, CKF and JEKF

	EKF	**SPKF**	**CKF**	**JEKF**
P	Diag([1, 1 ,0.5])	Diag([0.1, 0.1, 0.4])	Diag([1, 1, 0.6])	Diag([1, 1, 1, 1, 1e-3, 1e-1, 1e-4])
Q	Diag([1e-7, 1e-7 ,1e-13])	Diag([1e-11, 1e-11 ,1e-14])	Diag([1e-6, 1e-6 ,1e-14])	Diag([0, 0, 0, 0, 1e-18, 5e-11, 6e-11, 0])
R	1e-5	1e-6	1e-6	1e-8

From the table, it can be noticed that CKF and SPKF have better performance compared to EKF. However, the performance of CKF and SPKF are very close in terms of computational speed and accuracy. According to the theoretical analysis, it is expected to see CKF is more accurate compared with SPKF in every respect. But in RMSE section with -20% initial SOC error, SPKF exceeds CKF in convergence time section. But the RMSE of CKF is still lower than the RMSE of SPKF. It can be explained by the fact that the performance of KF highly depends on tuning Kalman Filters as shown in Table 6.6.

The results shown in Table 6.5 are based on the best tuning by trying multiple combinations of **P**, **Q** and **R** covariances in terms of the robustness, accuracy and convergence. It is not excluded that there are better tuning that will be consistent with the analytical discussion in Section 6.3.2. Nevertheless, the results have represented strong consistency with the theoretical analysis. Based on observations, CKF has better robustness, faster convergence, smaller RMSE and maximum error in most cases.

JEKF is close to SPKF in terms of convergence time and RMSE. However, EKF is better than JEKF considering RMSE. This can be caused by several reasons: 1) the tuning parameters, such as **P**, **Q** and *R*, as described. Tuning is able to strongly affect the performance; 2) since the internal parameters, such as Ohmic resistance and RC pairs, are the elements of JEKF's state

vector, they are estimated. However, the internal parameters are given in a look-up-table for EKF, SPKF and CKF. It is expected that JEKF performs better with battery age.

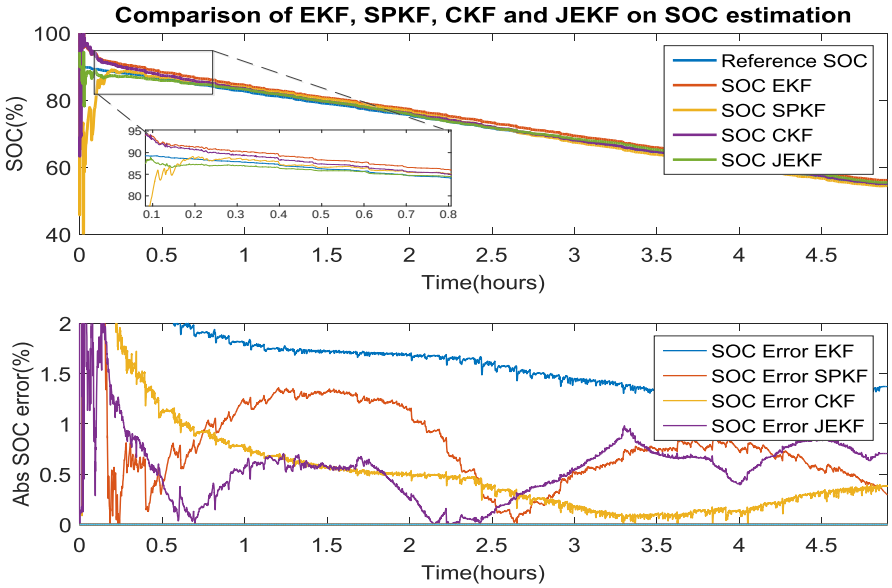

(a)

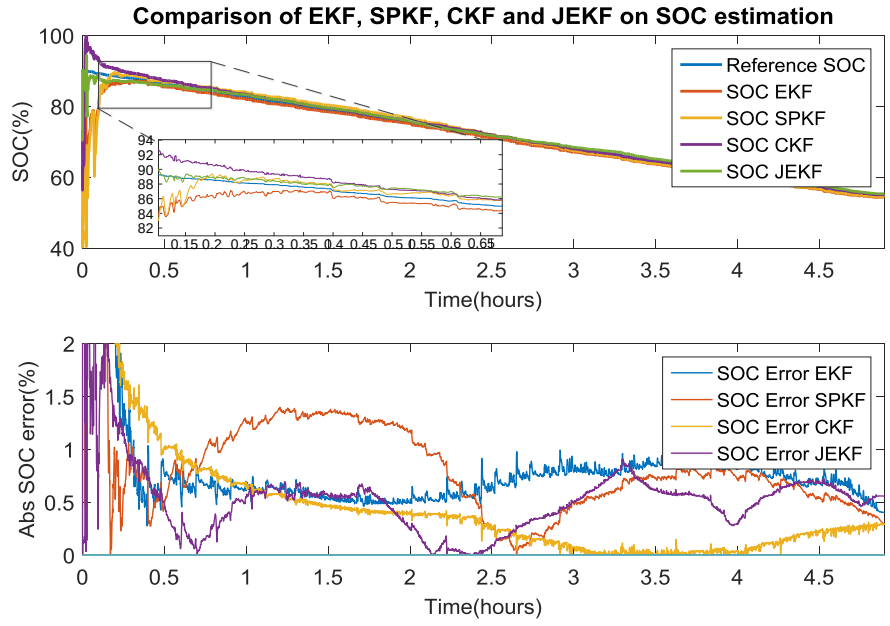

(b)

Figure 6.6 SOC estimation results with (a) +10% initial SOC error, (b) -20% initial SOC error

In this section, the improvement introduced to OCV-SOC relationship is investigated. The derivative is defined as the difference between consecutive SOC points. This method is denoted as ‘difference’ in (6.23). However, derivatives of polynomial function from OCV-SOC (denoted as ‘derivative’) curve shown in (6.23) are used in (6.10) for EKF, SPKF and CKF. The error in ‘derivatives’ origins from a) fitting method (6^{th} order polynomial fitting) generating biased OCV-SOC correlation, b) further error from derivatives of fitted OCV-SOC relationship.

$$\begin{aligned} &\text{'Difference'}: \frac{dV_{oc}}{dSOC} = \frac{\Delta V_{oc}(SOC)}{\Delta SOC} \\ &\text{'Derivative'}: \frac{dV_{oc}}{dSOC} = V_{oc}\text{'}(SOC) = k_1 + k_2 x^1 + \ldots + k_n x^{n-1} \end{aligned} \tag{6.23}$$

A comparison between the two methods to calculate *dVoc/dSOC* is performed. Note that ‘difference’ is approximated as the actual derivative of OCV and SOC, since the true OCV-SOC relationship is used in ‘difference’ method and ΔSOC is small, e.g. equal to 0.05. *dVoc/dSOC* based on these two methods for 20 ºC battery model is shown in Figure 6.7. The improvement of using ‘difference’ method for EKF SOC estimation is depicted in Figure 6.8.

It can be seen from these two figures, the ‘derivative’ method causes up to around 150% bias compared to the reference, which leads to maximum 1% more SOC estimation error. Therefore, ‘difference’ method should replace ‘derivative’ method in BMS SOC estimation for future development.

Additional sensitivity study is conducted to validate the robustness of proposed filtering methods. The white Gaussian noises with standard deviation of 2mV – 6mV and 0.05A – 0.09A represent the voltage measurement noise and current measurement noise. 2mV and 0.05A are extracted from the battery power cycler manual.

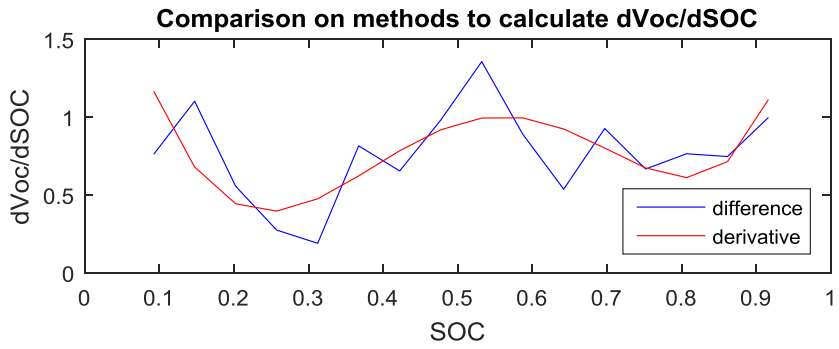

(a)

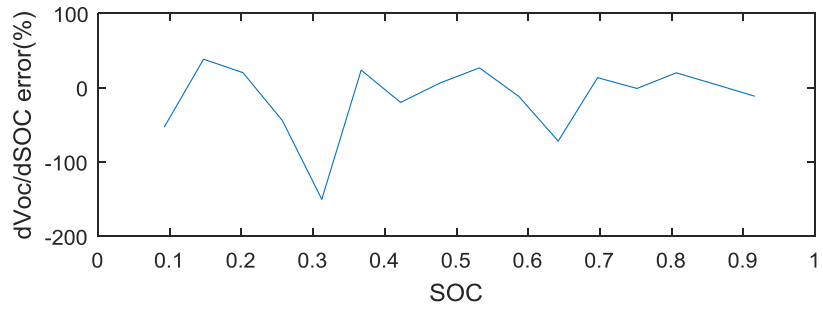

(b)

Figure 6.7 (a) comparison of dVoc/dSOC based on these two methods for 20 ºC battery model, (b) error between the two methods

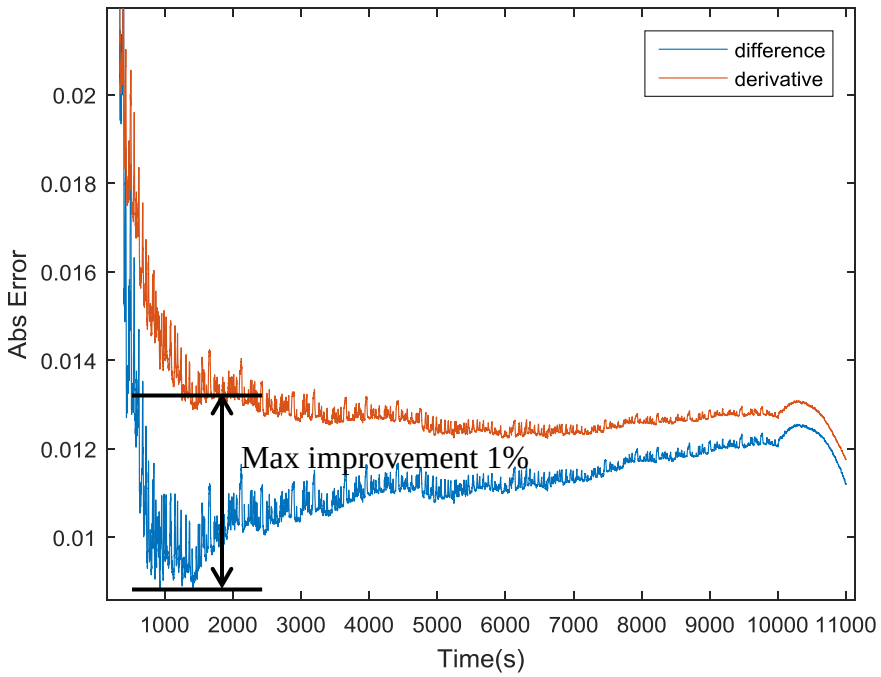

Figure 6.8 Improvement of using 'difference' method to calculate dVoc/dSOC on SOC estimation

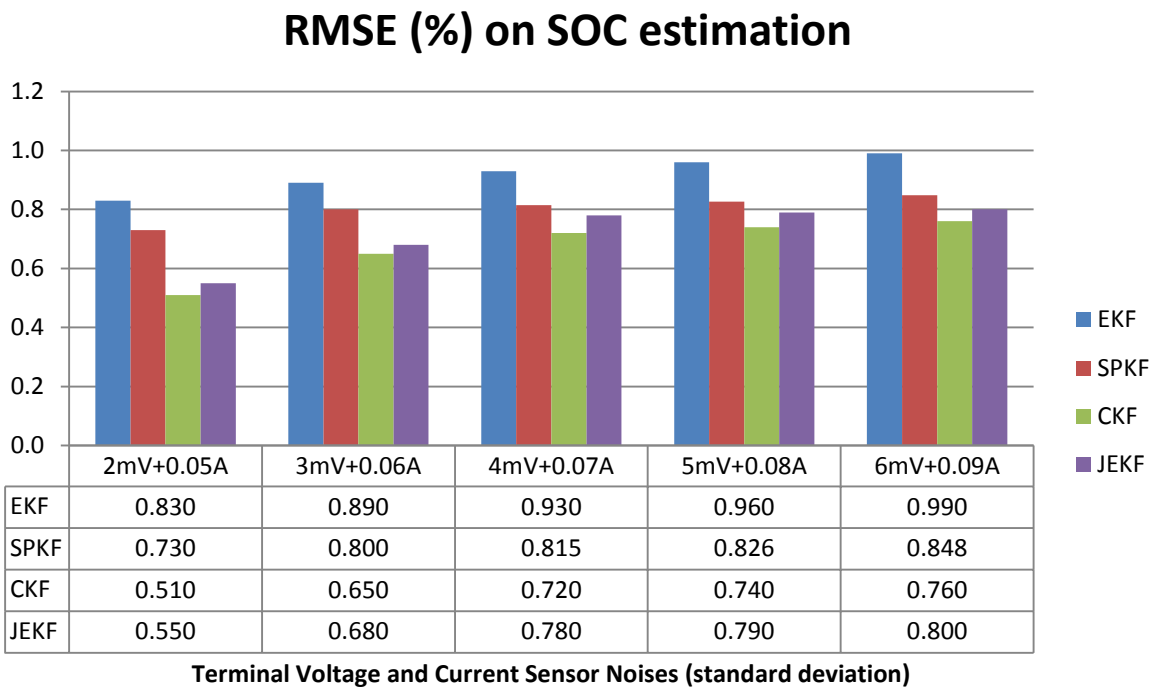

	2mV+0.05A	3mV+0.06A	4mV+0.07A	5mV+0.08A	6mV+0.09A
EKF	0.830	0.890	0.930	0.960	0.990
SPKF	0.730	0.800	0.815	0.826	0.848
CKF	0.510	0.650	0.720	0.740	0.760
JEKF	0.550	0.680	0.780	0.790	0.800

(a)

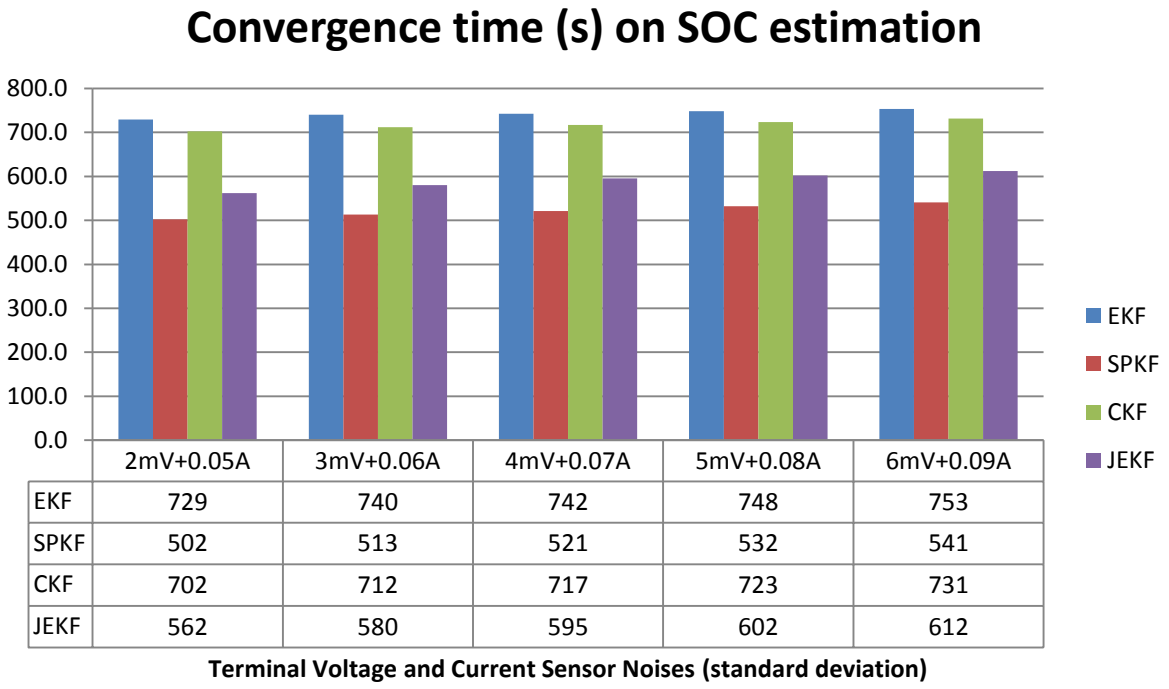

	2mV+0.05A	3mV+0.06A	4mV+0.07A	5mV+0.08A	6mV+0.09A
EKF	729	740	742	748	753
SPKF	502	513	521	532	541
CKF	702	712	717	723	731
JEKF	562	580	595	602	612

(b)

Figure 6.9 Sensitivity study on (a) RMS error and (b) convergence time

Higher levels of noises are for validation purpose under extreme conditions. RMS error, maximum error and convergence time are compared for each circumstance in bar charts Figure 6.9. Although the noises are increasing, the results show excellent robustness under each situation. RMS error is not sensitive to the noises thanks to high robustness of proposed methods. The convergence time slightly increases with noisier inputs for EKF, SPKF and CKF. On the other hand, JEKF is robust to the noises in terms of converging. Note that converging is defined as SOC estimation error drops below 2%. The best tuning parameters for EKF, SPKF, CKF and JEKF are listed in Table 6.6.

6.4 Conclusion

A comparative study among three KF-based battery state-of-charge estimators has been presented in this chapter. The KF-based strategies are the Extended Kalman Filter, the Sigma-Point Kalman Filter, the Cubature Kalman Filter and the joint Extended Kalman Filter. The strategies have been compared based on their estimation accuracy, computational complexity and convergence speed.

The parameters of second-order RC equivalent circuit battery model, such as internal resistance and RC pair impedance which are necessary for the estimators, are extracted based on HPPC experimental data from the BionX Electric Bicycle battery pack. The simulation results show that the EKF and JEKF has demonstrated relatively poor accuracy compared to the SPKF and CKF, however the EKF has shown better computational efficiency. On the contrast, results based on SPKF and CKF are precise (within 1.2% SOC error) but SPKF is time-consuming. The sensitivity study shows all methods are able to converge and maintain high accuracy even when measurement noise is significant. To sum up, if accuracy is the priority, SPKF and CKF are

recommended. But CKF would be the most balanced estimation technique among them according to trade-offs between speed and accuracy. If flexibility and integrity for estimated parameters are of importance, JEKF is recommended. Since only one estimator is need for both SOC and SOH estimation for JEKF instead of two separate estimators for SOC and SOH estimation for EKF/SPKF/CKF.

Chapter 7

CONCLUSION

7.1 Summary

The thesis had presented a comprehensive and systematic analysis and discussion on a battery pack of BionX Electric Bicycle, including parameterization, modeling and benchmarking.

In Chapter 3, the specifications and benchmarking of BionX Electric Bicycle system were described. A data acquisition system that consists of Cycle Analyst and Wahoo speed/cadence Bluetooth sensors was installed on an electrified bicycle via BionX conversion kit. This led to the feasibility of defining standard riding cycles. Two standard riding cycles were defined and applicable for 1) long-range and low traffic riding behavior and 2) urban road conditions with high traffic; this can be further applied to other research areas such as designing battery pack for Electric Bicycle application. Battery life test was performed to determine the average cruise distance per full charge in electric mode. Results showed that around 30 km can be achieved without any pedaling assistance. A threshold of assistance power for efficient and better-user-experience usage was determined to be around 50%.

In Chapter 4, time domain parameter identification and optimization were discussed. A novel QP based fitting algorithm for single and multiple SOC points fitting was proposed. Initialization was not necessary in this approach, so that it avoided the diverged results caused by inaccurate initialization. A test simulator was developed to emulate the current pulses from standard capability tests, such as HPPC and MEP tests; this allowed sensitivity study on fitting algorithms

by adding measurement noise. The sensitivity study on the QP based fitting algorithm showed its high robustness and accuracy compared with 'fmincon' from MATLAB optimization toolbox. The experimental results were fitted, analyzed and applied in Chapter 6 to develop the Electric Bicycle battery model.

In Chapter 5, frequency domain parameter identification and optimization were explained. Another proposed QP based fitting algorithm was developed to fit EIS test data. The sensitivity study also showed the ability to converge. The comparison between HPPC and EIS in terms of internal impedance was performed. Both show high consistency on Ohmic resistance at 20 ºC, but EIS showed insensitivity to temperature when temperature drops. Future work is needed to investigate and validate the reasons.

In Chapter 6, a second-order RC model was developed based on the parameters extracted from HPPC test and validated via pre-defined riding cycles. Four estimators, EKF, SPKF, CKF and JEKF, were used to estimate SOC and compared analytically and experimentally in terms of accuracy and computational complexity. The experimental results showed high consistency of theoretical analysis. In author's opinion, JEKF was the best since it is robust to parameter changing and capacity fading and the SOC estimation accuracy of JEKF is high (1% error).

7.2 Future Work

The following aspects are worthy of future study:

- After real-life aging process, the aging parameters can be extracted from HPPC/EIS test. They can be compared with fresh parameters so that the aging effect can be systematically analyzed.

- Comprehensive comparison between proposed QP fitting algorithm with other methods should be interested.
- The feasibility of online QP based fitting could be investigated, e.g. voltage and current profile is stored within a short period of time, QP could be utilized as a post-processing tool to update known battery parameters.
- The ECMs could be systematically and quantitatively compared in terms of accuracy and robustness.
- More estimation strategies can be included to compare in a comprehensive systematic comparative analysis, such as smooth variable structure filter (SVSF), recursive least squares, and on-line QP-based estimation.
- The different estimators for state of health estimation, including impedance and capacity estimation, and state of power estimation can be also investigated.
- Extensive human factors studies involving riders to quantify and explore usage styles and riding cycles.
- Electric bicycle benchmarking using robust assistance with alternative architectures, motors, energy storage systems, and additional instrumentation, e.g. pedal force sensors, power and efficiency measurements.

REFERENCES

[1] A. Emadi (Editor), *Advanced Electric Drive Vehicles*. CRC Press, 2014.

[2] B. Bilgin, P. Magne, P. Malysz, Y. Yang, V. Pantelic, M. Preindl, A. Korobkine, W. Jiang, S. Member, M. Lawford, S. Member, and A. Emadi, "Making the Case for Electrified Transportation," *IEEE Trans. Transp. Electrif.*, vol. 1, no. 1, pp. 4–17, 2015.

[3] S. M. Lukic and A. Emadi, "Charging ahead," *IEEE Ind. Electron. Mag.*, vol. 2, no. 4, pp. 22–31, 2008.

[4] J. Cao and A. Emadi, "Batteries need electronics," *Ind. Electron. Mag. IEEE*, vol. 5, no. 1, pp. 27–35, 2011.

[5] A. Emadi, "Transportation 2.0," *Power Energy Mag. IEEE*, vol. 9, no. 4, pp. 18–29, 2011.

[6] "Navigant Research." [Online]. Available: https://www.navigantresearch.com/.

[7] D. Fregosi, S. Bhattacharya, and S. Atcitty, "Empirical battery model characterizing a utility-scale carbon-enhanced VRLA battery," *2011 IEEE Energy Convers. Congr. Expo.*, pp. 3541–3548, 2011.

[8] X. Hu, S. Li, and H. Peng, "A comparative study of equivalent circuit models for Li-ion batteries," *J. Power Sources*, vol. 198, pp. 359–367, 2012.

[9] K. a. Smith, C. D. Rahn, and C. Y. Wang, "Model-based electrochemical estimation of lithium-ion batteries," *Proc. IEEE Int. Conf. Control Appl.*, no. 1, pp. 714–719, 2008.

[10] R. Ahmed, M. El Sayed, I. Arasaratnam, J. Tjong, and S. Habibi, "Reduced-Order Electrochemical Model Parameters Identification and SOC Estimation for Healthy and Aged Li-Ion Batteries. Part I: Parameterization Model Development for Healthy Batteryies," *IEEE J. Emerg. Sel. Top. Power Electron.*, vol. 2, no. 3, pp. 659–677, 2014.

[11] C. Speltino, "Experimental validation of a lithium-ion battery state of charge estimation with an extended kalman filter," *Control Conf. (ECC), 2009 Eur. Budapest*, pp. 4828–4833, 2009.

[12] C. Speltino, D. Di Domenico, G. Fiengo, and a. Stefanopoulou, "Comparison of reduced order lithium-ion battery models for control applications," *Proc. 48h IEEE Conf. Decis. Control held jointly with 2009 28th Chinese Control Conf.*, pp. 3276–3281, 2009.

[13] R. Gu, P. Malysz, H. Yang, and A. Emadi, "On the Suitability of Electrochemical-Based Modeling for Lithium-ion Batteries," *IEEE Trans. Transp. Electrif.*, vol. 7782, no. c, pp. 1–1, 2016.

[14] M. Chen and G. a. Rincón-Mora, "Accurate electrical battery model capable of predicting runtime and I-V performance," *IEEE Trans. Energy Convers.*, vol. 21, no. 2, pp. 504–511, 2006.

[15] R. Xiong, H. He, H. Guo, and Y. Ding, "Modeling for lithium-ion battery used in electric vehicles," *Procedia Eng.*, vol. 15, no. 1, pp. 2869–2874, 2011.

[16] P. Malysz, L. Gauchia, and H. Yang, "Fundamentals of Electric Energy Storage Systems," *Adv. Electr. Drive Veh.*, pp. 237–281, 2014.

[17] B. Y. Liaw, G. Nagasubramanian, R. G. Jungst, and D. H. Doughty, "Modeling of lithium ion cells - A simple equivalent-circuit model approach," *Solid State Ionics*, vol. 175, no. 1–4, pp. 835–839, 2004.

[18] N. Lin, S. Ci, and H. Li, "An enhanced circuit-based battery model with considerations of temperature effect," *2014 IEEE Energy Convers. Congr. Expo. ECCE 2014*, pp. 3985–3989, 2014.

[19] G. Liu, L. Lu, H. Fu, J. Hua, J. Li, M. Ouyang, and Y. Wang, "A comparative study of equivalent circuit models and enhanced equivalent circuit models of lithium-ion batteries with different model structures," pp. 1–6, 2014.

[20] M. Bahramipanah, D. Torregrossa, R. Cherkaoui, and M. Paolone, "Enhanced electrical model of Lithium-based batteries accounting the charge redistribution effect," *Proc. - 2014 Power Syst. Comput. Conf. PSCC 2014*, 2014.

[21] M. a. Roscher, O. Bohlen, and J. Vetter, "OCV Hysteresis in Li-Ion Batteries including Two-Phase Transition Materials," *Int. J. Electrochem.*, vol. 2011, pp. 1–6, 2011.

[22] H. Rahimi Eichi and M. Y. Chow, "Modeling and analysis of battery hysteresis effects," *2012 IEEE Energy Convers. Congr. Expo. ECCE 2012*, pp. 4479–4486, 2012.

[23] B. Pattipati, C. Sankavaram, and K. R. Pattipati, "System identification and estimation framework for pivotal automotive battery management system characteristics," *IEEE Trans. Syst. Man Cybern. Part C Appl. Rev.*, vol. 41, no. 6, pp. 869–884, 2011.

[24] E. Chemali, M. Peindl, P. Malysz, and A. Emadi, "Electrochemical and Electrostatic

Energy Storage and Management Systems for Electric Drive Vehicles: State-of-the-Art Review and Future Trends," *IEEE J. Emerg. Sel. Top. Power Electron.*, vol. 6777, no. c, pp. 1–1, 2016.

[25] H. He, X. Zhang, R. Xiong, Y. Xu, and H. Guo, "Online model-based estimation of state-of-charge and open-circuit voltage of lithium-ion batteries in electric vehicles," *Energy*, vol. 39, no. 1, pp. 310–318, 2012.

[26] K. S. Ng, C. S. Moo, Y. P. Chen, and Y. C. Hsieh, "Enhanced coulomb counting method for estimating state-of-charge and state-of-health of lithium-ion batteries," *Appl. Energy*, vol. 86, no. 9, pp. 1506–1511, 2009.

[27] W. Waag, C. Fleischer, and D. U. Sauer, "Critical review of the methods for monitoring of lithium-ion batteries in electric and hybrid vehicles," *J. Power Sources*, vol. 258, pp. 321–339, 2014.

[28] S. Lee, J. Kim, J. Lee, and B. H. Cho, "State-of-charge and capacity estimation of lithium-ion battery using a new open-circuit voltage versus state-of-charge," *J. Power Sources*, vol. 185, pp. 1367–1373, 2008.

[29] L. W. Juang, "Online Battery Monitoring for State-of-Charge and Power Capability Prediction by University of Wisconsin – Madison O nline Battery Monitoring for State-of-Charge and Power Capability Prediction by," 2010.

[30] I. Kim, "Nonlinear State of Charge Estimator for Hybrid Electric Vehicle Battery," *IEEE Trans. Power Electron.*, vol. 23, no. 4, pp. 2027–2034, 2008.

[31] G. L. Plett, “Sigma-point Kalman filtering for battery management systems of LiPB-based HEV battery packs. Part 2: Simultaneous state and parameter estimation,” *J. Power Sources*, vol. 161, no. 2, pp. 1369–1384, 2006.

[32] I. Arasaratnam and S. Haykin, “Cubature kalman filters,” *Autom. Control. IEEE Trans. …*, no. 7, pp. 1–16, 2009.

[33] D. Sun and X. Chen, “Adaptive parameter identification method and state of charge estimation of Lithium Ion battery,” *Electr. Mach. Syst. (ICEMS), 2014 17th Int. Conf.*, pp. 855–860, 2014.

[34] S. Habibi, “The smooth variable structure filter,” *Proc. IEEE*, vol. 95, no. 5, pp. 1026–1059, 2007.

[35] D. Di Domenico, G. Fiengo, and A. Stefanopoulou, “Lithium-ion battery state of charge estimation with a Kalman Filter based on a electrochemical model,” *Control Appl. 2008. CCA 2008. IEEE Int. Conf.*, pp. 702–707, 2008.

[36] A. Hammouche, E. Karden, and R. W. De Doncker, “Monitoring state-of-charge of Ni–MH and Ni–Cd batteries using impedance spectroscopy,” *J. Power Sources*, vol. 127, no. 1–2, pp. 105–111, Mar. 2004.

[37] W. Choi and J. Lee, “Development of the low-cost impedance spectroscopy system for modeling the electrochemical power sources,” in *7th Internatonal Conference on Power Electronics, ICPE’07*, 2008, pp. 113–118.

[38] S. Rodrigues, N. Munichandraiah, and A. K. Shukla, “AC impedance and state-of-charge

analysis of a sealed lithium-ion rechargeable battery," *Journal of Solid State Electrochemistry*, vol. 3. pp. 397–405, 1999.

[39] J. Lee and W. Choi, "Novel State-of-Charge Estimation Method for Lithium Polymer Batteries Using Electrochemical Impedance Spectroscopy," *J. Power Electron.*, pp. 237–243, 2011.

[40] G. L. Plett, "Extended Kalman filtering for battery management systems of LiPB-based HEV battery packs. Part 2: Modeling and identification," *J. Power Sources*, vol. 134, pp. 262–276, 2004.

[41] G. Plett, "Dual and Joint EKF for Simultaneous SOC and SOH Estimation," *Proc. 21st Electr. Veh. Symp. (EVS21), Monaco*, pp. 1–12, 2005.

[42] C. Hu, B. D. Youn, and J. Chung, "A multiscale framework with extended Kalman filter for lithium-ion battery SOC and capacity estimation," *Appl. Energy*, vol. 92, pp. 694–704, 2012.

[43] P. Malysz, R. Gu, J. Ye, H. Yang, and A. Emadi, "State-of-charge and state-of-health estimation with state constraints and current sensor bias correction for electrified powertrain vehicle batteries," *IET Electr. Syst. Transp.*, vol. 6 (2), pp. 136–144, 2016.

[44] J. Vetter, P. Novák, M. R. Wagner, C. Veit, K. C. Möller, J. O. Besenhard, M. Winter, M. Wohlfahrt-Mehrens, C. Vogler, and a. Hammouche, "Ageing mechanisms in lithium-ion batteries," *J. Power Sources*, vol. 147, pp. 269–281, 2005.

[45] H. Wang, L. He, J. Sun, S. Liu, and F. Wu, "Study on correlation with SOH and EIS

model of Li-ion battery," in *Proceedings of the 6th International Forum on Strategic Technology, IFOST 2011*, 2011, vol. 1, pp. 261–264.

[46] J. P. Christophersen, J. Morrison, W. Morrison, and C. Motloch, "Rapid Impedance Spectrum Measurements for State-of-Health Assessment of Energy Storage Devices," pp. 246–256, 2012.

[47] W. Waag, S. Käbitz, and D. U. Sauer, "Experimental investigation of the lithium-ion battery impedance characteristic at various conditions and aging states and its influence on the application," *Appl. Energy*, vol. 102, pp. 885–897, 2013.

[48] D. V. Do, C. Forgez, K. El Kadri Benkara, and G. Friedrich, "Impedance observer for a Li-ion battery using Kalman filter," *IEEE Trans. Veh. Technol.*, vol. 58, no. 8, pp. 3930–3937, 2009.

[49] G. S. Popkirov and R. N. Schindler, "A new impedance spectrometer for the investigation of electrochemical systems," *Rev. Sci. Instrum.*, vol. 63, no. 11, pp. 5366–5372, 1992.

[50] J. Schoukens, R. Pintelon, E. van der Ouderaa, and J. Renneboog, "Survey of excitation signals for FFT based signal analyzers.," *IEEE Trans. Instrum. Meas.*, vol. 37, no. 3, pp. 342–352, 1988.

[51] E. Barsoukov and J. R. Macdonald, *Impedance Spectroscopy*. 2005.

[52] H. Zhang and M. Y. Chow, "Comprehensive dynamic battery modeling for PHEV applications," *2010 IEEE Power Energy Soc. Gen. Meet.*, pp. 1–6, 2010.

[53] Y. Hu, S. Yurkovich, Y. Guezennec, and B. J. Yurkovich, "A technique for dynamic

battery model identification in automotive applications using linear parameter varying structures," *Control Eng. Pract.*, vol. 17, no. 10, pp. 1190–1201, 2009.

[54] D. I. Stroe, M. Swierczynski, A. I. Stan, V. Knap, R. Teodorescu, and S. J. Andreasen, "Diagnosis of Lithium-Ion Batteries State-of-Health based on Electrochemical Impedance Spectroscopy Technique," pp. 4576–4582, 2014.

[55] H. Wang, G. Li, Z. Yu, and X. Wang, "Study on Genetic Algorithm in Estimating the Initial Value of EIS Equivalent Circuit," *2009 WRI World Congr. Softw. Eng.*, pp. 507–510, 2009.

[56] P. a Lindahl, M. a Cornachione, and S. R. Shaw, "A Time-Domain Least Squares Approach to Electrochemical Impedance Spectroscopy," *Ieee Trans. Instrum. Meas.*, vol. 61, no. 12, pp. 3303–3311, 2012.

[57] H. Wang, K. Dong, G. Li, and F. Wu, "Research on the consistency of the power battery based on multi-points impedance spectrum," *2010 Int. Forum Strateg. Technol. IFOST 2010*, pp. 1–4, 2010.

[58] P.-C. Wu, W.-C. Hsu, and J.-F. Chen, "Detection on SOC of VRLA battery with EIS," *2013 1st Int. Futur. Energy Electron. Conf.*, pp. 897–902, 2013.

[59] Z. Chen, C. C. Mi, Y. Fu, J. Xu, and X. Gong, "Online battery state of health estimation based on Genetic Algorithm for electric and hybrid vehicle applications," *J. Power Sources*, vol. 240, pp. 184–192, 2013.

[60] W. Wang, P. Malysz, K. Khan, L. Gauchia, and A. Emadi, "Modeling , Parameterization ,

and Benchmarking of a Lithium Ion Electric Bicycle Battery," in *to be presented at IEEE Energy Conversion Congress & Exposition (ECCE)*, 2016, pp. 1–7.

[61] The Idaho National Laboratory, "Battery Test Manual For Electric Vehicles," no. June, 2015.

[62] G. L. Plett, "Recursive approximate weighted total least squares estimation of battery cell total capacity," *J. Power Sources*, vol. 196, no. 4, pp. 2319–2331, Feb. 2011.

[63] A. A. Hussein, "Experimental modeling and analysis of lithium-ion battery temperature dependence," *2015 IEEE Appl. Power Electron. Conf. Expo.*, pp. 1084–1088, 2015.

[64] A. Cordoba-Arenas, S. Onori, Y. Guezennec, and G. Rizzoni, "Capacity and power fade cycle-life model for plug-in hybrid electric vehicle lithium-ion battery cells containing blended spinel and layered-oxide positive electrodes," *J. Power Sources*, vol. 278, pp. 473–483, 2015.

[65] R. Xiong, H. He, H. Guo, and Y. Ding, "Modeling for Lithium-Ion Battery used in Electric Vehicles," *Procedia Eng.*, vol. 15, pp. 2869–2874, 2011.

[66] H. He, R. Xiong, H. Guo, and S. Li, "Comparison study on the battery models used for the energy management of batteries in electric vehicles," *Energy Convers. Manag.*, vol. 64, pp. 113–121, 2012.

[67] Z. He, M. Gao, J. Xu, and Y. Liu, "Battery model parameters estimation with the sigma point Kalman filter," in *2009 International Conference on Artificial Intelligence and Computational Intelligence, AICI 2009*, 2009, vol. 3, pp. 303–306.

[68] A. Hentunen, T. Lehmuspelto, and J. Suomela, "Time-domain parameter extraction method for th??venin-equivalent circuit battery models," *IEEE Trans. Energy Convers.*, vol. 29, no. 3, pp. 558–566, 2014.

[69] P. Malysz, J. Ye, R. Gu, H. Yang, and A. Emadi, "Battery State-of-Power Peak Current Calculation and Verification using an Asymmetric Parameter Equivalent Circuit Model," *IEEE Trans. Veh. Technol.*, vol. 9545, no. c, pp. 1–1, 2015.

[70] X. Feng and Z. Sun, "A battery model including hysteresis for state-of-charge estimation in Ni-MH battery," *2008 IEEE Veh. Power Propuls. Conf. VPPC 2008*, no. dc, pp. 3–7, 2008.

[71] S. Bangaru, R. Alugonda, and P. Palacharla, "Modeling and simulation of lithium-ion battery with hysteresis for industrial applications," *2013 Int. Conf. Energy Effic. Technol. Sustain. ICEETS 2013*, pp. 771–775, 2013.

[72] S. Qiu, Z. Chen, M. a Masrur, and Y. L. Murphey, "Battery hysteresis modeling for state of charge estimation based on Extended Kalman Filter," *Ind. Electron. Appl. (ICIEA), 2011 6th IEEE Conf.*, pp. 184–189, 2011.

[73] H. Zhang and M. Y. Chow, "On-line PHEV battery hysteresis effect dynamics modeling," *IECON Proc. (Industrial Electron. Conf.*, pp. 1844–1849, 2010.

[74] C. D. Rahn, *Battery systems engineering*. 2013.

[75] E. Karden, "Using low-frequency impedance spectroscopy for characterization , monitoring , and modeling of Industrial batteries," no. May, 2001.

[76] G. Liu, M. Ouyang, L. Lu, L. Xu, and J. Li, "Online monitoring of lithium-ion battery aging effects by internal resistance estimation in electric vehicles," *Control Conf. (CCC), ...*, pp. 6851–6855, 2012.

[77] B. Savova-Stoynov and Z. B. Stoynov, "Analysis of the inductance influence on the measured electrochemical impedance," *J. Appl. Electrochem.*, vol. 17, no. 6, pp. 1150–1158, 1987.

[78] K. S. Cole and R. H. Cole, "Dispersion and Absorption in Dielectrics I. Alternating Current Characteristics," *J. Chem. Phys.*, vol. 9, no. 4, p. 341, 1941.

[79] D. Andre, M. Meiler, K. Steiner, H. Walz, T. Soczka-Guth, and D. U. Sauer, "Characterization of high-power lithium-ion batteries by electrochemical impedance spectroscopy. II: Modelling," *J. Power Sources*, vol. 196, no. 12, pp. 5349–5356, 2011.

[80] D. Andre, M. Meiler, K. Steiner, C. Wimmer, T. Soczka-Guth, and D. U. Sauer, "Characterization of high-power lithium-ion batteries by electrochemical impedance spectroscopy. I. Experimental investigation," *J. Power Sources*, vol. 196, no. 12, pp. 5334–5341, 2011.

[81] L. W. Juang, P. J. Kollmeyer, T. M. Jahns, and R. D. Lorenz, "The Impact of DC Bias Current on the Modeling of Lithium Iron Phosphate and Lead-Acid Batteries Observed using Electrochemical Impedance Spectroscopy," pp. 2575–2581, 2014.

[82] L. W. J. Uang, "Improved Modeling of Lithium-Based Batteries using Temperature-Dependent Resistance and Overpotential."

[83] J. P. Schmidt, S. Arnold, A. Loges, D. Werner, T. Wetzel, and E. Ivers-Tiffée, "Measurement of the internal cell temperature via impedance: Evaluation and application of a new method," *J. Power Sources*, vol. 243, pp. 110–117, 2013.

[84] W. Wang, D. Wang, X. Wang, T. Li, R. Ahmed, S. Habibi, and A. Emadi, "Comparison of Kalman Filter-based State of Charge Estimation Strategies for Li-Ion Batteries," in *in the proc. IEEE Transportation Electrification Conference and Expo (ITEC), 2016 IEEE, Dearborn, MI*, 2016, pp. 1–6.

[85] M. Petzl and M. A. Danzer, "Advancements in OCV Measurement and Analysis for Lithium-Ion Batteries," vol. 28, no. 3, pp. 675–681, 2013.

[86] W. Wang, J. Ye, P. Malysz, H. Yang, and A. Emadi, "Sensitivity Analysis of Kalman filter Based Capacity Estimation for Electric Vehicles," in *IEEE Transportation Electrification Conference*, 2015, pp. 1–7.

[87] G. L. Plett, "Extended kalman filtering for battery management systems of lipb-based hev battery packs: Part 3. state and parameter estimation," *J. Power Sources*, vol. 134, no. 2, pp. 272–292, 2004.

[88] G. L. Plett, "Sigma-point Kalman filtering for battery management systems of LiPB-based HEV battery packs. Part 1: Introduction and state estimation," *J. Power Sources*, vol. 161, pp. 1356–1368, 2006.

[89] V. P. Bhuvana, C. Unterrieder, E. Christophunterriederaauat, and M. Huemer, "Battery Internal State Estimation : A Comparative Study of Non-Linear State Estimation Algorithms," 2013.

[90] I. Arasaratnam and S. Haykin, "Cubature Kalman smoothers," *Automatica*, vol. 47, no. 10, pp. 2245–2250, 2011.

[91] W. Wang, P. Malysz, D. Wang, R. Gu, H. Yang, A. E. Electrical, M. Automotive, and R. Centre, "Efficient Multi-cell SOC Estimation for Electrified Vehicle Battery Packs," *2016 IEEE Transportation Electrification Conference and Expo (ITEC)*, Dearborn, MI, USA, 2016, pp. 1-6.

[92] A. Christensen and A. Adebusuyi, "Using on-board Electrochemical Impedance Spectroscopy in Battery Management Systems," vol. i, pp. 1–7, 2013.

[93] S. Thrun, "Probabilistic robotics," *Commun. ACM*, vol. 45, no. 3, pp. 1999–2000, 2002.

APPENDIX

A.1 Capacity Test Procedures

The following variables are of interest and should be recorded during test: Voltage, Current, Time and Temperature.

Data should be recorded at a sampling rate of 10 second (0.1 Hz) during bulk charge/charge and rest; rest periods of one hour or longer are required. Data is recorded at a rate of 0.1 second (10 Hz) for charge and discharge test pulses of 10 seconds and one-minute rest period.

This test is the very first test before any further experiments (HPPC, MEP). The steps are as follows:

1) Rest the cell at 25°C. (2 hrs)
2) Charge the cell at C/3 rate until voltage V=Vmax. (maximum 3 hrs, depends on the initial SOC)
3) Keep voltage V=Vmax and reduce the charge current until current I=C/200.(depends on the chemistry, should be less than 30 mins)
4) Rest for 2 hours.
5) Set temperature chamber to the test temperature of 25˚C.
6) Rest for 2 hours.
7) Discharge the cell at C/3 rate until voltage V=Vmin.(3 hrs)
8) Keep voltage at V=Vmin and reduce the discharge current until current I=C/200.(depends on the chemistry, should be less than 30 mins)

9) Rest for 2 hours.
10) Repeat steps 1 to 9 for two more times.
11) Perform the above steps one time each at other test temperatures of -10ºC, 25ºC.
12) The total chargeable or dischargeable capacity would be the integrated current over the whole time interval. Record the capacity at each temperature.

A.2 HPPC Test Procedures

The same measurements and sampling rates for capacity tests are used for HPPC. The capacity is assumed as 2150mAh at beginning of life (BOL). The maximum charging/discharging current is 1 C-rate (2150mA).

HPPC test is using the results of the capacity test to determine SOC points. The procedure is performed with the following steps:

A.2.1 HPPC Discharging Test (Estimated time: 36 hrs)

1) Rest the cell at 25°C a night before the test.
2) Charge the cell at C/3 rate until voltage V=Vmax. (3 hrs)
3) Keep voltage at V=Vmax and reduce the charge current till current I=C/200. (depends on the chemistry, should be less than 30 mins)

   Note: This charging part can be alternatively finalized by the original charger from manufacturer, same as the charging phase in the future.
4) Rest for 2 hours.
5) Discharge at C/3 rate until 5% of the measured capacity in ampere-hour (Ah) from the capacity test is removed. The new SOC is at 95%.(3 hrs/20 = 9 mins)
6) Rest for 1 hour.

7) EIS test at this SOC level 95%. (20 mins)
8) Discharge at the maximum current limit rate (1C) for 10 seconds and rest for 1 minute and charge at 75% of the maximum current limit rate (1C) for 10 seconds and rest for 1 minute.(2.3 mins)
9) Discharge at C/3 rate until 5% of the measured Ah from the capacity test is removed. The new SOC is at 90%. (9 mins)
10) Rest for 1 hour. EIS test at this SOC level 90%.
11) Discharge at the maximum current limit rate for 10 seconds and rest for 1 minute and charge at 75% of the maximum current limit rate for 10 seconds and rest for 1 minute.
12) Discharge at C/3 rate until 10% of the measured Ah from the capacity test is removed. The new SOC is at 80%.
13) Rest for 1 hour.
14) Repeat the steps from 11 to 14 from 80% SOC to 10% SOC at 10% interval.....
15) EIS test at this SOC level 10%.
16) Discharge at the maximum current limit rate for 10 seconds and rest for 1 minute and charge at 75% of the maximum current limit rate for 10 seconds and rest for 1 minute.
17) Discharge at C/3 rate until 5% of the measured Ah from the capacity test is removed. The new SOC is at 5%.
18) Rest for 1 hour.
19) EIS test at this SOC level 5%.
20) Discharge at the maximum current limit rate for 10 seconds and rest for 1 minute and charge at 75% of the maximum current limit rate for 10 seconds and rest for 1 minute. (5-21: 19* 1.5 hrs = 29 hrs)

21) Discharge at C/3 rate until the cell voltage reaches to voltage V=Vmin and then discharge at a constant voltage v=Vmin until current decreases to C/200 rate. The new SOC is at about 0%. (9 mins)

22) Rest for 2 hours.

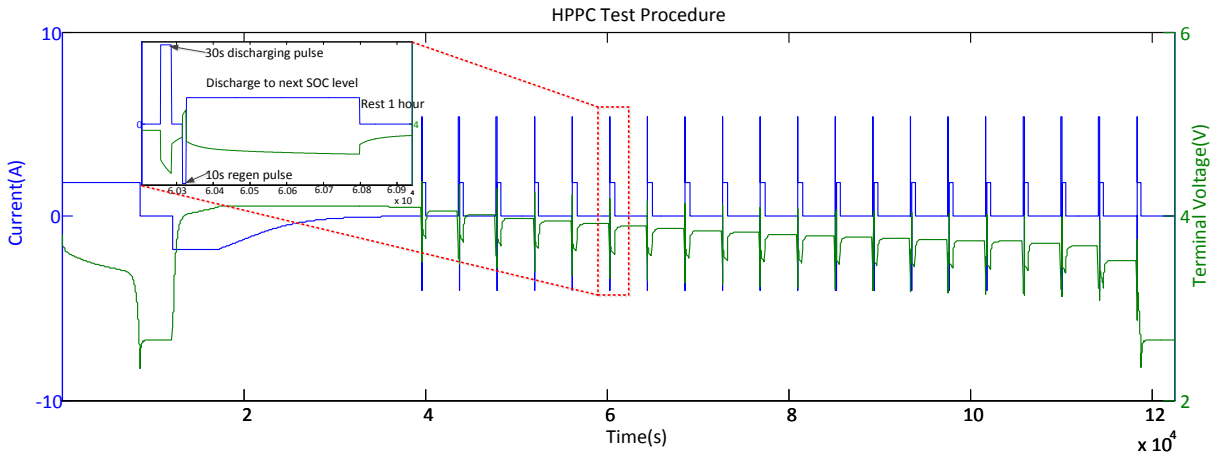

Figure A.0.1 HPPC test discharging sequence

A.2.2 HPPC Charging Test (Estimated time: 36 hrs)

1) Continue from 23.
2) Charge at C/3 rate until 5% of the measured Ah from the capacity test is added. The new SOC is at 5%.
3) Rest for 1 hour.
4) EIS test at this SOC level 5%.
5) Charge at the maximum current limit rate for 10 seconds and rest for 1 minute and discharge at 75% of the maximum current limit rate for 10 seconds and rest for 1 minute.
6) Charge at C/3 rate until 5% of the measured Ah from the capacity test is added. The new SOC is at 10%.
7) Rest for one hour.
8) EIS test at this SOC level 10%.

9) Charge at maximum current limit rate for 10 seconds and rest for 1 minute and discharge at 75% of the maximum current limit rate for 10 seconds and rest for 1 minute.
10) Charge at C/3 rate until 10% of the measured Ah from the capacity test is added. The new SOC is at 20%.
11) Rest for 1 hour.
12) Repeat steps 8 to 11 for SOC range from 20% to 90% in 10% SOC interval.....
13) EIS test at this SOC level 90%.
14) Charge at the maximum current limit rate for 10 seconds and rest for 1 minute and discharge at 75% of the maximum current limit rate for 10 seconds and rest for 1 minute.
15) Charge at C/3 rate until 5% of the measured Ah from the capacity test is added. The new SOC is at 95%.
16) Rest for 1 hour.
17) EIS test at this SOC level 95%.
18) Charge at the maximum current limit rate for 10 seconds and rest for 1 minute and discharge at 75% of the maximum current limit rate for 10 seconds and rest for 1 minute.
19) Charge at C/3 rate until the cell voltage reaches to V=Vmax and then charge at a constant voltage v=Vmax until current decreases to C/200 rate. The new SOC is at 100%.
20) Repeat the above steps for remaining test temperatures of -10˚C and 25 ˚C.

A.3 MEP Test Procedures

The MEP test is applied such that the battery is operated at is maximum limits during the duration of the pulse. The same pulse duration as with HPPC is used. The battery is charged/discharged at its maximum current until the voltage limit is reached, then a constant voltage condition is held there for the remaining duration of the pulse. Integrating power during

such a pulse results in the maximum energy the battery can provide during that pulse. Benefits of doing MEP test are that it avoids determination of appropriate current magnitudes, and can directly yield conservative power capability by using the power measured at the end of the pulse. An idealized response predominately in constant voltage mode in illustrated in Figure 4.9.

This test is roughly same with HPPC test, the only difference is the discharge and charge current pulses. Those pulses are replaced by maximum discharge and charge current instead of 1 C-rate and 0.75 C-rate. Note the maximum instant discharge/regenerative current amplitude are not given in battery datasheet. But referring to the maximum continues discharging current mentioned in the datasheet, the maximum instant discharge/regenerative current was chosen as 10 A. The same measurements and sampling rates for capacity tests are used for MEP.

A.3.1 MEP Discharging Test (Estimated time: 36 hrs)

23) Rest the cell at 25°C a night before the test.
24) Charge the cell at C/3 rate until voltage V=Vmax. (3 hrs)
25) Keep voltage at V=Vmax and reduce the charge current till current I=C/200. (depends on the chemistry, should be less than 30 mins)

    Note: This charging part can be alternatively finalized by the original charger from manufacturer, same as the charging phase in the future.
26) Rest for 2 hours.
27) Discharge at maximum discharge until 5% of the measured capacity in ampere-hour (Ah) from the capacity test is removed. The new SOC is at 95%.(3 hrs/20 = 9 mins)
28) Rest for 1 hour.
29) EIS test at this SOC level 95%. (20 mins)

30) Discharge at maximum discharging current limit for 10 seconds and rest for 1 minute and charge at the maximum charging current limit rate for 10 seconds and rest for 1 minute.(2.3 mins)
31) Discharge at C/3 rate until 5% of the measured Ah from the capacity test is removed. The new SOC is at 90%. (9 mins)
32) Rest for 1 hour. EIS test at this SOC level 90%.
33) Discharge at maximum discharging current limit for 10 seconds and rest for 1 minute and charge at the maximum charging current limit rate for 10 seconds and rest for 1 minute.(2.3 mins)
34) Discharge at C/3 rate until 10% of the measured Ah from the capacity test is removed. The new SOC is at 80%.
35) Rest for 1 hour.
36) Repeat the steps from 11 to 14 from 80% SOC to 10% SOC at 10% interval.....
37) EIS test at this SOC level 10%.
38) Discharge at maximum discharging current limit for 10 seconds and rest for 1 minute and charge at the maximum charging current limit rate for 10 seconds and rest for 1 minute.(2.3 mins)
39) Discharge at C/3 rate until 5% of the measured Ah from the capacity test is removed. The new SOC is at 5%.
40) Rest for 1 hour.
41) EIS test at this SOC level 5%.

42) Discharge at maximum discharging current limit for 10 seconds and rest for 1 minute and charge at the maximum charging current limit rate for 10 seconds and rest for 1 minute.(5-21: 19* 1.5 hrs = 29 hrs)
43) Discharge at C/3 rate until the cell voltage reaches to voltage V=Vmin and then discharge at a constant voltage v=Vmin until current decreases to C/200 rate. The new SOC is at about 0%. (9 mins)
44) Rest for 2 hours.

A.3.2 ME Charging Test (Estimated time: 36 hrs)

45) Continue from 23.
46) Charge at C/3 rate until 5% of the measured Ah from the capacity test is added. The new SOC is at 5%.
47) Rest for 1 hour.
48) EIS test at this SOC level 5%.
49) Charge at the maximum charging current limit rate for 10 seconds and rest for 1 minute and discharge at the maximum discharging current limit rate for 10 seconds and rest for 1 minute.
50) Charge at C/3 rate until 5% of the measured Ah from the capacity test is added. The new SOC is at 10%.
51) Rest for one hour.
52) EIS test at this SOC level 10%.
53) Charge at the maximum charging current limit rate for 10 seconds and rest for 1 minute and discharge at the maximum discharging current limit rate for 10 seconds and rest for 1 minute.

54) Charge at C/3 rate until 10% of the measured Ah from the capacity test is added. The new SOC is at 20%.
55) Rest for 1 hour.
56) Repeat steps 8 to 11 for SOC range from 20% to 90% in 10% SOC interval.....
57) EIS test at this SOC level 90%.
58) Charge at the maximum charging current limit rate for 10 seconds and rest for 1 minute and discharge at the maximum discharging current limit rate for 10 seconds and rest for 1 minute.
59) Charge at C/3 rate until 5% of the measured Ah from the capacity test is added. The new SOC is at 95%.
60) Rest for 1 hour.
61) EIS test at this SOC level 95%.
62) Charge at the maximum charging current limit rate for 10 seconds and rest for 1 minute and discharge at the maximum discharging current limit rate for 10 seconds and rest for 1 minute.
63) Charge at C/3 rate until the cell voltage reaches to voltage V=Vmax and then continue charging at a constant voltage V=Vmax until current decreases to 1/200 C-rate. The new SOC is at about 100%. (9 mins)
64) Rest for 2 hours.

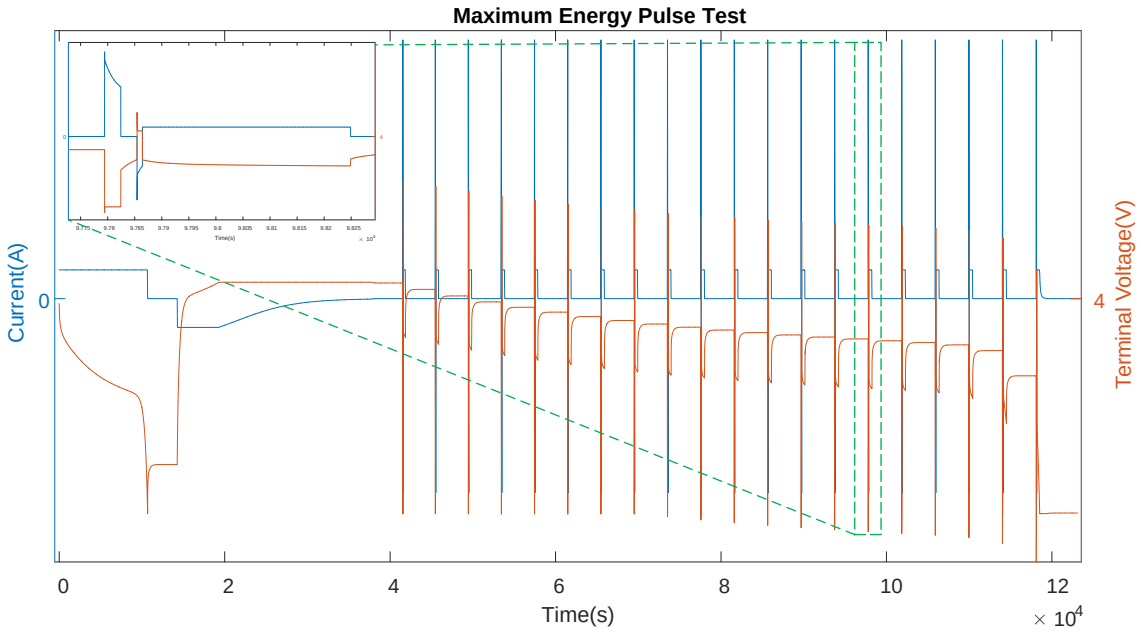

Figure A.0.2 MEP test discharging sequence

These max current pulses will lead to two possible results: (1) when the voltage reaches its limit value before the current does, the battery will remain in constant voltage mode, and the current will fade slowly. Because the current fades, the constant voltage mode will never be converted to the constant current mode. (2) When the current reaches its limit value before the battery voltage does, the battery will maintain a constant current state, and the voltage will continue to change slowly. The constant current mode will be converted to the constant voltage mode once the voltage reaches the limit value.

A.4 EIS Test Procedures

Data should be recorded at a sampling rate of at least 10 times the largest frequency of the AC signal. For example, the AC signal has a frequency of 1kHz, it should be recorded at a rate of at least 10kHz.

The test steps are given below:

1) Set temperature to the desired setting inside the temperature chamber.
2) Set the SOC level for the battery under test. Potentiostat will apply a DC voltage bias to the battery at its characteristic voltage (3.62 V). The AC voltage wave was applied on top of that.
3) The frequencies vary from 1mHz to 1kHz. The frequencies should be separated in
    a. 0.001Hz – 0.01Hz
    b. 0.01Hz-0.1Hz
    c. 0.1Hz-1Hz
    d. 1Hz-10Hz
    e. 10Hz-100Hz
    f. 100Hz-1000Hz

Each decade had 5 frequencies in between. The amplitude of AC voltage was set at less than 10mV. (1 period: 17 mins)

4. Repeat steps 1 to 3 for other desired SOC and temperature settings.

A.5 Components and Their Costs

In order to finish this thesis, the following components were purchased:

Table A.1: Components and costs

Component	**Cost**
Conventional bicycle for electrifying	CAD$ 600
BionX conversion kit	CAD$ 1999.99
Wahoo speed and cadence sensor	US$ 79
Cycle analyst V3 and analogger	CAD$ 367
Bicycle trainer/stand	CAD$ 119.99
Total	CAD$ 3087 + US$ 79